Formation of U-rich mineralizing fluids through basinal brine migration within basement-hosted shear zones: A large-scale study of the fluid chemistry around the unconformity-related Cigar Lake U deposit (Saskatchewan, Canada)

Pierre Martz, Julien Mercadier, Michel Cathelineau, Marie-Christine Boiron, David Quirt, Amber Doney, Olivier Gerbeaud, Etienne de Wally, Patrick Ledru

▶ **To cite this version:**

Pierre Martz, Julien Mercadier, Michel Cathelineau, Marie-Christine Boiron, David Quirt, et al.. Formation of U-rich mineralizing fluids through basinal brine migration within basement-hosted shear zones: A large-scale study of the fluid chemistry around the unconformity-related Cigar Lake U deposit (Saskatchewan, Canada). Chemical Geology, 2019, 508, pp.116-143. 10.1016/j.chemgeo.2018.05.042 . hal-02334115

HAL Id: hal-02334115
https://hal.science/hal-02334115

Submitted on 22 Oct 2021

HAL is a multi-disciplinary open access archive for the deposit and dissemination of scientific research documents, whether they are published or not. The documents may come from teaching and research institutions in France or abroad, or from public or private research centers.

L'archive ouverte pluridisciplinaire **HAL**, est destinée au dépôt et à la diffusion de documents scientifiques de niveau recherche, publiés ou non, émanant des établissements d'enseignement et de recherche français ou étrangers, des laboratoires publics ou privés.

Distributed under a Creative Commons Attribution - NonCommercial 4.0 International License

Version of Record: https://www.sciencedirect.com/science/article/pii/S0009254118302985
Manuscript_eee62ac3baf17a8a9dfee657691962a9

Formation of U-rich mineralizing fluids through basinal brine migration within basement-hosted shear zones: a large-scale study of the fluid chemistry around the unconformity-related Cigar Lake U deposit (Saskatchewan, Canada)

Pierre Martz [a], Julien Mercadier [a], Michel Cathelineau [a], Marie-Christine Boiron [a], David Quirt[b], Amber Doney [b], Olivier Gerbeaud[b], Etienne De Wally [a], Patrick Ledru [b].

[a] Université de Lorraine, CNRS, CREGU, GeoRessources Lab., Campus Aiguillettes, Faculté des Sciences et Technologies, rue Jacques Callot, Vandoeuvre-lès-Nancy, F-54506, France

[b] AREVA Resources Canada Inc. 817 45th Street West, S7K 3X5, Saskatoon, Saskatchewan, Canada

Abstract

The evolution of basinal brines through percolation into basement rocks is studied in the Paleo- to Mesoproterozoic Athabasca Basin and its underlying basement. This specific geological context includes the evolution of a NaCl-rich basinal brine to a U-mineralizing $CaCl_2$-rich brine that is of particular importance for the understanding of the formation of giant U deposits. The objective of this study is to determine the physico-chemical parameters (P-T-X) of the basinal brines and their changes both within the Athabasca Group sandstones and the underlying basement lithologies, on the scale of several km around the world class unconformity-related Cigar Lake U deposit.

Particularly, this study focuses on the basement-hosted fault systems that are considered to be the main fluid flow pathways. A comprehensive study including microthermometry, Raman spectroscopy, and LA-ICP-MS analyses was carried out on fluid inclusions, as was a semi-

© 2018 published by Elsevier. This manuscript is made available under the CC BY NC user license
https://creativecommons.org/licenses/by-nc/4.0/

quantitative estimation of the microfracture paleoporosity based on the surface density of fluid inclusion planes.

Initial NaCl-rich brines were trapped during early diagenesis (c.a. 1.7-1.65 Ga) in dickite-rich sandstones, under a three to seven kilometers thick sedimentary cover at around 90 to 150 °C under hydrostatic pressure, or at 120-210°C assuming lithostatic conditions. At the time of U deposits formation (ca. 1.46-1.29 Ga), these brines percolated through the entire basement, but preferentially within the damage zones of some graphite-rich faults, formed during the ca. 1.8 Ga Trans-Hudson Orogeny and active during the subsequent retrograde metamorphism and exhumation (ca. 1.8-1.72 Ga). The circulation of the basinal brines into these structures was enhanced and structurally-controlled by the microfracture network inherited from earlier brittle reactivation during basement uplift. The resulting high microfracture paleoporosity in the vicinity of some, but not all, of these structures favored intense interaction between the brines and basement rocks that induced the formation of illite-sudoite alteration haloes. In the basement, the percolating brines scavenged Mn, K, Ba, Sr, and especially U, and evolved from the original NaCl-dominant composition towards a higher salinity $CaCl_2$-rich composition. The resulting U-bearing brine mixed with the unmodified diagenetic NaCl-rich brine in, above, and all along the reactivated faults, either during thermal convection in isobaric settings and higher temperatures (110-200 °C) or through episodic tectonic reactivation in isothermal settings through episodic pressure fluctuation. In direct vicinity of the U deposits, the interactions between the brines and the basement rocks were the strongest, which is marked by the highest intensity of alteration of the host rocks.

Thus, the formation of ore-forming fluids resulted from the interaction between NaCl-rich basinal brines and highly-microfractured basement rocks. This study reinforces the hypothesis that interaction with basement rocks enhanced by strong fluid flow in cataclastic zones, can significantly modify the physico-chemical characteristics of basin-derived brines, leading to

the formation of mineralizing fluids and the genesis of giant ore deposits, such as the unconformity-related U deposits.

Keywords

basinal brines, unconformity-related uranium deposit, metals, microfracturing, uranium, Athabasca Basin.

Highlights

- Tectonic reactivation of some basement-hosted graphite-rich shear zones below the Athabasca Basin favored a significant increase of the porosity within these structures and the percolation of basinal brines into these structures;
- Interaction between NaCl-rich basinal brines and basement rocks induced modification of the Na/Ca ratio of the brines and metal uptake, resulting in the formation of $CaCl_2$- and U-rich ore-forming brines;
- NaCl and $CaCl_2$-rich brines mixed in and above reactivated shear zones due to thermal and/or deformation-driven convection.

1. Introduction

Unconformity-related uranium deposits are the world largest high-grade U deposits with average grades reaching up to 20 wt.% U. They represent about 240,000 t of reasonably-assured recoverable U resources at a cost of < USD 80 / kg U. These resources correspond to around 20% of the world's U resources and the bulk of it occurs in the Athabasca Basin region of northern Saskatchewan, Canada (OECD/NEA-IAEA, 2016). This study focuses on the Cigar Lake deposit which is the world's second-largest high-grade uranium deposit

75 containing 613,400 t of mineral reserves at an average grade of 15.9% U_3O_8 (Cameco, 2016).
76 These deposits are called “unconformity-related” because of their spatial relationship to the
77 unconformity between the Paleo- to Mesoproterozoic sedimentary cover and the underlying
78 crystalline basement.
79 The formation of these deposits is thought to be related to a major ore-forming event dated
80 between 1.6 and 1.3 Ga (Alexandre et al., 2007 and references therein). This event is linked
81 to the circulation of two brines, one NaCl-rich and the other $CaCl_2$-rich, that circulated before,
82 during, and after UO_2 deposition (Chu and Chi, 2016; Derome et al., 2005; Kotzer and Kyser,
83 1995; Pagel, 1975a; Pagel et al., 1980; Richard et al., 2016, 2010). Both brines have been
84 considered to have had a similar origin: sub-aerial evaporation of seawater, based on halogen
85 (Cl-Br-I) and noble gas (Ar-Kr-Xe) systematics, high salinities, stable chlorine isotopic
86 compositions, and also the B isotopic composition of tourmaline (sensu lato: “dravite”;
87 Derome et al., 2005; Leisen et al., 2012; Mercadier et al., 2012; Richard et al., 2014, 2011).
88 The $CaCl_2$-rich brines contain up to one order of magnitude more uranium and associated
89 metals (Cu, Pb, Zn, Mn) relative to the NaCl-rich brines (Richard et al., 2016, 2010). The
90 compositional differences between the two brines are considered to be a result of different
91 degrees of fluid-rock interaction, caused by variable availability of reactive rock along fluid
92 migration pathways (Richard et al., 2016). The greater Ca, Cl, and metal contents in the
93 $CaCl_2$-rich brine compared to the NaCl-rich brine are the result of processes that have been
94 already described in other contexts, such as European Pb-Zn-F-Ba deposits (Boiron et al.,
95 2010; Bons et al., 2014; Burisch et al., 2017b, 2016a; Fusswinkel et al., 2013; Gleeson et al.,
96 2003, 2001; Heijlen et al., 2003; Kendrick et al., 2005; Markl et al., 2016; Walter et al., 2017,
97 2016; Wilkinson et al., 2005), Australian Pb-Zn deposits (Feltrin et al., 2003), North African
98 Ag-Hg deposits (Essarraj et al., 2016, 2005), European and African Cu deposits (Koziy et al.,
99 2009; McGowan et al., 2006; Muchez et al., 2005) , as well as a few active hydrothermal

systems such as the Rhine graben (Cathelineau and Boiron, 2010) and the KTB drill hole fluids (Lodemann et al., 1997; Möller et al., 2005). All these examples share the following model: sedimentary brines of evaporitic origin (either primary or secondary) percolated within the basement and participated in specific water-rock interaction, resulting in cation exchange, salinity changes, and metal-leaching during fluid circulation. However, several uncertainties remain in this general model, especially for unconformity-related U deposits. Among these are: i) the mechanisms of conversion from NaCl-rich brine to $CaCl_2$-metal-rich brine, ii) the vertical and horizontal extent of fluid flow within the basement, and iii) the fluid flow mechanisms. Such knowledge deficiencies are present because nearly all of the pertinent data have so far only been acquired from (1) the Athabasca Basin sedimentary rocks, and (2) the immediate surroundings of the deposits, not from the basement rocks or away from the mineralized areas.

For this purpose, this study examines at a multi-kilometer scale (1) the main fluid flow pathways, and (2) the spatial distribution of the P-T-X features of the brines, trapped in both the sedimentary rocks (quartz overgrowths around detrital quartz and hydrothermal quartz veins) and in the basement (fluid inclusion planes [FIPs] crosscutting magmatic and metamorphic quartz). Oriented samples have been selected within a 25 km² area surrounding the Cigar Lake deposit and specifically along perpendicular profiles that cross-cut several different basement-hosted fault zones. Semi-quantitative estimations of the microfracture paleoporosity within selected lithologies and the local stress regime at the time of brine circulation were obtained by measuring the relative abundance and orientations of the FIPs in the basement. These estimations were used to track the physico-chemical evolution of the basinal brines during fluid-rock interaction and to understand the main controls of the brine migration at scales previously not investigated: in and around the deposit.

2. Geological setting

2.1. Regional geology

The basement below the Athabasca Basin (Saskatchewan, Canada) can be subdivided into two lithostructural subprovinces of the Western Churchill structural province: the Rae Subprovince to the west and the Hearne Subprovince to the east, separated by the Snowbird Tectonic Zone (STZ; Lewry et al., 1985; Fig. 1). The Hearne Subprovince can be further divided into three sub-domains: the Virgin River, Mudjatik, and Wollaston Domains. Most of the known unconformity-related U deposits are located in the Hearne Subprovince and, there, they are spatially concentrated at the transition between the Mudjatik and Wollaston Domains (Wollaston-Mudjatik Transition Zone: WMTZ). The two latter domains formed during the ca. 1.8 Ga continent-continent collision of the Trans-Hudson Orogeny (THO; Lewry et al., 1985; Lewry and Sibbald, 1977). The rocks in the WMTZ mainly correspond to polydeformed and metamorphosed metasediments (up to granulite facies) of the Wollaston Group overlying elongated Archean granitoid and orthogneissic domes. Widespread quartzo-feldspathic anatectic sweats, leucogranites, and granitic pegmatites formed between ca. 1.86 and 1.80 Ga (Annesley et al., 2005 and references therein). Major graphitic shear zones formed in graphitic metasedimentary lithologies throughout the THO and contributed to the overall basement structural framework (Annesley et al., 2005; Jeanneret et al., 2016; Martz et al., 2017). Most of the unconformity-related uranium deposits discovered to date are located within or above graphitic shear zones.

Deposition within the Athabasca Basin occurred following the exhumation of the Trans-Hudson orogenic belt at ca. 1700 Ma (Jeanneret et al., 2016) and at least before ca. 1640 Ma, which is the age of the Wolverine Point Formation, present near the top of the currently preserved Athabasca stratigraphy (Rainbird et al., 2007). The sedimentary rocks within the Athabasca Basin belong to the undeformed Athabasca Group (Ramaekers et al., 2007). It

consists mainly of thick sequences of Paleo- to Mesoproterozoic, polycyclic, fluvial to marine quartz sandstone deposited in a near-shore shelf environment (Ramaekers et al., 2007). The strata are divided into ten stratigraphic units: the earliest, quartz-rich conglomerate and sandstone with minor mudstone of the Fair Point Formation and subsequent Read, Smart, Manitou Falls, and Lazenby Lake Formations; sandstone and variably phosphatic siltstones/mudstones of the Wolverine Point Formations; sandstone and conglomeratic sandstones in the Locker Lake and Otherside Formations; mudstone, shale, and fine sandstone of the Douglas Formation, and finally stromatolitic carbonates with siliciclastic interbeds of the Carswell Formation (Ramaekers et al., 2007). The current maximum preserved thickness of the basin is about 1500 m but the maximum thickness has been interpreted to have reached a thickness of 3-5 km based on P-T estimations from fluid inclusions (Pagel, 1975a, 1975b). In the Cigar Lake deposit area, the only preserved stratigraphic unit is the Manitou Falls Formation containing quartz-rich sandstones and microconglomerates. The thickness of the Athabasca strata in the study area ranges from about 260 to 470 meters (Bruneton, 1993).

2.2.Local geology around the Cigar Lake deposit

The Cigar Lake deposit is a world-class unconformity-related uranium deposit located in the eastern part of the Athabasca Basin (Fig. 1). The deposit is in the form of an E-W elongated, ~1.9 km-long, 15-100 m-wide and ~10-20 m-high lens. Although the timing of U deposition remains open to debate, the main U stock, if not all of it, is believed to have precipitated between ca. 1.46 and 1.29 Ga (Fayek et al., 2002; Martz, 2017; Philippe et al., 1993). The deposit is almost entirely sandstone-hosted and occurs immediately above the unconformity between the Athabasca Group sedimentary cover and the underlying Paleoproterozoic metasediments of the Wollaston Group and Hudsonian plutonic rocks, and directly above a major E-W-oriented, S-dipping, graphitic-rich structure called the “Cigar Main conductor”

175 (Fouques et al., 1986; Bruneton, 1993). This structure is characterized by several stacked
176 graphite-bearing ductile-brittle shear zones developed within pelitic gneisses and lesser
177 calcsilicate rocks. It forms a 10 km-long electromagnetic (EM) conductor that was the
178 exploration target that resulted in the discovery of the deposit during the 1980-1981 winter
179 field season.
180 There is a main regional ductile fabric (foliation) striking SW-NE, the formation of which has
181 been attributed to the early THO deformation events (D1/D2, 1860 - 1830 Ma; Annesley et
182 al., 2005). Paleoproterozoic metasediments constitute the prominent basement lithology
183 encountered in drill holes all over the Cigar Lake area and are thought to be bounded to the
184 north by an Archean orthogneissic dome (Fig. 2). The contact between metasediments and
185 orthogneisses, called the "Cigar North-East Trend", is characterized by a contrast of the
186 magnetic properties (airborne data), and the occurrence of sheared rocks, mylonitized granite,
187 and graphite-rich fault rocks.
188
189 *Graphitic shear zones*
190 Graphite-bearing basement shear zones constitute the geological source of the EM conductors
191 identified in the Cigar lake area. Two main conductors have been identified, the Cigar Main
192 (E-W oriented) and the Cigar North-East Trend, as well as a third subordinate conductor
193 ("Power Line"), located 8 km to the south.
194 These shear zones contain a former ductile sheared fabric, characterized by the development
195 of porphyroblastic textures (cordierite and feldspar porphyroblasts, typically wrapped by
196 chlorite-graphite layers), locally showing S-C fabric, and the existence of dynamic quartz
197 recrystallization textures (grain boundary migration). A gradual steepening of the
198 metamorphic foliation is commonly observed, from 60 - 70° to the south-south-west (regional
199 trend) to 80° (locally subvertical) within the graphitic shear zones, in association with

increase in the intensity of shearing and the graphite content (locally up to ~50%). The shear zones were initiated in C-rich Paleoproterozoic (meta)sedimentary layers at near-peak THO metamorphic conditions (6 - 9 kbar and 750 - 825 °C; Annesley et al., 2005; Martz et al., 2017; McKechnie et al., 2012). They were reactivated under brittle conditions during the late stages of post-Hudsonian basement exhumation (1.775 – 1.720 Ga) leading to focused C-O-N-H fluid circulation and subsequent formation of hydrothermal chlorite and graphite along brittle fault planes (Martz et al., 2017). An abundant vein network additionally developed within the shear zones, with formation of white dolomite and milky quartz veins (some also filled by later pyrite) either parallel to the foliation or sub-horizontal. These late structures are observed in both the E-W and NE-SW trends.

The overall fracture density increases toward the central part of the shear zones and progressively overprints the former ductile fabric. The central zones with the highest degree of brittle deformation are referred to as fault damage zones. The fault cores are characterized by intervals, several meters wide, of cohesive fault rocks (proto- to ultracataclasites; Sibson, 1977) that are bounded by non-cohesive fault gouges containing sooty graphite, chlorite, dolomite, and sometimes euhedral pyrite. Finally, later veinlets of clear quartz, pink dolomite, and chlorite are observed in and near the fault cores, crosscutting the earlier milky quartz veins. For the three studied distinct ductile-brittle shear zones, the relatively large spacing between the drill holes (typically 50m) does not allow to say with certainty if the fault continues into the basin strata or not. Particularly for the E-W trend, it is uncertain if there is a small offset at the unconformity or not.

The alteration halo

224 At Cigar Lake, a well-developed host-rock alteration halo in the sandstone extends more than
225 300 m above the main U mineralization. It also extends more than 50 m into the basement
226 beneath the mineralization, however the extent of the alteration in the basement remains
227 poorly constrained due to a lack of drill cores that reach these depths (Pacquet and Weber,
228 1993). This alteration halo is composed of hydrothermal assemblages of illite and sudoite
229 (Mg-chlorite). Unlike most other unconformity-related deposits in the Athabasca, occurrences
230 of alkali-deficient dravitic tourmaline ("dravite") are rarely described. The illite-
231 sudoite±dravite clay mineral assemblage is typical of the host-rock alteration around the
232 unconformity-related deposits, both in the Athabasca region (Hoeve and Quirt, 1984;
233 Alexandre et al., 2005; Hoeve and Sibbald, 1978; Kister et al., 2005; Laverret et al., 2006; Ng
234 et al., 2013) and in the McArthur Basin in Australia (Beaufort et al., 2005; Fisher et al., 2013;
235 Nutt, 1989; Polito et al., 2004; Skirrow et al., 2016). Within the halo, all the primary minerals
236 of the basement rocks are replaced by the illite-sudoite(± dravite) assemblage while, in the
237 Athabasca strata, illite replaces the early- and peak-diagenetic dickite (± earlier illite) clay
238 mineral assemblage for over 400 m above the unconformity (Hoeve and Quirt, 1984; Quirt,
239 2001; Pacquet and Weber, 1993; Percival et al., 1993). The alteration halo is also marked by
240 intense quartz dissolution both in the sedimentary strata and the basement. Finally, a
241 hematite-siderite cap can be observed just above the highly clay-altered material of the main
242 mineralized zone (see also Hoeve and Quirt, 1984).
243

244 ## 3. Sampling

245 The sample set includes specimens from the deposit, distal areas, the basement and the basin,
246 which facilitates the reconstruction of physical-chemical conditions on a much larger scale
247 (~25 km^2) than the spatial extent of the deposit. This greater spatial area of study both in the
248 basin and the basement allows investigation of the overall conditions of basinal brine

circulations and the physico-chemical changes in the brines that were induced by these migrations within the environments surrounding the deposit. The sampling was focused on the three main ductile-brittle shear zones in the area: Cigar Main, Cigar North-East Trend, and Power Line. 46 samples of basement rocks (42 of granitic pegmatite and 5 of pelitic gneiss) and 17 sandstone samples were taken from 26 drill cores. Drill hole locations are indicated in Fig. 2. Sample names include the name of the drill hole and the depth of the sample (in meters).

i) In the deposit area, the sampling was from two horizontal geotechnical drill holes located in the basement below the deposit (U382 and U427) and from three vertical drill holes intersecting the deposit (SF-731-05 and SF-737-05 into its east part and WC372 into its west part).

ii) Along the E-W Cigar Main structural corridor, the sampling covers 15 drill holes, located up to 7 km to the east of the deposit and mainly focused in two cross-sections through the shear zones (A-B and C-D on Fig. 2).

iii) Along the Cigar North-East Trend, the sampling covers three drill holes (WC473, WC448, and WC467).

iv) Along the NE-SW Power Line structure, two drill holes (WC464 and 466A) were sampled.

v) One additional barren drill hole (WC254), located about 500 m south of the deposit and outside of the Cigar Main shear zone, was sampled.

Sampling of the basement lithologies included a selection of representative oriented-core samples of Hudsonian pegmatites and metapelitic gneisses showing various and distinct alteration intensities. Pegmatites (anatectic sweats, leucogranites, and granitic pegmatites) were specifically selected because these rocks contain large magmatic quartz crystals most suitable for FIP mapping and fluid inclusion analyses and they are a lithology representative

of the host rocks. The pegmatites were formed during peak metamorphic conditions of the THO and are most suitable to record all different fluid events post-dating the peak metamorphism, both pre- and post-basin deposition (eg. Mercadier et al., 2010). Five representative samples of metapelitic gneiss were sampled to compare the geometry of the fracture network and the fracture paleoporosity at the time of brine migration with those in the pegmatites. The maximum investigated depth is about 200 m below the unconformity. Collected sandstone samples represent variable intensities of hydrothermal alteration. Where available, druzy quartz, present in small fractures that crosscut the sandstone, was also studied.

4. Methods

Microthermometry

Microthermometry was carried out on fluid inclusions (FI) trapped in quartz overgrowths, quartz cement, and druzy quartz in sandstone samples, as well as on selected FIPs in magmatic quartz from basement samples. It was performed using a Linkam® MDS600 heating-cooling stage, adapted to an Olympus® microscope at the GeoRessources laboratory (Nancy, France). The stage was calibrated with in-house and certified standards by measuring the temperature of the final melting of pure water (0.0°C) in a silica glass capillary, the triple point of CO_2 ± Ar in a synthetic FI (-56.9°C), and the homogenization temperature (L+V → L) of a natural FI at 165 °C. The following microthermometric parameters were measured: eutectic temperature (Te), melting temperatures of ice and hydrohalite (Tm_{ice} and Tm_{hyd}), halite dissolution (Ts_{NaCl}), and homogenization temperature (L+V→L or L+V+S→L+S; Th). The temperatures of phase changes have a precision of about ± 5 °C for Te, ±0.1 °C for Tm_{ice} and Tm_{hyd}, and ±1 °C for Ts_{NaCl} and Th. A significant number (about 30%) of the analyzed FI did not freeze, even at temperatures as low as -180 °C, as previously observed for similar

299 inclusions in the Athabasca (eg. Chu and Chi, 2016; Richard et al., 2016). Inclusions for
300 which Tm_{ice} could not be unambiguously determined were excluded from the dataset.
301
302 ## *Calculation of FI compositions*
303 The actual methodologies used for calculation of FI bulk compositions depend on the
304 considered system. The methodologies are presented with the FI nomenclature in Table 1.
305 The nomenclature is adapted from Derome et al. (2005) and is based on both the Tm_{ice} ranges
306 (Tm_{ice} < -30°C: Lw' and Lwh'; -30°C < Tm_{ice} < -15°C: Lw1, Lw2 and Lwh; -15°C < Tmice:
307 Lw") and the last observed phase to melt upon heating (ice: Lw1, Lw' and Lw"; hydrohalite:
308 Lw2 and Lw'; halite: Lwh and Lwh').
309 For Lw1 inclusions and Lw′ inclusions, within which the last phase to melt is ice, FI bulk
310 compositions were calculated respectively in the H_2O–NaCl and H_2O–$CaCl_2$ system using the
311 AqSo2e program (Package FLUIDS 1, Bakker, 2003, and references therein). The
312 composition of all the other inclusions were calculated in the H_2O–NaCl–$CaCl_2$ system
313 according to Steele-MacInnis et al. (2011).
314
315 *Raman spectrometry*
316 The relative proportion of the gas species of the volatile phase of the fluid inclusions
317 previously analysed by microthermometry was measured using a Horiba Jobin-Yvon
318 LabRAM spectrometer equipped with a 1800 gr mm^{-1} grating and an Edge filter. Each
319 analysis was repeated three times. The analytical uncertainty is below 5%. The confocal hole
320 aperture is 500 µm and the slit aperture is 100µm. The excitation beam is provided by a
321 Stabilite 2017 Ar^+ laser at 514.532 nm (Spectra Physics, Newport Corporation) and a power
322 of 200 mW, focused on the fluid inclusions using x50 and x100 objectives on an Olympus
323 BX40 microscope. The signal-to-noise ratio was optimized ideally to lower than 1% by

adjusting the acquisition time and accumulation number. All Raman spectrometry analyses were performed at room temperature at the GeoRessources laboratory (Nancy, France).

LA-ICP-MS on fluid inclusions

Selected major, minor, and trace elements were analyzed in fluid inclusions using the LA-ICP-MS equipment at GeoRessources laboratory (Nancy, France) (Lach et al., 2013; Leisen et al., 2012). It comprises a GeoLas excimer laser (ArF, 193 nm, Microlas, Göttingen, Germany; Günther et al., 1997) and an Agilent 7500c quadrupole ICP-MS. The laser beam is focused onto the sample, within a low-volume custom-made lozenge-shaped ablation cell designed for fluid inclusion analyses, using a Schwarzschild reflective objective (magnification × 25; numerical aperture 0.4) mounted onto an optical microscope (Olympus BX41) equipped with a X–Y motorized stage and CCD camera. The certified reference material NIST610 (Jochum et al., 2011) was used as the external standard. NIST612 was also used to monitor the analytical conditions (in particular, precision and accuracy). Analysis parameters include a fluence of 14 J/cm² and laser shot frequency of 5 Hz, He = 0.5 $L.min^{-1}$ as a carrier gas mixed with Ar = 0.7 $L.min^{-1}$ via a cyclone mixer prior to entering the ICP torch. Spot sizes varied from 24 µm up to 44 µm, depending on the inclusion size. The elemental isotopes analyzed were: ^{7}Li, ^{23}Na, ^{11}B, ^{24}Mg, ^{39}K, ^{44}Ca, ^{55}Mn, ^{57}Fe, ^{63}Cu, ^{66}Zn, ^{75}As, ^{88}Sr, ^{122}Sb, ^{137}Ba, ^{182}W, ^{208}Pb, and ^{238}U, using an integration time of 0.01 s per mass channel for a total cycle time of 0.22 s.

System calibration and signal integration were performed using the Matlab®-based SILLS program (Guillong et al., 2008). Absolute element concentrations were calculated from the analyzed elemental ratios relative to the absolute concentration of Na (Longerich et al., 1990). This Na concentration was obtained from microthermometry using the charge-balance technique (Allan et al., 2005) that corrects the modelled amount of Na for contributions from

other chloride salts using the analyzed elemental ratios to Na. No FIs interpreted through microthermometry as pure H_2O-$CaCl_2$ could be analyzed through La-ICP-MS. Limits of detection (LODs) were calculated using the 3σ criterion (Longerich et al., 1996). The analytical precision of most elements is within 20-30% RSD (Allan et al., 2005).

FIP mapping and paleoporosity estimation

The intensity and geometry of fluid circulation in the basement were estimated through a statistical study of FIP densities and orientations along sampling profiles cross-cutting the graphitic shear zones. This work was carried out on polished wafers of oriented samples from different drill holes following a methodology similar to Martz et al. (2017), Mercadier et al. (2010) and Scheffer et al. (2017). For all oriented core samples, wafers were prepared in the horizontal plane from a selected region of the core. Mapping of FIPs was then carried out in each wafer using the AnIma software (Lespinasse et al., 2005). FIP orientations are presented in rose diagrams. An example of FIP mapping is given in Fig. 3, with pictures of the three mapped FIP types. The distinct types are based on the FIs that they contain; i) carbonic fluid inclusions, ii) aqueous fluid inclusions, and iii) a mixture of both aqueous and carbonic inclusions in the same FIP (mixed FIPs; see Section 5 for detailed description and explanation). Based on the mapping of the distinct FIP types crosscutting the primary quartz grains, the fracture paleoporosity of the quartz was semi-quantified from the reconstructed microfracture network for each sample following the methodology developed by Sausse et al. (2001) and Lespinasse et al. (2005). Calculations are given in Appendix A. This method was first developed for total paleoporosity and paleopermeability calculations based on the total micro-fracture network. In this study, the method is applied only to FIPs in quartz and therefore it only allows calculation of the quartz fracture paleoporosity that is only a semi-quantitative proxy for the fluid/rock ratio at the time of the distinct fluid migrations. Since this

study is restricted to FIP microstructures in quartz, the estimated porosity will be overestimated as it does not take into account the size and irregular boundaries of the quartz grains. Moreover, the estimated connected porosity should also be considered as being a maximum instantaneous porosity, taking into account that microfracture sealing can be a rapid process (Lander and Laubach, 2015).

ShortWave InfraRed (SWIR) spectroscopy

Semi-quantitative determination of the relative proportions of a set of clay minerals has been carried out by AREVA Resources Canada (ARC) using the MINSPEC software developed by Earle (1997, 1996) on ShortWave InfraRed (SWIR) reflectance spectral data acquired using a field portable spectrometer (e.g. PIMA II, TerraSpec). The MINSPEC algorithm is based on the detection of characteristic absorption peaks (i.e. reflectance minima), as well as the shapes, shoulders, and slopes/inflections of the peaks and the intervening spectrum. The spectral measurements were performed on 10 to 20cm long drill core pieces every 3 m in all the selected drill holes, as well as on the individual samples from this study. Clay mineral types were confirmed through optical microscopy and SEM examinations at the GeoRessources laboratory (Nancy, France). The MINSPEC algorithm, designed specifically for Athabasca Group and Kombolgie Formation quartz-rich sandstones, semi-quantifies the relative proportions of six clay and clay-size minerals, including illite, three kaolin polymorphs (kaolinite, dickite, halloysite), sudoitic chlorite, and alkali-deficient dravite from each reflectance spectrum acquired. For this study, the three different kaolin polymorphs were not further distinguished - they all are simply given as kaolinite. In the same way, the proportion of illite may also include several illite polytypes, and may include muscovite in basement samples. The reported relative proportion of chlorite is based on sudoite (Al-Mg di,trioctahedral chlorite), however, it may also include clinochlore (trioctahedral Fe-Mg

399 chlorite) in basement samples. Clinochlore does not occur in the Athabasca strata (Hoeve and
400 Quirt, 1984).
401
402 # 5. Results
403 ## 5.1.Petrography
404 Fig. 4 summarizes the main petrographic features of the studied samples on a schematic
405 cross-section through the deposit. The same hydrothermal alteration, occurring in and around
406 the deposit, can be observed all along the Cigar Main Trend, but with significantly less
407 intensity when moving out of the near-deposit area.
408 *Basement rocks*
409 The granitic pegmatites and anatectic rocks have an initial magmatic mineral assemblage of
410 quartz, feldspar (K-feldspar ± plagioclase), biotite, muscovite, and accessory minerals such as
411 sulfide, zircon, monazite, and apatite. The pelitic gneisses show a metamorphic mineralogy of
412 quartz, feldspar (K-feldspar ± plagioclase), graphite, biotite, garnet, cordierite, sillimanite,
413 tourmaline, ilmenite, pyrite and chalcopyrite plus accessory minerals including apatite,
414 monazite, and zircon. In the basement rocks, three main types of superimposed alteration are
415 observed: i) The retrograde alteration of late-Hudsonian age is present in all studied samples.
416 It is characterized by a partial or total chloritization (Fe-Mg-rich chlorite) of biotite with an
417 associated crystallization of iron-titanium oxides and quartz, and formation of muscovites
418 (star-like appearance; with possible phengitic substitution <10%). Additionally, late chlorite,
419 graphite, pyrite, chalcopyrite, dolomite, and milky quartz are observed in fractures. ii) The
420 regolithic alteration ("paleoweathering"; Halter, 1988; Macdonald, 1980) occurs in the
421 uppermost meters of the basement, immediately below the unconformity, and is related to the
422 basement exhumation after the Trans-Hudson Orogeny. All the studied samples were taken
423 from below the paleoregolith extent and therefore do not show features of this alteration. iii)

Finally, the post-Athabasca hydrothermal alteration stage occurs in variable degrees in almost all the studied samples, even in the deepest and most distal samples from the deposit. This alteration is mainly expressed by an illite-sudoite ± dravite assemblage occurring either as secondary minerals or alteration assemblages in fractures or replacing the primary minerals. The relative proportion of sudoite to illite tends to be greater in the more altered samples, especially those located right under the deposit. Those samples usually show partial to total quartz dissolution features. Sudoite occurs as irregular flakes which are stacked in layers when present in high proportions (Percival and Kodama, 1989).

Athabasca sandstones

The sandstone samples all contain more than 90% sub-rounded to rounded detrital quartz grains, with no evidence of detrital K-feldspar or plagioclase being observed. Accessory minerals include sparse tourmaline and zircon, with iron-titanium oxides occurring locally in the clay matrix. Most of the sandstones and conglomerates from Cigar North-East Trend drill hole WC473 and Power Line drill hole WC464 show features of unaltered regional samples with well compacted and quartz-cemented sandstones containing frequent iron oxides in a clay matrix, entirely consisting of pseudomorphic dickite after kaolinite, filling the interstitial space (Fig. 5A). The detrital quartz grains (Q_0) show quartz overgrowths (Q_1) clearly distinguished by a line of FIs and iron oxides (called dustline, Fig. 5B). In the regional samples, quartz dissolution features are minimal to absent. In contrast, samples occurring above the Cigar Main E-W shear zone typically have a low iron oxides content ("bleached" rock; c.f. Hoeve and Quirt, 1984) and display strong dissolution features affecting both the detrital grains (Q_0) and quartz overgrowths (Q_1; Fig. 5C and D). Diagenetic dickite (itself after earlier kaolinite) is replaced by illite, illite crystals being sometimes embedded in Q_1 (Fig. 5E) and thus indicating that growth of Q_1 may have continue during and after dickite

449 replacement by illite. Small crystals of aluminum-phosphate-sulphate (APS) minerals are
450 locally disseminated in the illitic clay mineral matrix. The presence of sudoite is typically
451 restricted to the basal 5-20 meters of sandstone, above the basement graphitic structures,
452 either intermixed with illite or mechanically interlayered at a micro/nanoscale. Here, quartz
453 dissolution features are strongly developed (Fig. 5F). These features (sudoite occurrence plus
454 strong quartz dissolution) occur in greater abundance directly in and below the deposit. The
455 irregular presence of dustlines under Q_1 indicates that at least one quartz dissolution event
456 interrupted the diagenetic silicification pre- or syn-illite and sudoite crystallization.
457 Structurally-controlled pervasive silicification (Q_2) consists of quartz cement entirely filling
458 interstitial pores between the quartz overgrowths (Q_1). Q_2 is however very rarely observed at
459 Cigar Lake (in only one sample WC311-342.6; Fig. 5G), although it is common in the
460 McArthur River area (Derome et al., 2005). Euhedral quartz crystals (Q_3; <150 µm in size)
461 that crystallized in small open fractures cutting the sandstone, detrital grains, and quartz
462 overgrowths, were observed in nine samples out of the nineteen selected. Thick illite ±
463 sudoite rich dustlines are sometimes observed at the base of Q_3 indicating crystallization of Q_3
464 was post-illite+sudoite alteration (Fig. 5H).
465

466 ## 5.2.Fluid Inclusion petrography

467 *FIs in the basement rocks*

468 In magmatic and metamorphic quartz in basement rocks, FIs occur as secondary fluid
469 inclusion planes (FIPs) cross-cutting the quartz. They have been grouped into six major types:
470 i) dark, negative crystal-shaped, two- or three-phase carbonic (CO_2-CH_4-N_2±H_2O) fluid
471 inclusions (Fig. 3B), ii) two-phase aqueous-carbonic (H_2O-CO_2-CH_4-N_2) fluid inclusions, iii)
472 dark vapor monophase CH_4-N_2-rich fluid inclusions, iv) solid-bearing aqueous fluid
473 inclusions, v) low-salinity, two-phase, liquid-dominated, aqueous fluid inclusions, and finally

vi) high-salinity aqueous fluid inclusions. Types i) to iv) are only observed in the basement rocks and discussed in Martz et al. (2017), and are interpreted to have formed during pre-Athabasca retrograde metamorphic events. This study focuses only on the P-T-X properties of the basinal brines (Type vi) in the Paleoproterozoic Athabasca Basin, therefore the other types will not be discussed in this paper.

The brine fluid inclusions are aqueous liquid inclusions with a vapor phase of about 5-10 vol. % and can be either two-phase (liquid and vapor H_2O) (Fig. 6E), three-phase (with a halite cube) (Fig. 6F), or multi-phase (with halite and clay minerals). Carbonic fluid inclusions and high-salinity aqueous fluid inclusions are by far the most dominant types and can be easily distinguished from each other, as they present very distinct optical features.

FIs in the Athabasca sandstones

Fluid inclusions in quartz overgrowths (Q_1), cements (Q_2), and euhedral quartz (Q_3) from sandstones are small (<15 µm; often 3-10 µm in size) and fairly rare. They are aqueous liquid inclusions with a vapor phase of about 5-10 vol. % and sometimes contain a halite cube and/or a clay mineral (either dickite, illite, or sudoite) and iron oxides (Fig. 6A). FIs in Q_1 occur either along the dustlines, as pseudosecondary planes, isolated, or in small clusters (Fig. 6B). FIs in Q_2 and Q_3 occur isolated or in clusters (Fig. 5H and 6B and C). In dickite-rich samples, FIs are dominated by two-phase inclusions Lw1 and Lw2. In illite and/or sudoite-rich samples, FIs can be two-phase (liquid and vapor H_2O: Lw1, Lw2, Lw'), three-phase (with a halite cube, Lwh, Lwh'), or multi-phase (with halite and clay mineral) inclusions. Halite and/or clay minerals can occur either as heterogeneously-trapped minerals or as daughter minerals (same solid-vapor-fluid relative proportion in the whole FIA).

5.3.Fluid microthermometry

499 Microthermometric data for the post-Athabasca FIs are provided as supplementary data in
500 ESM-1.
501 *Inclusions with highly saline Na-Ca brines*
502 In the basement, microthermometric parameter ranges are: Te ranging from -75 to -54 °C,
503 Tm_{ice} from -50.8 °C to -16.8 °C, Tm_{hyd} from -25.3 to -0.5 °C, Th from 78 to 204 °C, TsNaCl
504 from 89 to 305 °C. In the sandstones: Te ranges from -74 to -57 °C, Tm_{ice} from -42.5 to -15.2
505 °C, Tm_{hyd} from -15.2 to -0.2 °C, Th from 84 to 226 °C, and finally Ts_{NaCl} from 112 to 305 °C
506 (ESM-1, Fig. 7A and B).
507 In the sandstones, there are significant variations in the temperature of phase transitions in the
508 FIs which correlate with the relative proportions of the clay mineral phases filling the
509 interstitial pore spaces. FIs in Q_1 for samples dominated by diagenetic dickite are mainly Lw1
510 inclusions. They show relatively high Tm_{ice} ranging from -25.1 to -20.5 °C (Fig. 7A and B),
511 specific to the NaCl-rich end-member, and low Th ranging from 84 to 121°C. The Th-Tm_{ice}
512 pairs for these FIs display a narrow range compared to the other studied FIs. Samples showing
513 partial to total dickite to illite replacement have FIs in Q_1, Q_2, and Q_3 displaying Tm_{ice} ranging
514 from -40.3 to -24.3 °C, Th ranging from 88 to 182 °C, and Ts_{NaCl} from 148 to 305 °C with no
515 clear differences between the distinct quartz types. Finally, samples containing sudoite have
516 FIs in Q_1 and Q_3 with Tm_{ice} ranging from -42.5 to -23.2 °C, Th ranging from 85 to 226 °C,
517 and Ts_{NaCl} from 112 to 246°C (Fig. 7A and B). A large Tm_{ice} variability can be observed in a
518 single FIA, either in a single Q_3 crystal (Fig. 6C) or in FIPs from the basement. In these FIA,
519 the Th remains constant.
520 $Th_{(L+V\rightarrow L)}$ - Ts_{NaCl} pairs of Lwh and Lwh' inclusions from both sandstone and basement
521 samples are presented in Fig 7B. Most of the Lwh FIs plot near the 1:1 slope in the $Th_{(L+V\rightarrow L)}$
522 - Ts_{NaCl} diagram (Fig 7B) indicating similar pressure trapping conditions with a fluid density
523 close to the isochoric path intersecting in a P-T diagram the point at which the halite liquidus

for its composition intersects the three-phase (liquid + vapor + halite) curve (Type B homogenization in Becker et al., 2008). In contrast, most of the Lwh' inclusions show halite dissolution after vapor disappearance upon heating (Type C homogenization in Becker et al., 2008) and a wide range of TsNaCl values, from about 130 up to 300 °C, together with a limited $Th_{(L+V\rightarrow L)}$ range mostly between 100 and 150 °C (Fig 7B). The observed scattering of the TsNaCl values expresses mainly heterogeneous trapping of halite (varying TsNaCl and constant Th in a single FIA, Fig 7B), indicating that the fluid trapped in Lw' and Lwh' became saturated with respect to halite. Nonetheless, some FIAs show Lwh' inclusions with similar TsNaCl - Th(L+V→L) pairs and TsNaCl > Th(L+V→L) (Fig 7B) indicating slightly higher minimal pressure trapping conditions compared to the Lwh inclusions (Fig. 7B).

Low salinity inclusions

Lw" inclusions in FIPs from the basement rocks show Tm_{ice} ranging from -4.2 to -1.2 °C and Th ranging from 93 to 196 °C. Lw" inclusions in the sandstone samples occur in Q_1 and Q_3. They are rare and were mainly observed in the same location (drill holes WC426 and WC441). They never occur in the same FIA with the brines (Lw1, Lw2, Lw', Lwh, or Lwh' inclusions), indicating the presence of local conditions disconnected from the main basinal brine circulation events. Their Tm_{ice} range from -10.2 to -0.1 °C and their Th from 84 to 132 °C.

5.4. Spatial distribution of microthermometric data and gas contents of FIs

There is a spatial distribution of FI types around and at distance from the deposit as follows:

FIs in the basement rocks

548 Away from the Cigar Main shear zone, i.e. in the Power Line (South conductor) and Cigar
549 North-East Trend shear zones, and outside the shear zones, only Lw1, Lw2, and Lwh FIs with
550 Tm_{ice} > - 26.3°C and Na/(Na+Ca) > 0.7 can been observed (Fig. 8). For nearly all of the
551 samples from these areas, the mean and median salinity for the FIs are about 25 wt.% eq.
552 NaCl + $CaCl_2$. The exception is sample WC254-460.5. In this sample 5 analyzed Lwh
553 inclusions occur with Lw1 inclusions in the same FIP. The FIs for these samples present the
554 lowest Th values, with a mean of 98 °C for the Cigar North-East Trend, 100 °C for Power
555 Line, and 122.5 °C away from conductors (Fig. 8).
556 Along the Cigar Main shear zone, both NaCl- and $CaCl_2$-rich inclusions have been observed.
557 Here, samples show overall a greater proportion of Lwh and Lwh' inclusions (up to 100%)
558 and therefore FIs with higher salinities (up to ca. 40 wt.% eq. NaCl + $CaCl_2$). Mean and
559 median Tm_{ice} values for FIs of samples occurring in this zone are usually below -26°C and
560 Na/(Na+Ca) ratio are variable, but overall low, with mean values ranging from 0.57 to 0.82
561 indicating significant calcium content in the trapped FIs. These FIs show an overall higher
562 range of Th values (80 to 200 °C) compared to the other structures.
563 Below the deposit, NaCl-rich Lwh and CaCl2-rich Lwh' and Lw' FIs predominate, and they
564 show high salinities (up to ca. 40 wt.% eq. NaCl + $CaCl_2$), the lowest Tm_{ice} (down to -50.8
565 °C), and a significant proportion of FIs with very low Na/(Na+Ca) ratio (<0.65 and down to
566 0) . There is no clear difference in the Th values compared to the barren portions of Cigar
567 Main.
568 *FIs in the sandstone*
569 The composition of the FIs trapped in the quartz overgrowths and in druzy quartz in the
570 sandstone varies according to the clay assemblage, which is directly dependent on the location
571 of the samples relative to the Cigar Main shear zone and to the Cigar Lake deposit (Fig. 9).

572 Above the barren NE-SW trending shear zones (i.e. Cigar North-East Trend and Power Line),
573 the sandstones are dominated by dickite. In these rocks, the FIs are Lw1, Lw2, and Lwh
574 inclusions. They display overall high Tm_{ice} (mean at -22.5 °C), almost pure NaCl
575 compositions with Na/(Na+Ca) = 1, high salinities (around 25 wt.% eq. NaCl + $CaCl_2$), and
576 low Th (around 90-100 °C, Fig. 9). However, in the basal 15 m above the unconformity both
577 above the Cigar North-East Trend and Power Line, illite and sudoite occur nonetheless,
578 replacing dickite (cf. sample WC473-385.4). In these areas, the FIs show lower Tm_{ice} and
579 Na/(Na+Ca) ratio (mean at 0.73), higher Th and higher salinities (Fig. 9).
580 Above the Cigar Main shear zone, the illite alteration extends up to the current surface,
581 whereas sudoite is present only in the basal 20 m above the basement shear zone. In contrast
582 to the FIs described above, here, the FIs trapped in Q_1, Q_2,, and Q_3 show a significant content
583 of $CaCl_2$ as expressed through overall low Tm_{ice} and Na/(Na+Ca) ratio, and significantly
584 higher Th (around 100-150 °C).
585 Toward the deposit, the proportion of $CaCl_2$-rich FIs per sample increases and those same
586 $CaCl_2$-rich inclusions show overall lower Tm_{ice} and Na/(Na+Ca) ratio, so higher $CaCl_2$
587 contents, toward the deposit, without visible Th gradient as a function of the distance to the
588 deposit.
589 Low-salinity fluid inclusions Lw" are locally present to the east of the studied zone in both Q_1
590 and Q_2, above both the Cigar Main and Cigar North-East Trend, and occur in higher
591 proportions compared to the basement samples. They display high Tm_{ice} (up to 0 °C) and
592 slightly higher Th (up to 180 °C) compared to other FIs.
593

594 ## 5.5.Gas contents in FIs and spatial distribution

595 Due to the limited size of the vapor phases, the vapor bubbles often show Brownian motion.
596 Therefore, the gas contents of only a few FIs could be successfully analyzed by Raman

spectroscopy. Furthermore, the uncertainty is high due to the small size of the inclusions and the overall low gas content. No volatile components have been detected in the liquid phase. The presence of trace amounts of CH_4, CO_2, N_2, H_2, and O_2 have occasionally been detected in the vapor phase, but only in high salinity FIs trapped in basement rocks. None of these constituents have been detected in the vapor phase of the sandstone hosted FIs (ESM-1). The relative proportions of these gases are highly variable (Fig. 10). FIs in shear zone-hosted samples (Cigar Main and Cigar North-East Trend) are usually dominated by traces of CO_2, CH_4, and N_2; CH_4 being the dominant gas. H_2 and O_2 have only been detected within the deposit (U427-200, SF-731-05-445.9, WC372-457.9), in association with CO_2, CH_4, and/or N_2. The samples occurring outside of the structures contain only traces of CO_2 (WC254-460.5; Fig. 10).

5.6. Chemical composition of the basinal fluids and spatial distribution

Overall, fluid inclusion compositions in the vicinity of the Cigar Lake deposit demonstrate a continuum between a Cl>Na>Ca>Mg>K end-member and a Cl>Ca≈Mg>Na>K end-member. The proportion of analysed FIs with element concentrations above the LOD is indicated in Table 2. A significant evolution in fluid composition is observed from barren areas away from Cigar Lake to the Cigar Main shear zone and the deposit area, confirming the trend deduced from microthermometry (Fig. 11).

In the barren Cigar North-East Trend (sample WC473-440.8), the FIs located in the basement are dominated by NaCl-rich brines. They plot along the 1:1 slope in the [Na + K] vs. 2 [Ca + Mg] binary diagram (main monovalent cations vs. main divalent cations). This slope indicates cationic exchange at constant charge, i.e. at constant chlorinity (4.5 mol/kg).

In contrast, the compositions of the FIs trapped both in and above the E-W shear zone, outside the deposit area, emphasize an additional process in addition to the Na ↔ (Ca ± Mg) cationic

exchange: an increase in the content of divalent cations. Such increase occurs with a relative constant content of monovalent cation (mainly Na) and expresses a compositional evolution toward higher chlorinities (from 4.5 to 6.1 mol/kg). This evolution occurs along with an enrichment in Mg, K, Mn, Ba, Sr, B, U and a depletion of Li (ESM-1, Fig. 12).

Directly below the deposit, the trapped FIs are $CaCl_2$-rich. They show the same general features as the FIs trapped along the E-W shear zone, but with even more evolved compositions. Compared to the NaCl-rich fluid trapped in the barren Cigar North-East Trend, here, the FIs show a very high chlorinity (around 6.5 mol/kg), a strong depletion of Na (from about 2 to almost 0 mol/kg) and Li (from about 36 to 8.4 mmol/kg), and a strong enrichment in Ca (from about 1 to 2.5 mol/kg), Mg (from about 150 to 490 mmol/kg), K (from about 110 to 280 mmol/kg), Mn (from about 7.5 to 10 mmol/kg), Ba (from 2.7 about to 24 mmol/kg), Sr (from about 11 to 23 mmol/kg), B (from about 2 to 5 mmol/kg), Zn (from about 2 to 6 mmol/kg), Pb (from about 0.8 to 2.5 mmol/kg), U (from about 0.03 to 0.3 mmol/kg), Sb (from about 0.12 to 0.6 mmol/kg) (ESM-1, Fig. 11 and 12). This compositional evolution translates into an enrichment in the Mg content of about × 1.4 to × 5.9, in K of about × 1.8 to × 5.8, in Mn of 0 up to × 3.6, in Ba of about × 1.3 to × 32.2, in Sr of about × 1.4 to × 3.4, in B of about 1.2 to × 4.9 and finally in U of about × 2.5 to × 388, and a depletion of Li of about 60 to 100% (ESM-1, Fig. 13). The Cu, Fe, Zn and Pb contents show an erratic behavior during this evolution, with highly variable contents in both brines, making evaluation of their concentrations difficult (ESM-1 and Fig. 13).

5.7. Orientations and surface density of fluid inclusions planes

The fluid inclusions planes (FIPs) from basement rocks were divided into two distinguishable groups, as previously proposed by Mercadier et al. (2010) and Martz et al. (2017): i) C-dominated (carbonic) FIPs formed during basement uplift and before the deposition of the Athabasca Basin, and ii) basinal brine (aqueous) FIPs, linked to the major stages of U body

647 formation at ca. 1.46 - 1.29 Ga (Fayek et al., 2002; Martz, 2017; Philippe et al., 1993). Some
648 mixed FIPs, with both types of fluids, correspond to metamorphic FIPs reopened and
649 cemented by brines (Fig. 3D). Most FIPs, whatever their nature, occur in orientations both
650 perpendicular and parallel to the foliation (Fig. 14). In addition, some local orientations (Fig.
651 14) are observed: N0°, observable in samples from the drill hole WC-448, corresponds to a
652 structurally more complex area, and N140-N170° plus N50°-N70° FIPs, found in some
653 samples located along the E-W conductor (WC372, WC335, and WC313, for example). At
654 the sample scale, aqueous brine FIPs show the same main orientations as the carbonic and
655 mixed FIPs.
656 The FIP density(σ_s) and quartz fracture paleoporosity(φ) of the quartz microfracture network
657 at the time of both carbonic fluid migration and brine migration has been estimated for each
658 sample by FIP mapping (Fig. 15). The density and associated quartz fracture paleoporosity
659 based on mixed FIPs have been added to those measured and calculated for both carbonic and
660 brine FIPs, as the mixed FIPs record both types of fluid migration. Table 3 summarizes the
661 geometrical parameters used for quartz paleoporosity reconstruction. There is a significant
662 difference in the density of the microfracture network around the Cigar Main shear zone
663 (cross-section C-D, Fig. 2) compared to the other structures, such as the Cigar North-East
664 Trend (cross-section E-F, Fig. 2). For example, in the 20 m surrounding each structure, the
665 reconstructed quartz fracture paleoporosity during basement uplift (i.e. during carbonic fluid
666 migration) are higher in Cigar Main (from 2.5 to 15.8 %, Fig. 15) compared to Cigar North-
667 East Trend (from 4.6 to 7.6%, Fig. 15). In the same way, the overall quartz fracture
668 paleoporosity at the time of brine migration is higher in the rocks from Cigar Main (from
669 0.3% up to 7.8 % toward the fault core) compared to the samples from the Cigar North-East
670 Trend (below 2%). Similarly, samples from the Power Line structure (drill hole WC466A,

671 Fig. 2) and structures away from the shear zones (drill hole WC254, Fig. 2) also show a very
672 low quartz fracture porosity at the time of brine migration (Table 3).
673 FIP mapping of pelitic gneiss samples occurring in the Cigar Main structure show somewhat
674 different features. They have very low quartz fracture paleoporosity based on brine FIPs (<
675 1%) relative to both the paleoporosity determined for pegmatites in this area and the high
676 paleoporosity based on carbonic FIPs (3.8 to 7.7 %) (Table 3).
677

678 # 6. Discussion

679 ## 6.1. Conversion of NaCl-rich brine into $CaCl_2$-rich brine during fluid
680 migration through the basement

681 The earliest brine end-member is represented by the NaCl-rich fluid found in quartz
682 overgrowths from barren ("regional") sandstones where dickite preservation attests to the lack
683 of subsequent fluid circulations, particularly in areas away from reactivated basement
684 structures (Fig. 8 and 9). This NaCl-rich fluid presents restricted ranges for Th and salinity,
685 with values between 84 and 121°C and 15.7 to 25.6 wt. % eq. NaCl + $CaCl_2$. This brine is
686 similar to that described elsewhere in Athabasca ore deposits and considered as a primary
687 evaporitic brine (Derome et al., 2005; Richard et al., 2013, 2011). Depending on the
688 considered pressure regime, the pressure correction for this diagenetic fluid results in trapping
689 temperatures of i) around 90-150°C, assuming a typical 30-40 °C/km hydrostatic gradient
690 under a 2.5-5 km thick sedimentary cover (case A in Fig. 16.) or ii) around 120-220°C, if
691 lithostatic conditions are assumed (case B in Fig. 16.). A hydrostatic pressure regime is,
692 however, preferred because of the porous sandstone-dominated nature of the Athabasca strata
693 (Hoeve and Quirt, 1984) forming a relatively permeable environment (Chi et al., 2013).
694 $CaCl_2$-rich FIs, containing brines with variable low (Na/Na+Ca) ratios in between 0 and 0.65,
695 were almost exclusively trapped in sandstones and basement rocks along, above and all along

696 the reactivated E-W shear zone hosting the deposit, unlike the regionally-trapped NaCl-rich
697 fluid (Figs. 7, 8, 9, 12). Despite their own distinct spatial distributions, halogen and noble gas
698 systematics of both $CaCl_2$-rich and NaCl-rich FIs demonstrate that they share a common
699 origin; that being seawater that underwent evaporation up to epsomite saturation (Leisen et al.
700 2012a, Richard et al., 2011a, 2014). It is thus apparent that the $CaCl_2$-rich brine was derived
701 from the initial NaCl-rich brine through fluid-rock interactions in this particular area (as
702 proposed by Derome et al., 2005; and Richard et al., 2010, 2016).
703 All the basement rocks sampled along the E-W shear zone, even several km to the East of the
704 deposit, are marked by the same hydrothermal alteration associated with U deposition in the
705 Athabasca Basin (Alexandre et al., 2005; Halter, 1988; Hoeve and Quirt, 1984; Kister et al.,
706 2006, 2005; Ng et al., 2013; Pacquet and Weber, 1993, among others). However, the deposit
707 area is characterized by a much higher intensity of hydrothermal alteration, both in the
708 sandstone and the basement, indicating that the deposit formed where the brine-rock
709 interactions were the most developed (Hoeve and Quirt, 1984). Here, not only do the $CaCl_2$-
710 rich FIs occur in higher proportions (up to 100% of the total analyzed FIs per sample), but
711 they also show the highest Ca content (>1.5 mol/kg, Fig. 12), corresponding to the lowest
712 Tm_{ice} (Fig. 8, 9), and the highest chlorinity (about 6.5 mol/kg, Fig. 11). These points indicate
713 that the $CaCl_2$-rich brine is a direct product of the fluid-rock interactions between the initial
714 NaCl-rich brine and the basement lithologies within the reactivated shear zones. Additionally,
715 it also indicates that there is a chemical gradient in brine compositions along the main EW
716 corridor from the barren zones to the Cigar Lake deposit (Fig. 17).
717

718 ## 6.2. The Chlorine increase in the $CaCl_2$-rich brine

719 The noteworthy chlorinity increase of the $CaCl_2$ brine from that of the NaCl brine can be
720 explained from earlier experimental works. Burisch et al. (2016) investigated, through

721 leaching experiments, the chemical evolution of both pure water and NaCl-brine (25%wt.
722 NaCl) through cataclastic deformation (increases the fluid/rock ratio) in granite and gneisses
723 of compositions similar to those of the sub-Athabasca basement lithologies. They
724 demonstrated that grain size reduction through cataclasis strongly increased the chlorinity of
725 the percolating fluid via i) leaching of Cl-bearing minerals (micas, apatites), and iii) removal
726 of H_2O from the fluid by replacement of anhydrous minerals (feldspars and plagioclases) by
727 hydrated ones (clay minerals) (Bons et al., 2014; Gleeson et al., 2003; Stober and Bucher,
728 2004; Walter et al., 2016). Similarly, in the altered basement rocks of the Athabasca region,
729 the replacement of anhydrous minerals, such as feldspars, can explain the chlorinity increase.
730

731 ## 6.3. The Uranium uptake

732 Tectonically-controlled brine percolations have affected larger volumes than only clay-rich
733 halo surrounding the U ores. Consequently the volume of rock from which U was leached is
734 significantly larger than previously thought. Among the basement lithologies, pegmatites and
735 metapelitic gneisses are dominant. In those rocks, the hydrothermal alteration is expressed by
736 the progressive replacement of the primary mineralogy, (i.e. K-feldspars, plagioclases,
737 muscovites, biotites, retrograde Fe-rich chlorites, and some accessory minerals such as
738 monazites) by a clay mineral assemblage of illite and sudoite with accessory alkali-deficient
739 dravite and APS minerals replacing monazite. Basement alteration like this present at Cigar
740 Lake is similar to that described elsewhere in Athabasca (Alexandre et al., 2005; Gaboreau et
741 al, 2007; Mercadier et al., 2010; Ng et al., 2013, among others). This rock alteration is
742 characterized by a gain of Mg, Li, B, and H_2O, and a loss of Ca, Na, K, Fe, Mn, Ba, Sr, Pb,
743 and U during alteration (Alexandre et al., 2005, Mercadier, 2009).
744 The microthermometric and LA-ICP-MS analyses of brine inclusions show that the $CaCl_2$-
745 rich end-member is characterized, relative to the NaCl-rich one, by a higher chlorinity, higher

746 contents of Ca, K, Mg, B, Mn, Ba, Sr, and U, and lower contents of Na and Li (Fig. 13).
747 However, except for the conceptual model of variations of volume and major element
748 contents in the basement rocks provided in Alexandre et al. (2005), no clear geochemical
749 budget associated with the hydrothermal alteration of those rocks has been presented yet.
750 Nonetheless, the chemistry of the brine resulting from the brine-rock interactions in general
751 confirms the gains and losses shown by the whole rock lithogeochemistry. In particular, the
752 gain in U for the $CaCl_2$ brine reaches up to 400%, suggesting that uranium is extracted from
753 the basement rocks though the alteration of the main U-bearing accessory minerals, such as
754 through monazite to APS conversion (Gaboreau et al., 2007; Hecht and Cuney, 2000). This
755 study provides strong evidence for a basement-derived U source in the long-lasting debate
756 about the uranium source for unconformity-related deposits in the Athabasca Basin (Jefferson
757 et al., 2007; Kyser and Cuney, 2015 and references therein) and tackles previous arguments
758 stating that no large-volume high permeability altered basement rocks have been detected
759 beneath the Athabasca Basin (Hoeve and Quirt, 1984; Thomas et al., 1998).
760

761 ## 6.4. Structurally controlled fluid flow in the basement.

762 *Brine penetration into the basement*

763 The occurrence of brine FIPs cross-cutting magmatic quartz in almost all the studied
764 basement rocks, within and outside the Hudsonian structures, indicates that brine percolation
765 was ubiquitous in the studied area. Therefore, the basin/basement interface was not a
766 watertight interface and basinal brines percolated into the basement rocks at a larger scale
767 than previously estimated (Kotzer and Kyser, 1995; Mercadier et al., 2010a; Pascal et al.,
768 2016). In the Athabasca region, the maximum depth of brine inclusion occurrence so far
769 observed in the basement rocks is 400 m below the unconformity (Richard et al., 2016). It
770 may however be inferred that the brines could have percolated to even greater depths since

771 basinal brines with a chlorinity similar to the Athabasca brines have been observed elsewhere
772 down to several kilometers below the unconformity in crystalline basement rocks (Boiron et
773 al., 2010; Bons et al., 2014; Burisch et al., 2017a; Cathelineau and Boiron, 2010; Munz et al.,
774 1995). In addition, fluid flow simulations focussed on the case of the Athabasca Basin
775 proposed km-scale percolations of brines in the basement through reactivated structures (Chi
776 et al., 2014; Cui et al., 2012; Li et al., 2016).
777 The similar distributions of micro-fracture surface densities obtained for metamorphic C-
778 dominated fluid FIPs and brine FIPs along cross-sections perpendicular to shear zones (Fig.
779 15) indicate that the brine circulation was greatly influenced by the microfracture network
780 inherited from pre-Athabasca Hudsonian exhumation events. In addition, the same dominant
781 strike directions of the FIP networks of both the retrometamorphic and the brine events (Fig.
782 14) may also indicate that the stress directions were similar during those two events. In
783 comparison to the pegmatites, only a few brine FIPs were observed in the pelite gneisses,
784 regardless of proximity to the fault cores. Yet, the intense hydrothermal alteration (illite-
785 sudoite) displayed by these gneisses suggests that brines nonetheless percolated through these
786 rocks, probably along the foliation planes.
787
788 *Brine fluid flow*
789 Fluid flow is demonstrated by the increased number of brine FIPs, and therefore an enhanced
790 microfracture paleoporosity, toward the damage zones of the main shear zones (Fig. 15). The
791 shear zones themselves are frequently occupied by glide planes full of graphite and pyrite that
792 decrease their permeability. This is a typical feature of the distribution of permeability around
793 faults, as shown for present day fluid flows in basement reservoirs (eg. the Soultz hot dry rock
794 project; Géraud et al., 2010) and rift faults (Dimmen et al., 2017; Kristensen et al., 2016). The
795 overall global structure of a shear zone includes a fault core surrounded by damage zone

796 domains that are characterized by minor faults and an overall enhanced fracture density
797 compared to the protolith (Bense et al., 2013; Caine et al., 1996). The damage zones within
798 the Athabasca basement faults, in particular within the complex association of graphite-rich
799 gneisses and lenses of pegmatite, show an increase in number, length, aperture, and
800 connectivity of microfractures, healed in the case of quartz, and sometimes filled by pyrite,
801 graphite, and chlorite. These features result in an increased permeability towards the fault
802 plane over around 20 to 40 meters (Fig. 15), whereas the fault core itself is characterized by a
803 lower permeability graphitic and clay-rich breccia with microfissures being clogged by clay
804 minerals, graphite-rich shear planes, and shear-related grain size reduction.
805
806 *Lateral evolution from barren zones towards the ore deposit.*
807 There is an increased degree of host-rock alteration around the ore deposit that is expressed
808 by the enhanced development of clay minerals at the expense of feldspars, the total bleaching
809 of the rock due to the total disappearance of mafic minerals (Fe-Mg phyllosilicates [biotite,
810 chlorite], amphiboles), and in the most intense alteration facies, total dissolution of quartz
811 (Pacquet and Weber, 1993). This enhanced alteration was favored by: i) increased focused
812 brine flow resulting from increased deformation rate, and ii) maintenance of favorable
813 mineral reaction conditions for a period of sufficient length. As the main E-W Cigar Main
814 fault corridor extends for more than 10 kilometers, the local increases in permeability and
815 fluid flow around the deposit needs to be explained by an additional local factor. The largest
816 zones of fluid percolation correspond to volumes at the intersection of faults where the
817 damage zones are larger (Dimmen et al., 2017). Therefore, the higher fluid flows and efficient
818 fluid conduits occur where the structural complexity is highest, such as in the Cigar Lake
819 area. This structural complexity is caused by: i) a series of N-S to NNE-SSW faults that
820 intersect the main E-W graphite-bearing fault corridor, and ii) potential stress perturbation

causing wider fracture apertures and further increase permeability in areas of fault interactions. A precise lithological and structural map of the basement at around the 500 m depth level is unfortunately not available, thus making difficult identification of the main causes for the enhanced permeability.

6.5. P-T conditions of fluid mixing and fluid flow mechanisms in and above reactivated basement-hosted shear zones

FIs show varying Tm_{ice} and varying (Na/Na+Ca) ratios in individual FIAs both in the euhedral quartz (Q_3) in the sandstones above the E-W structure and in the basement rocks in the structure. This indicates that NaCl- and $CaCl_2$-rich brines specifically mixed within and above this structure. Knowing that the $CaCl_2$-rich brine results from the interactions between the initial NaCl-rich basinal brine and the basement rocks, it implies that the initial brine first percolated downward into the basement-hosted shear zone during reactivation. Then, this brine chemically reacted with the basement lithologies to form the $CaCl_2$-rich brine. This evolved brine was finally expulsed upward from the basement back into the sandstones where it mixed with the ubiquitous formation waters (i.e. the initial NaCl-rich brine). Fluid movement in the context of basin-basement interface is generally attributed either to temperature, pressure, deformation (Burisch et al., 2016b; Garven, 1995) or density gradients (Koziy et al., 2009). In the Athabasca case, fluid density gradients are unlikely as both fluids are brines with similar densities. Thermally-driven or pressure-driven fluid migration is thus envisaged. Around the reactivated shear zone, the FIs show a wide range of Th values (mainly between 80 and 170 °C) which is overall higher compared to the initial diagenetic fluid (80-120°C) (Figs 7, 8, and 9). At this time, no unequivocally independent temperature or pressure constraints exist and thus only assumptions on the geothermal gradients can be used to constrain the temperature and pressure trapping conditions of the $CaCl_2$ brines and the

846 subsequent mixing. Therefore, the overall higher Th range of the FIs in this area can be
847 interpreted through two scenarios that vary depending on the assumed pressure regime:
848
849 *Thermally-driven convection under a hydrostatic pressure regime*
850 Assumption of a typical 30-40 °C/km hydrostatic gradient (Peters et al., 2012) in the
851 Athabasca Basin during the trapping of the NaCl-rich brine implies initial P-T diagenetic
852 conditions of around 90-150°C under a 2.5-5 km thick sedimentary cover (Fig. 16).
853 Considering this thickness of sedimentary cover, the higher Th of the FIAs with mixed NaCl-
854 rich brines and $CaCl_2$-brines (up to 200°C) are best explained by a localized thermal
855 disturbance in the shear zone related to a high geothermal gradient (path A in Fig. 16). P-T
856 conditions occurring in the E-W shear zone at this time would thus be mainly 110-200 °C and
857 hydrostatic pressure would be around 250-500 bars with a geothermal gradient of 60°C/km.
858 Those conditions imply that the E-W shear zone was an area of thermal convection with
859 hotter fluids assending from deeper parts of the shear zone. Heat input can be attributed to
860 two main causes : i) heat derived from intrusives or mantle anomalies: there is no evidence of
861 intrusions at the time of formation of the deposit, and no clear geodynamic cause explaining
862 abnormal heat flows. ii) heat brought by the ascending fluids: this is the likely hypothesis for
863 explaining lateral thermal gradients. Thermal disturbance and convection in this area is
864 furthermore supported by the abundance of illite above the structure (Fig. 17) and especially
865 in the illite clay mineral halo above the deposit in which both *2M* and *3T* (now considered to
866 be *1Mc* and *1Mt*, respectively) illite polytypes have been described and whose crystallinity
867 indicates temperature of formation approximating 200 °C or more (Kister et al., 2005). Chu
868 and Chi (2016) considered also that some localities in the basin underwent upwelling fluid
869 convection. The shear zone hosting the deposit could have acted as an upwelling flow zone
870 from deeper zones in the basement to basin between two thermal convection cells

perpendicular to the structure as predicted earlier (Hoeve and Quirt, 1984) and through 2D numerical modeling (Li et al., 2016). Another possibility would be convection inside and parallel to the fault plane itself with possible upwelling sites corresponding to the areas showing abundant $CaCl_2$-FIPs and strong alteration features, such as those found below the deposit area (Fig. 17).

Deformation-driven convection under a hydrostatic pressure regime

In this scenario, the same initial typical gradient of 30-40 °C/km (Peters et al., 2012) is assumed, but this time under a lithostatic pressure regime. This implies initial P-T diagenetic conditions of around 120-220°C under a 2.5-7 km thick sedimentary cover (Fig. 16). In this scenario the higher Th recorded in the E-W shear zone could as well be explained by a pressure drop (path B in Fig. 16) due to change of pressure regime from lithostatic to hydrostatic during tectonic reactivation of the basement fault and propagation into the sandstone. Pressure changes during seismic pumping along the faults following the model of Sibson et al. (1975) and Behr et al. (1987) are in this way envisaged. The recent study of two-dimensional fluid flow modeling applied on the shear zones hosting the Gryphon and Phoenix U-deposits (Li et al., 2018) has shown that deformation-driven fluid flow in this context can result in both downward and upward flow at the same time depending on local heterogeneities in the basement geology under a common compressional stress field. In the case of the Cigar Lake deposit, such heterogeneities may have controlled the areas of upwelling or downwelling migrations in the same fault plane.

Finally, one additional fluid flow mechanism may have participated in either case especially for focusing the mineralizing brine in the ca. 2 km-long portion of the shear zone hosting the deposit. The dessication process (loss of water from the fluid) during the hydrolytic clay mineral formation would have been more intense in the alteration halo surrounding the

deposit and may have created a hydraulic gradient around the areas of higher fluid-rock interactions. This mechanism follows the "dessication suck" model proposed in the Variscan Schwarzwald (Germany) by Bons et al. (2014), Stober and Bucher (2004), and Walter et al. (2016).

In any case, the estimated P-T pairs are much above those proposed by Rabiei et al. (2017) for a low burial (<2.5 km) scenario and a P-T pair close to the L/V curve, yielding to subsequent boiling of the fluids. As no reliable aqueous vapor inclusions have been found in this study, the latter hypothesis can be ruled out. The very high thermal gradients linked to hydrothermal-epithermal systems are thus rather unprobable. However, hypotheses involving localized thermal anomalies are easier to understand, as fluids can convect deep into the basement and bring heat upwards from below.

6.6. Significance of the trace amounts of volatile in the brines

The studied FIs contain gases, with a specific spatial distribution between sandstone and basement, and between the deposit area, the E-W shear zone, and the other sampled zones. CH_4, N_2 and CO_2 are the dominant gases and are only observed in basement FIPs (Fig. 10). O_2 and H_2 are only detected in FIs located in the deposit area, in both sandstones and basement rocks. This latter restricted distribution is in agreement with a radiolytic origin (Derome et al., 2003; Richard, 2017). The occurrence of CH_4, N_2, and CO_2 in the brine FIs has been also recorded in other studies (Derome et al., 2005, 2003; Mercadier et al., 2010; Richard, 2017, among others). Increasing interest in those gases has developed in recent years since it has been shown that focused flow of such reduced gases along brittle faults could provide the needed reducing agents for the precipitation of uraninite from U^{VI} transported in oxidized brines (Burisch et al., 2017a; Dargent et al., 2015). The occurrence of trace amounts of CO_2, CH_4, and N_2 gases involves the interaction of the oxidizing basinal brines with the

graphite-bearing metapelitic gneisses, with alteration by the brines of NH_4-bearing feldspars and biotite and graphite destabilization (Richard, 2017). Such an explanation remains plausible and valid but it faces the difficulty that no clear evidence of graphite destabilization has been provided at this time.

The scale of the present study allows an alternative hypothesis to be expressed. The spatial distribution of the dominant gases appears to show a spatial distribution similar to that of the retrograde metamorphism-related C-O-H-N dominated FIs trapped in graphite-bearing shear zones (i.e. an evolution from pure CO_2 toward CO_2-CH_4-N_2-H_2O compositions with proximity to the graphite-rich fault cores, Martz et al., 2017). This observation, together with evidence of reopening of retrometamorphic carbonic FIPs (forming mixed FIPs), suggests instead that the trace amounts of gases detected in the brine FIs may result from the release of earlier C-O-H-N dominated fluids either trapped as FIPs in magmatic and metamorphic quartz or adsorbed on chlorite layers in the gneisses. If such a hypothesis is correct, it would mean that those trace amounts of gases cannot be used as proxies for focused flow of reducing agents and subsequently U deposition.

7. Conclusion

The systematic and multi-method analysis of brines trapped as fluid inclusions in both Athabasca Group sandstones and their basement rocks within a 25 km² area surrounding the Cigar Lake U deposit (Saskatchewan, Canada) has allowed the full description of the physico-chemical features of these fluids and their changes through time and space related to the genesis of this exceptional U deposit:

- The seawater-derived initial diagenetic NaCl-rich and Ca-poor brine of the Athabasca Basin percolated into most basement lithologies at temperatures ranging from 90 to 150 °C under a 2.5-5 km thick sedimentary cover. Thus the basin/basement interface is not a

946 watertight interface and basinal brines percolated into the basement rocks at a larger scale
947 than previously estimated.

948 - In quartz-rich basement rocks such as pegmatites, the similar abundance of micro-
949 fractures containing i) C-dominated fluid inclusions issued from fluid stages related to the
950 basement uplift (ca. 1.80 - 1.72 Ga) and ii) brine inclusions trapped at ca. 1.46-1.29 Ga,
951 indicate that the brine circulation was greatly influenced by the pre-existing microfracture
952 networks inherited from Hudsonian exhumation events. The increase in the density of FIP
953 surfaces along profiles perpendicular to shear zones reflect the fault damage zones that affect
954 the rocks over 20 to 40 m on both sides of the shear zones. These zones are where the basinal
955 fluid flows focused in the basement.

956 - In the damage zone of the reactivated E-W structure hosting the deposit, the
957 enhanced circulation of the NaCl-rich brine induced: i) the formation of the illite-sudoite-
958 dominated alteration that characterizes the unconformity-related U deposits, ii) the subsequent
959 chemical evolution of the NaCl-rich brine towards $CaCl_2$-rich and Mg, B, K, Mn, Ba, Sr, and
960 U-rich compositions, and iii) the chlorinity increase of the brines through desiccation by clay
961 precipitation during alteration. These processes were active all along the E-W shear zone, i.e.
962 on a scale of several kilometers, but their intensity increase significantly towards the deposit.

963 - There is a spatial correlation between the samples showing i) the highest intensity of
964 hydrothermal alteration, ii) the highest proportion of $CaCl_2$-rich brines, and iii) the FIs with
965 the highest Ca contents and salinities. This suggests that the $CaCl_2$-rich brine was a direct
966 product of the fluid-rock interactions between the initial NaCl-rich brine and the basement
967 lithologies. The fluids related to the U mineralization are thus the most evolved brines.

968 - The two brines mixed in and above the reactivated E-W shear zone. Based on the
969 assumed pressure regime, two scenarios can be proposed. i) The first one, which is also the
970 preferred one, involves thermally-driven convection occurring under hydrostatic pressure

regime with isobaric mixing at higher temperature (110-200 °C) in upwelling limbs of convection cells. ii) The second is defined by deformation-driven circulations occurring through seismic pumping and isothermal episodic pressure fluctuations from lithostatic to hydrostatic.

These conclusions provide new perspectives to the processes related to the genesis of unconformity-related U deposits and, at a broader scale, to the processes leading to the generation of Ca-dominated brines in basement rocks. This work strongly demonstrates that brine migration and/or convection into basement reactivated shear zones is a key and indispensable process for the development of the ore-forming fluid and thus for U-deposit formation.

8. Acknowledgments

This work was carried out as part of a PhD thesis done in the CREGU, GeoRessources, Université de Lorraine (Nancy, France), and entirely supported by AREVA Resources CANADA (ARC). We thank AREVA for the permission to publish these results. We also thank Cameco Corporation for logistical assistance during the sampling. We are grateful to Antonin Richard for fruitful discussions and help with the LA-ICP-MS data treatment. Marie-Camille Caumon is thanked for Raman data acquisition and treatment, and Lise Salsi from the SCMEM for the SEM pictures. This work has been carried out thanks to the access to the analytical capabilities of the GeoRessources laboratory (Université de Lorraine, CNRS, CREGU), with equipment financed by the CPER program (national funds-Lorraine Region-FEDER) and Labex Ressources 21 (supported by the French National Research Agency through the national program 'Investissements d'avenir' with reference ANR-10-LABX-21—LABEX RESSOURCES 21). The authors also thank Dr. Mathias Burisch and Dr. Gregor

995 Markl for their detailed reviews that helped to improve a former version of this manuscript,
996 and both Dr. Klaus Mezger and Dr. Alexandre Tarantola for editorial handling.
997

998 ## 9. References

999 Alexandre, P., Kyser, K., Polito, P., Thomas, D., 2005. Alteration mineralogy and stable
1000 isotope geochemistry of Paleoproterozoic basement-hosted unconformity-type uranium
1001 deposits in the Athabasca Basin, Canada. Econ. Geol. 100, 1547–1563.
1002 Alexandre, P., Kyser, K., Thomas, D., Polito, P., Marlat, J., 2007. Geochronology of
1003 unconformity-related uranium deposits in the Athabasca Basin, Saskatchewan, Canada
1004 and their integration in the evolution of the basin. Miner. Depos. 44, 41–59.
1005 doi:10.1007/s00126-007-0153-3
1006 Alexandre, P., Kyser, T.K., 2005. EFFECTS OF CATIONIC SUBSTITUTIONS AND
1007 ALTERATION IN URANINITE, AND IMPLICATIONS FOR THE DATING OF
1008 URANIUM DEPOSITS. Can. Mineral. 43, 1005–1017. doi:10.2113/gscanmin.43.3.1005
1009 Allan, M.M., Yardley, B.W., Forbes, L.J., Shmulovich, K.I., Banks, D.A., Shepherd, T.J.,
1010 2005. Validation of LA-ICP-MS fluid inclusion analysis with synthetic fluid inclusions.
1011 Am. Mineral. 90, 1767–1775.
1012 Annesley, I.R., Madore, C., Portella, P., 2005. Geology and thermotectonic evolution of the
1013 western margin of the Trans-Hudson Orogen: evidence from the eastern sub-Athabasca
1014 basement, Saskatchewan. Can. J. Earth Sci. 42, 573–597. doi:10.1139/e05-034
1015 Bakker, R.J., 2003. Package FLUIDS 1. Computer programs for analysis of fluid inclusion
1016 data and for modelling bulk fluid properties. Chem. Geol. 194, 3–23.
1017 doi:10.1016/S0009-2541(02)00268-1
1018 Beaufort, D., Patrier, P., Laverret, E., Bruneton, P., Mondy, J., 2005. Clay alteration
1019 associated with proterozoic unconformity-type uranium deposits in the East Alligator

1020 Rivers uranium field, Northern Territory, Australia. Econ. Geol. 100, 515–536.
1021 doi:10.2113/gsecongeo.100.3.515
1022 Becker, S.P., Eichhubl, P., Laubach, S.E., Reed, R.M., Lander, R.H., Bodnar, R.J., 2010. A 48
1023 m.y. history of fracture opening, temperature, and fluid pressure: Cretaceous Travis Peak
1024 Formation, East Texas basin. GSA Bull. 122.
1025 Becker, S.P., Fall, A., Bodnar, R.J., 2008. Synthetic fluid inclusions. XVII. PVTX properties
1026 of high salinity H 2 O-NaCl solutions (> 30 wt% NaCl): Application to fluid inclusions
1027 that homogenize by halite disappearance from porphyry copper and other hydrothermal
1028 ore deposits. Econ. Geol. 103, 539–554.
1029 Bense, V.F., Gleeson, T., Loveless, S.E., Bour, O., Scibek, J., 2013. Fault zone hydrogeology.
1030 Earth-Science Rev. 127, 171–192.
1031 Boiron, M.-C., Cathelineau, M., Richard, A., 2010. Fluid flows and metal deposition near
1032 basement/cover unconformity: lessons and analogies from Pb-Zn-F-Ba systems for the
1033 understanding of Proterozoic U deposits. Geofluids 10, 270–292. doi:10.1111/j.1468-
1034 8123.2010.00289.x
1035 Bons, P.D., Fusswinkel, T., Gomez-Rivas, E., Markl, G., Wagner, T., Walter, B., 2014. Fluid
1036 mixing from below in unconformity-related hydrothermal ore deposits. Geology 42,
1037 1035–1038. doi:10.1130/G35708.1
1038 Bruneton, P., 1993. Geological environment of the Cigar Lake uranium deposit. Can. J. Earth
1039 Sci. 30, 653–673.
1040 Burisch, M., Gerdes, A., Walter, B.F., Neumann, U., Fettel, M., Markl, G., 2017a. Methane
1041 and the origin of five-element veins: mineralogy, age, fluid inclusion chemistry and ore
1042 forming processes in the Odenwald, SW Germany. Ore Geol. Rev. 81, 42–61.
1043 Burisch, M., Marks, M.A.W., Nowak, M., Markl, G., 2016a. The effect of temperature and
1044 cataclastic deformation on the composition of upper crustal fluids — An experimental

1045 approach. Chem. Geol. 433, 24–35. doi:10.1016/j.chemgeo.2016.03.031
1046 Burisch, M., Walter, B.F., Markl, G., 2017b. Silicification of Hydrothermal Gangue Minerals
1047 In Pb-Zn-Cu-Fluorite-Quartz-Baryte Veins. Can. Mineral. 55, 501–514.
1048 Burisch, M., Walter, B.F., Wälle, M., Markl, G., 2016b. Tracing fluid migration pathways in
1049 the root zone below unconformity-related hydrothermal veins: Insights from trace
1050 element systematics of individual fluid inclusions. Chem. Geol. 429, 44–50.
1051 Caine, J.S., Evans, J.P., Forster, C.B., 1996. Fault zone architecture and permeability
1052 structure. Geology 24, 1025–1028.
1053 Cathelineau, M., Boiron, M.-C., 2010. Downward penetration and mixing of sedimentary
1054 brines and dilute hot waters at 5km depth in the granite basement at Soultz-sous-Forêts
1055 (Rhine graben, France). Comptes Rendus Geosci. 342, 560–565.
1056 doi:10.1016/j.crte.2009.08.010
1057 Chi, G., Bosman, S., Card, C., 2013. Numerical modeling of fluid pressure regime in the
1058 Athabasca basin and implications for fluid flow models related to the unconformity-type
1059 uranium mineralization. J. Geochemical Explor. 125, 8–19.
1060 doi:10.1016/j.gexplo.2012.10.017
1061 Chi, G., Li, Z., Bethune, K., 2014. Numerical modeling of hydrocarbon generation in the
1062 Douglas Formation of the Athabasca basin (Canada) and implications for unconformity-
1063 related uranium mineralization. J. Geochemical Explor. 144, 37–48.
1064 doi:10.1016/j.gexplo.2013.10.015
1065 Chu, H., Chi, G., 2016. Thermal profiles inferred from fluid inclusion and illite
1066 geothermometry from sandstones of the Athabasca basin: Implications for fluid flow and
1067 unconformity-related uranium mineralization. Ore Geol. Rev. 75, 284–303.
1068 doi:10.1016/j.oregeorev.2015.12.013
1069 Cox, S.F., 2005. Coupling between deformation, fluid pressures, and fluid flow in ore-

producing hydrothermal systems at depth in the crust. Econ. Geol. 100th anni, 39–75.

Cui, T., Yang, J., Samson, I.M., 2012. Tectonic Deformation and Fluid Flow: Implications for the Formation of Unconformity-Related Uranium Deposits. Econ. Geol. 107, 147–163. doi:10.2113/econgeo.107.1.147

Dargent, M., Truche, L., Dubessy, J., Bessaque, G., Marmier, H., 2015. Reduction kinetics of aqueous U(VI) in acidic chloride brines to uraninite by methane, hydrogen or C-graphite under hydrothermal conditions: Implications for the genesis of unconformity-related uranium ore deposits. Geochim. Cosmochim. Acta 167, 11–26. doi:10.1016/j.gca.2015.06.027

Dehoff, R.., Rhines, F.N.., 1972. Microscopie Quantitative.

Derome, D., Cathelineau, M., Cuney, M., Fabre, C., Lhomme, T., Banks, D., 2005. Mixing of sodic and calcic brines and uranium deposition at McArthur River, Saskatchewan, Canada: a Raman and laser-induced breakdown spectroscopic study of fluid inclusions. Econ. Geol. 100, 1529–1545. doi:10.2113/gsecongeo.100.8.1529

Derome, D., Cathelineau, M., Lhomme, T., Curley, M., 2003. Fluid inclusion evidence of the differential migration of H2 and O2in the McArthur River unconformity-type uranium deposit (Saskatchewan, Canada). Possible role on post-ore modifications of the host rocks. J. Geochemical Explor. 78–79, 525–530. doi:10.1016/S0375-6742(03)00114-6

Dimmen, V., Rotevatn, A., Peacock, D.C.P., Nixon, C.W., Nærland, K., 2017. Quantifying structural controls on fluid flow: Insights from carbonate-hosted fault damage zones on the Maltese Islands. J. Struct. Geol. 101, 43–57.

Earle, S., 1997. MINSPEC3 program for estimation of clay contents in Athabasca Group sandstones from reflectance spectral data. Internal Report, Grasswood Geosciences.

Earle, S., 1996. MINSPEC1 and CALSPEC1 interactive graphical programs for quantitative analysis of clay minerals from relectance data and for assessment of PIMA II calibration

spectra. Internal Report, Grasswood Geosciences.

Essarraj, S., Boiron, M.-C., Cathelineau, M., Tarantola, A., Leisen, M., Boulvais, P., Maacha, L., 2016. Basinal Brines at the Origin of the Imiter Ag-Hg Deposit (Anti-Atlas, Morocco): Evidence from LA-ICP-MS Data on Fluid Inclusions, Halogen Signatures, and Stable Isotopes (H, C, O). Econ. Geol. 111.

Essarraj, S., Boiron, M.C., Cathelineau, M., Banks, D.A., Benharref, M., 2005. Penetration of surface-evaporated brines into the Proterozoic basement and deposition of Co and Ag at Bou Azzer (Morocco): Evidence from fluid inclusions. J. African Earth Sci. 41, 25–39. doi:10.1016/J.JAFREARSCI.2005.03.001

Fayek, M., Harrison, T.M., Ewing, R.C., Grove, M., Coath, C.D., 2002. O and Pb isotopic analyses of uranium minerals by ion microprobe and U-Pb ages from the Cigar Lake deposit. Chem. Geol. 185, 205–225. doi:10.1016/S0009-2541(01)00401-6

Feltrin, L., Oliver, N.H.S., Kelso, I.J., King, S., 2003. Basement metal scavenging during basin evolution: Cambrian and Proterozoic interaction at the Century ZnPbAg Deposit, Northern Australia. J. Geochemical Explor. 78, 159–162.

Fisher, L.A., Cleverley, J.S., Pownceby, M., MacRae, C., 2013. 3D representation of geochemical data, the corresponding alteration and associated REE mobility at the Ranger uranium deposit, Northern Territory, Australia. Miner. Depos. 48, 947–966. doi:10.1007/s00126-013-0463-6

Fouques, J.P.R., Knipping, H.D.D., Schimann, K., Fowler, M., Knipping, H.D.D., Schimann, K., 1986. The Cigar Lake uranium deposit: Discovery and general characteristics, in: E.L. Evans, Ed., Uranium Deposits of Canada: Canadian Institute of Mining and Metallurgy Special Volume 33. pp. 218–229.

Fusswinkel, T., Wagner, T., Wälle, M., Wenzel, T., Heinrich, C.A., Markl, G., 2013. Fluid mixing forms basement-hosted Pb-Zn deposits: Insight from metal and halogen

1120 geochemistry of individual fluid inclusions. Geology 41, 679–682.
1121 Gaboreau, S., Cuney, M., Quirt, D., Beaufort, D., Patrier, P., Mathieu, R., 2007. Significance
1122 of aluminum phosphate-sulfate minerals associated with U unconformity-type deposits:
1123 The Athabasca basin, Canada. Am. Mineral. 92, 267–280. doi:10.2138/am.2007.2277
1124 Garven, G., 1995. Continental-Scale Groundwater Flow and Geologic Processes. Annu. Rev.
1125 Earth Planet. Sci. 23, 89–117. doi:10.1146/annurev.ea.23.050195.000513
1126 Géraud, Y., Rosener, M., Surma, F., Place, J., Le Garzic, É., Diraison, M., 2010. Physical
1127 properties of fault zones within a granite body: example of the Soultz-sous-Forêts
1128 geothermal site. Comptes Rendus Geosci. 342, 566–574.
1129 Gleeson, S.A., Wilkinson, J.J., Stuart, F.M., Banks, D.A., 2001. The origin and evolution of
1130 base metal mineralising brines and hydrothermal fluids, South Cornwall, UK. Geochim.
1131 Cosmochim. Acta 65, 2067–2079.
1132 Gleeson, S.A., Yardley, B.W.D., Munz, I.A., Boyce, A.J., 2003. Infiltration of basinal fluids
1133 into high-grade basement, South Norway: sources and behaviour of waters and brines.
1134 Geofluids 3, 33–48. doi:10.1046/j.1468-8123.2003.00047.x
1135 Gomila, R., Arancibia, G., Mitchell, T.M., Cembrano, J.M., Faulkner, D.R., 2016.
1136 Palaeopermeability structure within fault-damage zones: A snap-shot from microfracture
1137 analyses in a strike-slip system. J. Struct. Geol. 83, 103–120.
1138 doi:10.1016/j.jsg.2015.12.002
1139 Guillong, M., Meier, D.L., Allan, M.M., Yardley, B.W.D., 2008. SILLS: A MATLAB-based
1140 program for the reduction of laser ablation ICP-MS data of homogeneous materials and
1141 inclusions, in: Laser Ablation ICP-MS in the Earth Sciences: Current Practices and
1142 Outstanding Issues, Vol 40. Mineralogical Association of Canada Short Course Series.
1143 Vancouver, pp. 328–333.
1144 Günther, D., Frischknecht, R., Heinrich, C.A., Kahlert, H.-J., 1997. Capabilities of an Argon

Fluoride 193 nm Excimer Laser for Laser Ablation Inductively Coupled Plasma Mass Spectometry Microanalysis of Geological Materials. J. Anal. At. Spectrom. 12, 939–944. doi:10.1039/A701423F

Halter, G., 1988. Zonalite des alterations dans l'environnement des gisements d'uranium associes a la discordance du proterozoique moyen (Saskatchewan, Canada). Thèse de 3ème cycle, Université de Strasbourg, Strasbourg, France.

Hecht, L., Cuney, M., 2000. Hydrothermal alteration of monazite in the Precambrian crystalline basement of the Athabasca Basin (Saskatchewan, Canada): implications for the formation of unconformity-related uranium deposits. Miner. Depos. 35, 791–795. doi:10.1007/s001260050280

Heijlen, W., Muchez, P., Banks, D.A., Schneider, J., Kucha, H., Keppens, E., 2003. Carbonate-Hosted Zn-Pb Deposits in Upper Silesia, Poland: Origin and Evolution of Mineralizing Fluids and Constraints on Genetic Models. Econ. Geol. 98, 911–932. doi:10.2113/gsecongeo.98.5.911

Hoeve, J., Quirt, D., 1984. Mineralization and host rock alteration in relation to clay mineral diagenesis and evolution of the middle Proterozoic Athabasca basin, northern Saskatchewan, Canada. Research council technical repport No. 187.

Hoeve, J., Sibbald, T.I.I., 1978. On the genesis of Rabbit Lake and other unconformity-type uranium deposits in northern Saskatchewan, Canada. Econ. Geol. 73, 1450–1473. doi:10.2113/gsecongeo.73.8.1450

Jeanneret, P., Goncalves, P., Durand, C., Trap, P., Marquer, D., Quirt, D., Ledru, P., 2016. Tectono-metamorphic evolution of the pre-Athabasca basement within the Wollaston–Mudjatik Transition Zone, Saskatchewan. Can. J. Earth Sci. 53, 231–259. doi:10.1139/cjes-2015-0136

Jefferson, C.W., Thomas, D.J., Gandhi, S.S., Ramaekers, P., Delaney, G., Brisbin, D., Cutts,

C., Portella, P., Olson, R. a., 2007. Unconformity-associated uranium deposits of the Athabasca basin, Saskatchewan and Alberta. Bull. Geol. Surv. Canada 23–67.

Jochum, K.P., Weis, U., Stoll, B., Kuzmin, D., Yang, Q., Raczek, I., Jacob, D.E., Stracke, A., Birbaum, K., Frick, D.A., Günther, D., Enzweiler, J., 2011. Determination of Reference Values for NIST SRM 610-617 Glasses Following ISO Guidelines. Geostand. Geoanalytical Res. 35, 397–429. doi:10.1111/j.1751-908X.2011.00120.x

Kendrick, M.A., Burgess, R., Harrison, D., Bjørlykke, A., 2005. Noble gas and halogen evidence for the origin of Scandinavian sandstone-hosted Pb-Zn deposits. Geochim. Cosmochim. Acta 69, 109–129.

Kister, P., Laverret, E., Quirt, D., Cuney, M., Patrier Mas, P., Beaufort, D., Bruneton, P., 2006. Mineralogy and geochemistry of the host-rock alterations associated with the Shea Creek unconformity-type uranium deposits (Athabasca Basin, Saskatchewan, Canada). Part 2. Regional-scale spatial distribution of the Athabasca Group sandstone matrix mineral. Clays Clay Miner. 54, 295–313. doi:10.1346/CCMN.2006.0540302

Kister, P., Vieillard, P., Cuney, M., Quirt, D., Laverret, E., 2005. Thermodynamic constraints on the mineralogical and fluid composition evolution in a clastic sedimentary basin: the Athabasca Basin (Saskatchewan, Canada). Eur. J. Mineral. 17, 325–341. doi:10.1127/0935-1221/2005/0017-0325

Kotzer, T.G., Kyser, T.K., 1995. Petrogenesis of the Proterozoic Athabasca Basin, northern Saskatchewan, Canada, and its relation to diagenesis, hydrothermal uranium mineralization and paleohydrogeology. Chem. Geol. 120, 45–89. doi:10.1016/0009-2541(94)00114-N

Koziy, L., Bull, S., Large, R., Selley, D., 2009. Salt as a fluid driver, and basement as a metal source, for stratiform sediment-hosted copper deposits. Geology 37, 1107–1110. doi:10.1130/G30380A.1

1195 Kristensen, T.B., Rotevatn, A., Peacock, D.C.P., Henstra, G.A., Midtkandal, I., Grundvåg, S.-
1196 A., 2016. Structure and flow properties of syn-rift border faults: The interplay between
1197 fault damage and fault-related chemical alteration (Dombjerg Fault, Wollaston Forland,
1198 NE Greenland). J. Struct. Geol. 92, 99–115.
1199 Kyser, K., Cuney, M., 2015. Basins and uranium deposits, In: Geology and Geochemistry of
1200 Uranium and Thorium Deposits, Short Course Series, Vol. 46. pp. 224–250.
1201 Lach, P., Mercadier, J., Dubessy, J., Boiron, M.-C., Cuney, M., 2013. In Situ Quantitative
1202 Measurement of Rare Earth Elements in Uranium Oxides by Laser Ablation-Inductively
1203 Coupled Plasma-Mass Spectrometry. Geostandars Geoanalytical Res. 37, 277–296.
1204 doi:10.1111/j.1751-908X.2012.00161.x
1205 Lander, R.H., Laubach, S.E., 2015. Insights into rates of fracture growth and sealing from a
1206 model for quartz cementation in fractured sandstones. GSA Bull. 127.
1207 Laverret, E., Mas, P.P., Beaufort, D., Kister, P., Quirt, D., Bruneton, P., Clauer, N., Patrier
1208 Mas, P., Beaufort, D., Kister, P., Quirt, D., Bruneton, P., Clauer, N., 2006. Mineralogy
1209 and geochemistry of the host-rock alterations associated with the Shea Creek
1210 unconformity-type uranium deposits (Athabasca Basin, Saskatchewan, Canada). Part 1.
1211 Spatial variation of illite properties. Clays Clay Miner. 54, 275–294.
1212 doi:10.1346/CCMN.2006.0540301
1213 Lecumberri-Sanchez, P., Steele-MacInnis, M., Bodnar, R.J., 2012. A numerical model to
1214 estimate trapping conditions of fluid inclusions that homogenize by halite disappearance.
1215 Geochim. Cosmochim. Acta 92, 14–22. doi:10.1016/J.GCA.2012.05.044
1216 Leisen, M., Boiron, M.C., Richard, A., Dubessy, J., 2012. Determination of Cl and Br
1217 concentrations in individual fluid inclusions by combining microthermometry and LA-
1218 ICPMS analysis: Implications for the origin of salinity in crustal fluids. Chem. Geol.
1219 330–331, 197–206. doi:10.1016/j.chemgeo.2012.09.003

1220 Lespinasse, M., Désindes, L., Fratczak, P., Petrov, V., 2005. Microfissural mapping of natural
1221 cracks in rocks: Implications for fluid transfers quantification in the crust. Chem. Geol.
1222 223, 170–178. doi:10.1016/j.chemgeo.2005.05.009
1223 Li, Z., Chi, G., Bethune, K.M., 2016. The effects of basement faults on thermal convection
1224 and implications for the formation of unconformity-related uranium deposits in the
1225 Athabasca Basin, Canada. Geofluids. doi:10.1111/gfl.12180
1226 Li, Z., Chi, G., Bethune, K.M., Eldursi, K., Thomas, D., Quirt, D., Ledru, P., 2018.
1227 Synchronous egress and ingress fluid flow related to compressional reactivation of
1228 basement faults: the Phoenix and Gryphon uranium deposits, southeastern Athabasca
1229 Basin, Saskatchewan, Canada. Miner. Depos. 53, 277–292.
1230 Lodemann, M., Fritz, P., Wolf, M., Ivanovich, M., Hansen, B.T., Nolte, E., 1997. On the
1231 origin of saline fluids in the KTB (continental deep drilling project of Germany). Appl.
1232 Geochemistry 12, 831–849. doi:10.1016/S0883-2927(97)00085-1
1233 Longerich, H.P., Jackson, S.E., Günther, D., Fryer, B.J., 1996. Inter-laboratory note. Laser
1234 ablation inductively coupled plasma mass spectrometric transient signal data acquisition
1235 and analyte concentration calculation. J. Anal. At. Spectrom. 11, 899–904.
1236 doi:10.1039/JA9961100899
1237 Longerich, H.P., Jenner, G.A., Fryer, B.J., Jackson, S.E., 1990. Inductively coupled plasma-
1238 mass spectrometric analysis of geological samples: A critical evaluation based on case
1239 studies. Chem. Geol. 83, 105–118. doi:10.1016/0009-2541(90)90143-U
1240 Macdonald, C.C., 1980. Mineralogy and geochemistry of a precambrian regolith in the
1241 Athabasca Basin, in: Master Thesis, University of Saskatchewan. p. 151.
1242 Markl, G., Burisch, M., Neumann, U., 2016. Natural fracking and the genesis of five-element
1243 veins. Miner. Depos. 51, 703–712.
1244 Martz, P., 2017. Caractéristiques, chronologie et rôles des circulations fluides dans le bassin

d'Athabasca et de son socle: implications dans la formation et l'évolution du gisement d'uranium de Cigar Lake. Characteristics, chronology and roles of fluid circulations in t.

Martz, P., Cathelineau, M., Mercadier, J., Boiron, M.-C., Jaguin, J., Tarantola, A., Demacon, M., Gerbeaud, O., Quirt, D., Doney, A., 2017. C-O-H-N fluids circulations and graphite precipitation in reactivated Hudsonian shear zones during basement uplift of the Wollaston-Mudjatik Transition Zone: Example of the Cigar Lake U deposit. Lithos 294–295, 222–245. doi:https://doi.org/10.1016/j.lithos.2017.10.001

McGowan, R.R., Roberts, S., Boyce, A.J., 2006. Origin of the Nchanga copper–cobalt deposits of the Zambian Copperbelt. Miner. Depos. 40, 617.

McKechnie, C.L., Annesley, I.R., Ansdell, K.M., 2012. MEDIUM- TO LOW-PRESSURE PELITIC GNEISSES OF FRASER LAKES ZONE B, WOLLASTON DOMAIN, NORTHERN SASKATCHEWAN, CANADA: MINERAL COMPOSITIONS, METAMORPHIC P-T-t PATH, AND IMPLICATIONS FOR THE GENESIS OF RADIOACTIVE ABYSSAL GRANITIC PEGMATITES. Can. Mineral. 50, 1669–1694. doi:10.3749/canmin.50.6.1669

Mercadier, J., 2009. Conditions de genèse des gisements d'uranium associés aux discordances protérozoïques et localisés dans les socles. exemple du socle du bassin d'Athabasca (Saskatchewan, Canada). INPL.

Mercadier, J., Cuney, M., Cathelineau, M., Lacorde, M., 2010a. U redox fronts and kaolinisation in basement-hosted unconformity-related U ores of the Athabasca Basin (Canada): late U remobilisation by meteoric fluids. Miner. Depos. 46, 105–135. doi:10.1007/s00126-010-0314-7

Mercadier, J., Richard, A., Boiron, M.-C.C., Cathelineau, M., Cuney, M., 2010b. Migration of brines in the basement rocks of the Athabasca Basin through microfracture networks (P-Patch U deposit, Canada). Lithos 115, 121–136. doi:10.1016/j.lithos.2009.11.010

1270 Mercadier, J., Richard, A., Cathelineau, M., 2012. Boron- and magnesium-rich marine brines
1271 at the origin of giant unconformity-related uranium deposits:δ11B evidence from Mg-
1272 tourmalines. Geology 40, 231–234. doi:10.1130/G32509.1
1273 Möller, P., Woith, H., Dulski, P., Lüders, V., Erzinger, J., Kämpf, H., Pekdeger, A., Hansen,
1274 B., Lodemann, M., Banks, D., 2005. Main and trace elements in KTB-VB fluid:
1275 Composition and hints to its origin. Geofluids 5, 28–41. doi:10.1111/j.1468-
1276 8123.2004.00104.x
1277 Muchez, P., Heijlen, W., Banks, D., Blundell, D., Boni, M., Grandia, F., 2005. 7: Extensional
1278 tectonics and the timing and formation of basin-hosted deposits in Europe. Ore Geol.
1279 Rev. 27, 241–267.
1280 Munz, I.A., Yardley, B.W.D., Banks, D.A., Wayne, D., 1995. Deep penetration of
1281 sedimentary fluids in basement rocks from southern Norway: Evidence from
1282 hydrocarbon and brine inclusions in quartz veins. Geochim. Cosmochim. Acta 59, 239–
1283 254.
1284 Ng, R., Alexandre, P., Kyser, K., 2013. Mineralogical and geochemical evolution of the
1285 unconformity-related McArthur river zone 4 orebody in the Athabasca Basin, Canada:
1286 Implications of a silicified zone. Econ. Geol. 108, 1657–1689.
1287 doi:10.2113/econgeo.108.7.1657
1288 Nutt, C.J., 1989. Chloritization and associated alteration at the Jabiluka unconformity-type
1289 uranium deposit, Northern Territory, Australia. Can. Mineral. 27 pt 1, 41–58.
1290 OECD/NEA-IAEA, 2016. Uranium 2016: Resources, Production and Demand, in: OECD
1291 (Ed.), Red Book. p. 550.
1292 Pacquet, A., Weber, F., 1993. Pétrographie et minéralogie des halos d'altération autour du
1293 gisement de Cigar Lake et leurs relations avec les minéralisations. Can. J. Earth Sci. 30,
1294 674–688.

1295 Pagel, M., 1975a. Détermination des conditions physico-chimiques de la silicification
1296 diagénétique des grès Athabasca (Canada) au moyen des inclusions fluides. Comptes
1297 Rendus Académie Sci. Paris, Série D. 280, 2301–2034.
1298 Pagel, M., 1975b. Cadre géologique des gisements d'uranium dans la structure de Carswell
1299 (Saskatchewan, Canada). Etudes des phases fluides. Thèse de 3ème cycle, Université de
1300 Nancy, Nancy, France.
1301 Pagel, M., Poty, B., Sheppard, M.F.S., 1980. Contribution to some Saskatchewan uranium
1302 deposits mainly from fluid inclusion and isotope data. In: Ferguson, J., Goleby, A.
1303 (Eds.), Uranium in the Pine Creek Geosyncline., International Atomic Energy Agency
1304 (IAEA).
1305 Pascal, M., Boiron, M.-C., Ansdell, K., Annesley, I.R., Kotzer, T., Jiricka, D., Cuney, M.,
1306 2016. Fluids preserved in variably altered graphitic pelitic schists in the Dufferin Lake
1307 Zone, south-central Athabasca Basin, Canada: implications for graphite loss and uranium
1308 deposition. Miner. Depos. 51, 619–636. doi:10.1007/s00126-015-0628-6
1309 Percival, J.B., Bell, K., Torrance, J.K., 1993. Clay mineralogy and isotope geochemistry of
1310 the alteration halo at the Cigar Lake uranium deposit. Can. J. Earth Sci. 30, 689–704.
1311 Percival, J.B., Kodama, H., 1989. SUDOITE FROM CIGAR LAKE, SASKATCHEWAN.
1312 Can. Mineral. 27, 633–641.
1313 Peters, K.E., Curry, D.J., Kacewicz, M., 2012. An overview of basin and petroleum system
1314 modeling: Definitions and concepts.
1315 Philippe, S., Lancelot, J.R., Clauer, N., Pacquet, A., 1993. Formation and evolution of the
1316 Cigar Lake uranium deposit based on. U- Pb and K- Ar isotope systematics. Can. J.
1317 Earth Sci. 30, 720–730.
1318 Polito, P.A., KYSER, T.K., Marlatt, J., Alexandre, P., Bajwah, Z., Drever, G., 2004.
1319 Significance of alteration assemblages for the origin and evolution of the Proterozoic

1320 Nabarlek unconformity-related uranium deposit, Northern Territory, Australia. Econ.
1321 Geol. 99, 113–139. doi:10.2113/gsecongeo.99.1.113
1322 Rabiei, M., Chi, G., Normand, C., Davis, W.J., Fayek, M., Blamey, N.J.F., 2017.
1323 Hydrothermal Rare Earth Element (Xenotime) Mineralization at Maw Zone, Athabasca
1324 Basin, Canada, and Its Relationship to Unconformity-Related Uranium Deposits. Econ.
1325 Geol. 112, 1483–1507. doi:10.5382/econgeo.2017.4518
1326 Rainbird, R.H., Stern, R. a., Rayner, N., Jefferson, C.W., 2007. Age, provenance, and regional
1327 correlation of the athabasca group, saskatchewan and alberta, constrained by igneous and
1328 detrital zircon geochronology. Bull. Geol. Surv. Canada 193–209.
1329 Ramaekers, P., Jefferson, C.W., Yeo, G.M., Collier, B., Long, D.G.F., Drever, G., McHardy,
1330 S., Jiricka, D., Cutts, C., Wheatley, K., Catuneanu, O., Bernier, S., Kupsch, B., Post,
1331 R.T., 2007. Revised geological map and stratigraphy of the Athabasca group,
1332 Saskatchewan and Alberta. Bull. Geol. Surv. Canada 155–191.
1333 Richard, A., 2017. Radiolytic (H2, O2) and other Trace Gases (CO2, CH4, C2H6, N2) in
1334 Fluid Inclusions from Unconformity-related U Deposits. Procedia Earth Planet. Sci. 17,
1335 273–276. doi:10.1016/j.proeps.2016.12.053
1336 Richard, A., Banks, D. a., Mercadier, J., Boiron, M.C., Cuney, M., Cathelineau, M., 2011. An
1337 evaporated seawater origin for the ore-forming brines in unconformity-related uranium
1338 deposits (Athabasca Basin, Canada): Cl/Br and δ37Cl analysis of fluid inclusions.
1339 Geochim. Cosmochim. Acta 75, 2792–2810. doi:10.1016/j.gca.2011.02.026
1340 Richard, A., Boulvais, P., Mercadier, J., Boiron, M.C., Cathelineau, M., Cuney, M., France-
1341 Lanord, C., 2013. From evaporated seawater to uranium-mineralizing brines: Isotopic
1342 and trace element study of quartz-dolomite veins in the athabasca system. Geochim.
1343 Cosmochim. Acta 113, 38–59. doi:10.1016/j.gca.2013.03.009
1344 Richard, A., Cathelineau, M., Boiron, M.-C., Mercadier, J., Banks, D. a., Cuney, M., 2016.

Metal-rich fluid inclusions provide new insights into unconformity-related U deposits (Athabasca Basin and Basement, Canada). Miner. Depos. 51, 249–270. doi:10.1007/s00126-015-0601-4

Richard, A., Kendrick, M.A., Cathelineau, M., 2014. Noble gases (Ar, Kr, Xe) and halogens (Cl, Br, I) in fluid inclusions from the Athabasca Basin (Canada): Implications for unconformity-related U deposits. Precambrian Res. 247, 110–125. doi:10.1016/j.precamres.2014.03.020

Richard, A., Pettke, T., Cathelineau, M., Boiron, M.C., Mercadier, J., Cuney, M., Derome, D., 2010. Brine-rock interaction in the Athabasca basement (McArthur River U deposit, Canada): Consequences for fluid chemistry and uranium uptake. Terra Nov. 22, 303–308. doi:10.1111/j.1365-3121.2010.00947.x

Sausse, J., Jacquot, E., Fritz, B., Leroy, J., Lespinasse, M., 2001. Evolution of crack permeability during fluid–rock interaction. Example of the Brézouard granite (Vosges, France). Tectonophysics 336, 199–214. doi:10.1016/S0040-1951(01)00102-0

Scheffer, C., Tarantola, A., Vanderhaeghe, O., Rigaudier, T., Photiades, A., 2017. CO2 flow during orogenic gravitational collapse: Syntectonic decarbonation and fluid mixing at the ductile-brittle transition (Lavrion, Greece). Chem. Geol. 450, 248–263. doi:10.1016/j.chemgeo.2016.12.005

SIBSON, R.H., 1977. Fault rocks and fault mechanisms. J. Geol. Soc. London. 133, 191–213. doi:10.1144/gsjgs.133.3.0191

Sibson, R.H., Moore, J.M.M., Rankin, a. H., 1975. Seismic pumping - a hydrothermal fluid transport mechanism. J. Geol. Soc. London. 131, 653–659. doi:10.1144/gsjgs.131.6.0653

Skirrow, R.G., Mercadier, J., Armstrong, R., Kuske, T., Deloule, E., 2016. The Ranger uranium deposit, northern Australia: Timing constraints, regional and ore-related alteration, and genetic implications for unconformity-related mineralisation. Ore Geol.

Rev. 76, 463–503. doi:10.1016/J.OREGEOREV.2015.09.001

Steele-MacInnis, M., Bodnar, R.J., Naden, J., 2011. Numerical model to determine the composition of H2O-NaCl-CaCl2 fluid inclusions based on microthermometric and microanalytical data. Geochim. Cosmochim. Acta 75, 21–40. doi:10.1016/j.gca.2010.10.002

Stober, I., Bucher, K., 2004. Fluid sinks within the earth's crust. Geofluids 4, 143–151. doi:10.1111/j.1468-8115.2004.00078.x

Thomas, D.J., Matthews, R.B., Sopuck, V.J., 1998. Athabasca Basin unconformity-type uranium deposits: a synopsis of the empirical model and review of exploration and production trends, in: Metallurgy and Petroleum Meeting, Montreal, May. pp. 3–7.

Walter, B.F., Burisch, M., Markl, G., 2016. Long-term chemical evolution and modification of continental basement brines - a field study from the Schwarzwald, SW Germany. Geofluids 16, 604–623. doi:10.1111/gfl.12167

Walter, B.F., Burisch, M., Marks, M.A.W., Markl, G., 2017. Major element compositions of fluid inclusions from hydrothermal vein-type deposits record eroded sedimentary units in the Schwarzwald district, SW Germany. Miner. Depos. 1–14.

Wilkinson, J.J., Eyre, S.L., Boyce, A.J., 2005. Ore-forming processes in Irish-type carbonate-hosted Zn-Pb deposits: Evidence from mineralogy, chemistry, and isotopic composition of sulfides at the Lisheen mine. Econ. Geol. 100, 63–86.

10.Appendix A

Based on the mapping of the distinct FIP types that cross-cut the primary quartz grains, a fracture paleoporosity of the quartz can be estimated through reconstruction of the microfracture network for each sample following the method proposed by Sausse et al. (2001), Lespinasse et al. (2005), and more recently Gomila et al., (2016) and Martz et al.,

(2017). It should be mentioned that this method was developed for paleoporosity and paleopermeability calculations based on the total microfracture networks, however, in this study the method is applied only to FIPs in quartz and therefore only allows the calculation of the maximum quartz paleoporosity. The quartz paleoporosity is only a semi-quantitative assessment of the fluid/rock ratio at the time of the distinct fluid migrations. The method is based on the characterization of the geometry of the microfracture network, with the assumption that each microfracture can be considered as a "penny-shaped cylinder". The quartz fracture porosity (φ_i) at a given time (t_i) of fluid (fi) migration is assumed to be entirely represented by the connected quartz fracture network (Cox, 2005) and is defined as :

$$\varphi_i = \sigma_{vi} \pi {c_{fi}}^2 e \qquad (1)$$

Where (e) is the cylinder height corresponding to the aperture of the microfracture and, here, approximated to 10 µm (mean size of the inclusions). However some statistical procedures are required to evaluate the fracture volumetric density (σ_{vi}) and the mean radius (c_{fi}), as the observed length (L_j) of each FIP in the polished wafer does not correspond to the real and maximum length value of the microfractures (i.e. the diameter of the disc) (Dehoff and Rhines, 1972).

Based on the assumption that a penny-shaped FIP population is randomly cut by the plane of observation and that the mean observed length will be less than their true length, the radius (c_{fi}) is defined as:

$$c_{fi} = \frac{\pi}{4 Z_{fi}} \qquad (2)$$

Where Z_{fi} is the mean value of the inverse ($1/L_{ji}$) of the measured FIP lengths of the fluid (fi) in the section plane:

$$Z_{fi} = \frac{1}{N} \sum_{j=1}^{N} \frac{1}{L_{ji}} \qquad (3)$$

The volumetric density (σ_{vi}) at the time t_i is hence defined as:

$$\sigma_{vi} = \frac{2\sigma_{si}Z_{fi}}{\pi \sin\theta i} \qquad (4)$$

Where the surface density (σ_{si}) is the cumulated measured lengths of all the FIPs (fi) per unit surface and (θ) is the dip of the microfractures.

Knowing the thickness of the oriented polished wafers, dip measurements of FIPs have been calculated for a few samples based on the perpendicular distance between the trace of a selected FIP on the lower surface of the polished wafer and the trace on the upper surface. Dip measurements range from 20 to 60° and a mean value of $\theta = 45°$ has been used.

11.Figure captions:

Figure 1: Simplified geological map of the Athabasca Basin and underlying basement rocks, Canada, modified from Jefferson et al. (2007). The location of the Cigar Lake deposit is indicated by the red square. Basement domains are identified by distinct colors. TD - Talston Domain, WMTZ - Wollaston-Mudjatik Transition Zone, WWD - Western Wollaston Domain, EWD - Eastern Wollaston Domain, VRSZ - Virgin River shear zone, BLSZ - Black Lake Shear Zone. The Snowbird Tectonic Zone (STZ) separates the Rae Subprovince in the west from the Hearne Subprovince in the east.

Figure 2: Simplified geological map of the basement at the unconformity around the Cigar Lake uranium deposit, coupled with the aeromagnetic map. Magnetic data have been acquired by AREVA Resources Canada. The Cigar Lake deposit is an elongated lens occurring immediately above a major EW graphite-rich shear zone forming a major electromagnetic (EM) conductor. Archean domes correspond to magnetic high values whereas the mainly Paleoproterozoic metapelitic gneiss environment correspond to magnetic low values.

Regional foliation is parallel to the elongated Archean domes whereas it is reoriented to the E-W direction around the shear zone hosting the deposit. Drill holes 466A and WC464 (in the bottom left insert) are exploration holes located about 8 km south of the deposit. The schematic cross-section (A – B) and interpretative cross-sections C – D and E – F, respectively through the EW shear zone and the NE-SW contact with the Archean Dome, are symbolized by a white line (see Fig. 4, 14 and 16).

Figure 3: A) Example of a FIP map of quartz from pegmatite sample WC450-429.7. FIPs are grouped into three types on the basis of the hosted fluid inclusions type (aqueous, carbonic, or mixed FIP). Orientations of FIPs are presented in rose diagrams with the orientation of the surrounding gneissic fabric together with the percentage number indicating the percentage value of the outer circle of the rose diagram. B) Example of a carbonic FIP. C) Example of a aqueous (brine) FIP. D) Mixed FIP showing both carbonic and brine inclusions interpreted as a reopening of carbonic FIP during later brine circulation. Abbreviations: Bt - biotite, Qtz - quartz.

Figure 4: Schematic cross-section through the main deposit. The U deposit is mainly associated with illite and sudoite alteration and is located at the unconformity immediately above a ductile-brittle graphitic shear zone referred as the Cigar Main E-W shear zone. Regional Athabasca sandstone is well-cemented and contains dickite as the main clay mineral infilling interstitial pore space. Two-phase aqueous inclusions are present at dustlines and in quartz overgrowths (Q1). Above the deposit, an illite halo extends upwards 400 m. Within this halo, the sandstone shows evidence of quartz dissolution and sometimes local recrystallization (Q2, not represented here as it is rare in this deposit), partial to total replacement of dickite by illite, and some euhedral quartz (Q3) crystallizing in fractures. The

later quartz generations show aqueous two and/or three-phase (with halite cube) inclusions. Below the deposit, an alteration halo, the depth extent of which is currently unknown, is characterized by partial quartz dissolution and replacement of plagioclas, K-feldspar, and retrograde (chloritic) biotite into an illite + sudoite assemblage. Both carbonic and two and/or three-phase aqueous inclusions are trapped as FIPs cross-cutting magmatic and metamorphic quartz. Abbreviations: Dick - dickite, ill - illite, Fld-K - K-feldspar, Bt - biotite, Qtz - quartz.

Figure 5: A) SEM image of a quartz-cemented sandstone showing aggregates of pseudomorphic dickite platelets, after vermicular kaolinite. Detrital quartz grains (Q0) have quartz overgrowths (Q1), both showing slight dissolution features. B) Image of early diagenetic authigenic quartz overgrowth separated from the detrital grain by a dustline of iron oxides. C) Image of a thick section of sandstone showing quartz dissolution affecting both detrital quartz and quartz overgrowth with a clay matrix of illite. D) SEM image of platy and hairy illite grains filling interstitial space; with corrosion pits on quartz overgrowth. E) SEM image of fine grains of hairy illite on the quartz overgrowth surface. F) SEM image of a partially dissolved quartz overgrowth with infilling assemblage of sudoite and illite. G) Photomicrograph of rare structurally-controlled pervasive silicification (Q2) in an illite-dominated faulted sandstone. H) Image of small euhedral quartz grains (Q3) separated from detrital quartz by a thin illite layer. The red rectangle corresponds to Fig. 6C.

Figure 6: A) Three-phase aqueous fluid inclusion (FI) in quartz overgrowth from sandstone (Q1) with heterogeneously trapped dickite. B) Isolated three-phase aqueous FI with a halite cube in quartz cement from structurally-controlled pervasive silicification in sandstone (Q2). C) Two-phase fluid inclusions trapped in euhedral quartz from a fracture in sandstone (see location in Fig. 5H.) with distinct Tm_{ice} indicating fluid mixing at the time of trapping. D)

Four-phase FI with daughter halite and chlorite (probably sudoite) in quartz overgrowth from sandstone. E) Two-phase brine FIs trapped as a FIP crosscutting magmatic quartz in pegmatite. F) Three-phase brine FIs with daughter halites trapped as a FIP crosscutting magmatic quartz in pegmatite. Abbreviations: Dick : dickite, ill : illite, Qtzm : magmatic quartz.

Figure 7: A) Th - Tm_{ice} pairs of analyzed FIs. Note that both FIs trapped in quartz overgrowth in dickite-dominated sandstones and FIs trapped as FIPs in barren structures and outside structures are restricted to a narrow area. In contrast, the other FIs (except Lw"), both in sandstone and basement, show a wide range of Tmice (equal to lower) and Th (equal to higher). B) Th(L+V→L) – TsNaCl pairs of Lwh and Lwh' FI. Lwh inclusions are tight to the 1:1 slope, whereas Lwh' inclusions mainly showed vapor disappearance before halite melting. Pressure correspondences at halite dissolution (so minimal pressure of trapping) are indicated and based on numerical modeling from Lecumberri-Sanchez et al. (2012). Two Th(L+V→L) – TsNaCl pairs from two FIPs with either heterogeneous or homogeneous trapping of halite mineral are shown and pictures of the fluid inclusion assemblage (FIA) are presented at the bottom of the Figure. FIs with heterogeneously-trapped halite show varying TsNaCl and constant Th(L+V→L), whereas homogeneously trapped FIs show constant Th(L+V→L) – TsNaCl pairs in the FIA.

Figure 8: Spatial distribution of FI types and microthermometric parameter ranges for analyzed FIs in FIPs in the basement. Relative proportion of FI types per drill hole are given in pie chart above the simplified geological map. Tm_{ice}, salinity, and Th ranges, mean, and median values per sample are given in box plot. FIs from the South conductor (Power Line), NE-SW conductor (Cigar North-East Trend), and off-conductor are Na-dominated with

relative slightly lower Th, and they represent the regional diagenetic fluid. In contrast, FIs from the Cigar Main E-W structure show a high proportion of Ca-dominated FIs with lower Tm_{ice}, higher salinity, and higher Th. The most extreme values have been obtained from samples below the deposit.

Figure 9: Spatial distribution of FI types and microthermometric parameter ranges for analyzed FIs in quartz overgrowths, cement, and euhedral quartz in the Athabasca Group. Relative proportion of FI types per drill hole are given in the pie chart above the simplified geological map. Tm_{ice}, salinity, and Th ranges, mean, and median values per sample are given in a box plot. Percentages of relative clay proportion per sample obtained from SWIR field spectrometry are provided and are indicated by the colored bar chart. Samples located above the Power Line and the NE-SW conductor (Cigar North-East Trend) are dominated by dickite, contain Na-dominated FIs with relatively slightly lower Th, and define the regional diagenetic fluid (except for sample WC473-385.4 located right at the unconformity and containing illite + sudoite with Ca-dominated inclusions). In contrast, FIs located on the Cigar Main E-W structure contain significant proportions of illite and sudoite with high proportions of Ca-dominated FIs with lower Tm_{ice}, higher salinity, and higher Th.

Figure 10: Spatial distribution of maximum amounts of detected gases in brine FIs per basement sample. H_2 and O_2 occurrence is restricted to the mineralized area. When gases were detected, the FIs are dominated by CO_2-CH_4-N_2

Figure 11: Major monovalent cationic vs. divalent cationic composition of individual brine FIs from both sandstone and basement samples. The arrows indicate the evolution from a

1543 NaCl-rich brine composition toward a $CaCl_{2-}$ and $MgCl_2$-dominated composition associated
1544 with a gain in chlorinity (horizontal dashed arrows).
1545
1546 Figure 12: La-ICP-MS geochemical data of fluids from individual brine FIs from both
1547 sandstone and basement samples. Selected element concentrations are plotted against the
1548 calcium content. The FIs occurring in the NE-SW barren conductor (Cigar North-East Trend)
1549 are dominated by the NaCl-rich end-member, whereas the FIs occurring below and above the
1550 deposit are dominated by the $CaCl_2$-rich end-member
1551
1552 Figure 13: Proportion of elemental gains and loss through the evolution from the NaCl-rich
1553 brine end-member toward the high salinity $CaCl_2$-rich brine. 15 Selected $CaCl_2$-rich Lwh'
1554 inclusions from sample U427-200 to represent the most evolved $CaCl_2$-rich end member
1555 whereas a mean composition based on the Lw1 and Lw2 inclusions trapped in sample
1556 WC473-452.6 has been used to define the NaCl-rich end-member.
1557
1558 Figure 14: Geological map of the basement at the unconformity near the Cigar Lake deposit
1559 with rose diagrams showing the preferred orientation of both carbonic and brine fluid
1560 inclusion planes (FIP) per drill holes. Main orientations of the two FIP types are indicated in
1561 rose diagrams with the foliation of the gneissic surrounding rocks. The percentage number
1562 indicates the value of the outer circle. Both carbonic and brine FIPs show similar orientations
1563 at the scale of drilling.
1564
1565 Figure 15: Evolution of FIP density and calculated quartz fracture paleoporosity based on
1566 both carbonic and brine FIP networks from cross-sections C – D and E – F (Fig. 2.). Mixed
1567 FIPs density and calculated quartz paleoporosity based on mixed FIPs have been added to

both carbonic and brine FIPs as they contributed to the overall paleoporosity network, both at the times of carbonic and brine migrations. Pegmatite samples are labelled from 01 to 21, correspondences are given in Table 1.

Figure 16: Estimated P-T evolution of basinal brine in and above the E-W structure controlling the Cigar Lake deposit. Two scenarios are proposed. A) Brine evolution and mixing under hydrostatic regime from regional Na-dominated brine toward evolved Ca-dominated brines during isobaric heating induced by thermal convection. B) Episodic brine evolution and mixing between Na- and Ca-dominated brines during isothermal pressure drop by pressure regime change from lithostatic to hydrostatic, induced by seismic pumping.

Figure 17: Schematic 3D block diagram of the brine circulations and physicochemical changes induced by brine-basement rock interactions in the 10 km² area surrounding the Cigar Lake deposit; at the time of deposit formation. Two interpretative cross-sections have been added: i) the first (on the right) is in a priori barren basement graphitic structure and show features of regional background: diagenetic dickite-dominant clay matrix in the sandstone and ubiquitous presence of Na-dominated brine that slightly and pervasively percolate a in a low permeability basement. ii) The second (on the left) is located through the Cigar Main E-W ductile brittle structure. This structure was reactivated at the time of U deposition due to weakening during earlier Hudsonian basement uplift. The regional Na-dominated brines evolved into a Cl, Mg, K, Mn, Ba, Sr, Pb, U-enriched and Li depleted Ca-dominated brine through brine-basement interactions resulting from a higher fluid-rock ratio in the damage zone of this structure. The Ca-dominated basinal brines mixed with regional Na-dominated brines in and above the structure due to thermo- and/or deformation-driven convection either in the fault plane or perpendicular to it. Brine convection induced intense hydrothermal illite

± sudoite alteration replacing the early diagenetic dickite and was a critical process for the formation of the U deposit.

Table 1: Fluid inclusion nomenclature. The nomenclature is based on microthermometric observations and Tm_{ice} ranges. The considered system and the methodology used for the calculations of bulk compositions per inclusion types are indicated. HH - hydrohalite.

Table 2: Proportion of analyzed FIs with element concentrations above the L.O.D.

Table 3: Geometrical parameters of the FIP networks for the carbonic, brine, and mixed FIPs. σS - FIP density, Zf - mean value of the inverse of the measured FIP lengths, Cf - mean radius. Calculated maximum paleoporosity of quartz at the time of carbonic or brine fluid migration is indicated in %. As Quartz paleoporosity calculated from mixed FIPs is effective both during carbonic fluid and brine circulation, it is added to quartz paleoporosity based only on carbonic or brine FIPs. Correspondences between the samples names (I.D.) and the labels used in Fig. 14 are also given here.

Appendix A: Methodology for the reconstruction of the microfracture network and calculation of the quartz fracture paleoporosity.

ESM-1: SWIR spectroscopy and microthermometry parameters of analyzed fluid inclusions. Calculated bulk salinity from microthermometric data is given in Cl (mol/kg). Abbreviations: Fe-chl - ferromagnesian retrograde chlorite; I - illite; Sud - Sudoite; K - kaolin minerals; Ps. p.- pseudosecondary plane. La-ICP-MS data are given after.

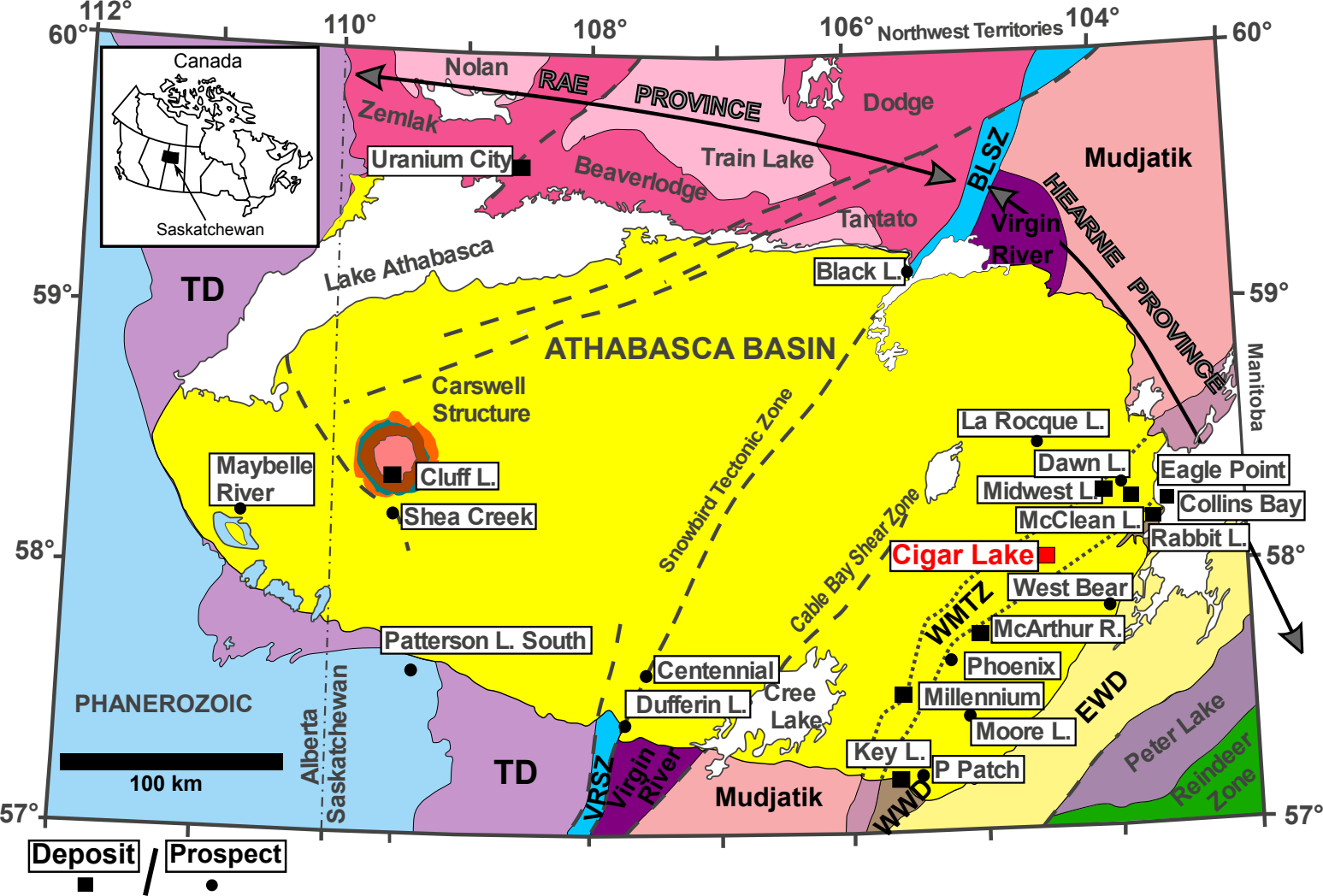
112°
110°
108°
106°
104°
60°
59°
58°
57°
Northwest Territories
Manitoba
Canada
Saskatchewan
Nolan
RAE PROVINCE
Zemlak
Dodge
Uranium City
Beaverlodge
Train Lake
Tantato
BLSZ
Mudjatik
HEARNE PROVINCE
Virgin River
Black L.
Lake Athabasca
TD
ATHABASCA BASIN
Carswell Structure
Maybelle River
Cluff L.
Shea Creek
Snowbird Tectonic Zone
Cable Bay Shear Zone
La Rocque L.
Dawn L.
Eagle Point
Midwest L.
Collins Bay
McClean L.
Rabbit L.
Cigar Lake
West Bear
WMTZ
McArthur R.
Phoenix
Millennium
Moore L.
EWD
Key L.
P Patch
WWD
Peter Lake
Reindeer Zone
Patterson L. South
Centennial
Dufferin L.
Cree Lake
PHANEROZOIC
Alberta
Saskatchewan
100 km
TD
VRSZ
Virgin River
Mudjatik
Deposit
Prospect

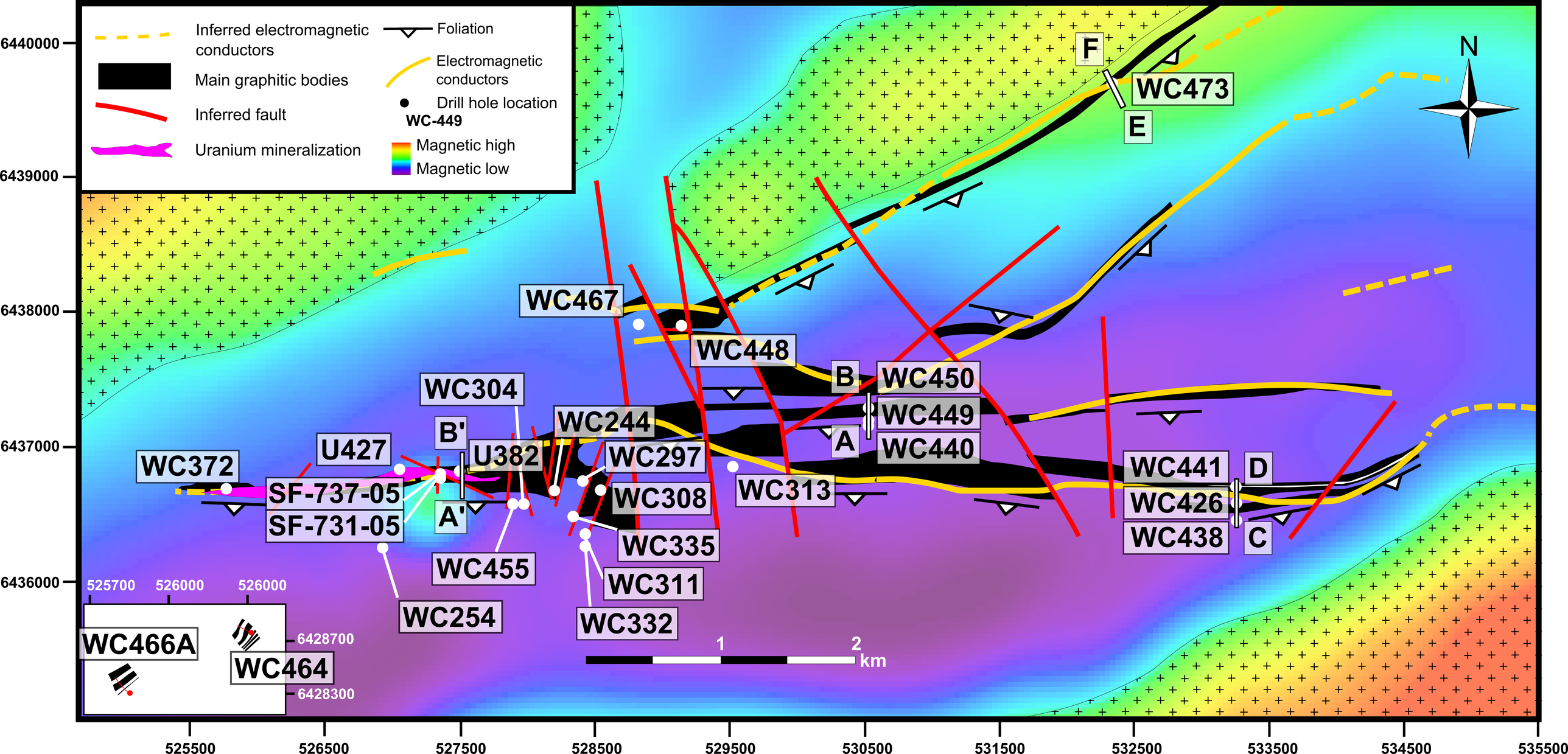
Inferred electromagnetic conductors
Main graphitic bodies
Inferred fault
Uranium mineralization
Foliation
Electromagnetic conductors
Drill hole location
WC-449
Magnetic high
Magnetic low
N
F
WC473
E
WC467
WC448
B
WC450
WC449
A
WC440
WC304
B'
WC244
U427
U382
WC297
WC372
SF-737-05
SF-731-05
A'
WC308
WC313
WC441
D
WC426
WC438
C
WC335
WC455
WC311
WC254
WC332
1
2
km
WC466A
WC464
525700
526000
526000
6428700
6428300
6440000
6439000
6438000
6437000
6436000
525500
526500
527500
528500
529500
530500
531500
532500
533500
534500
535500

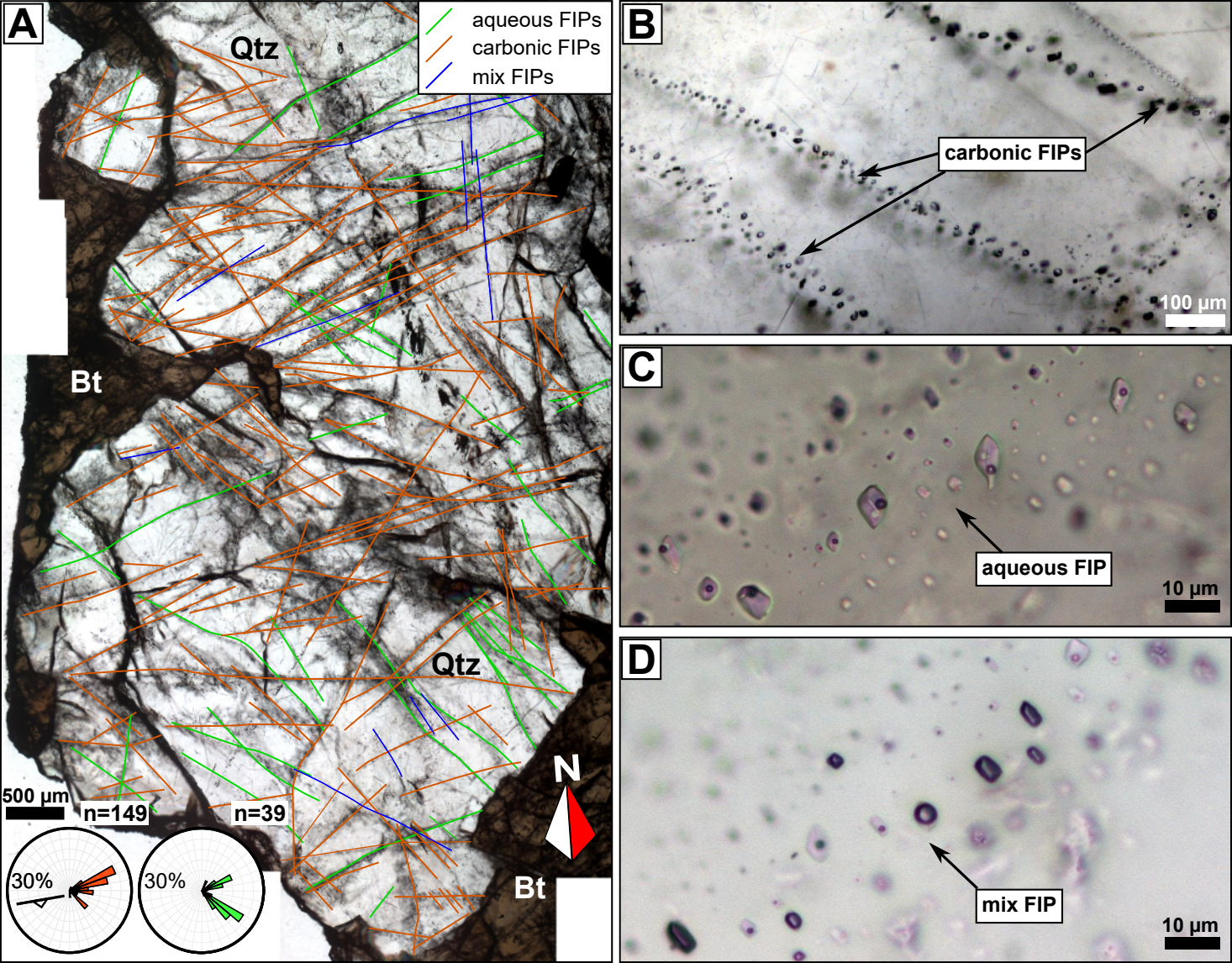
A
aqueous FIPs
carbonic FIPs
mix FIPs
Qtz
Bt
Qtz
Bt
N
500 µm
n=149
n=39
30%
30%
B
carbonic FIPs
100 µm
C
aqueous FIP
10 µm
D
mix FIP
10 µm

dustline

Q0

Q1

dick

Q0

Q1

Q1

dick

Q0

Q0

perched bodies

Q3

Q3

Q3

Q3

Q0

Q1

ill

Q0

Q1

Q1

Q0

Q1

Q0

ill

illite dominated area

Dickite dominated area

A'

B'

Siderite-hematite cap

major U body - sudoite + illite

Unconformity

illite + sudoite alteration

50 m

Fld-K +
ill + sud

Qtz

Bt

Qtz

Fld-K +
ill + sud

Metapelitic gneiss

Augen gneiss

Calcsilicate rocks

Granitic pegmatite and anatectic material

Conglomerate

2-5 % graphite

>5 % graphite

Graphitic cataclasite and breccia >20% graphite

Illite alteration

Siderite-Hematite cap

U mineralization

Basement argilitization

Faults

Fluid inclusions

Basinal brine

Carbonic fluid

A

Q_0

Q_1

Q_1

Dick

Q_0

Q_0

Q_0

WC473-205 X 150 15.0kV COMPO LM 100µm WD 17.3mm

B

Q_1

dustline

Hem.

Q_0

100 µm

WC464-165

C

Q_0

Q_0

Q_1

Q_1

Q_0

Qtz dissolution

ill

Qtz dissolution

WC372-431

D

dissolution pits

Q_1

ill

ill

WC372-431

15.0kV 11.1mm x350 YAGBSE 50.0um

E

Q_1

5µm

ill

Q_1

ill

Q_1

WC455-456

15,0kV 9,8mm x400 YAGBSE 100um

F

Q_1

Qtz dissolution

sud + ill

Q_1

WC449-358.4

15.0kV 10.4mm x1.30k SE(M) 40.0um

G

ill

Silicification (Q_1+Q_2)

ill

2 cm

WC311-342.6

H

Q_3

Q_0

Q_0

ill

100 µm

WC467-325.9

2cm

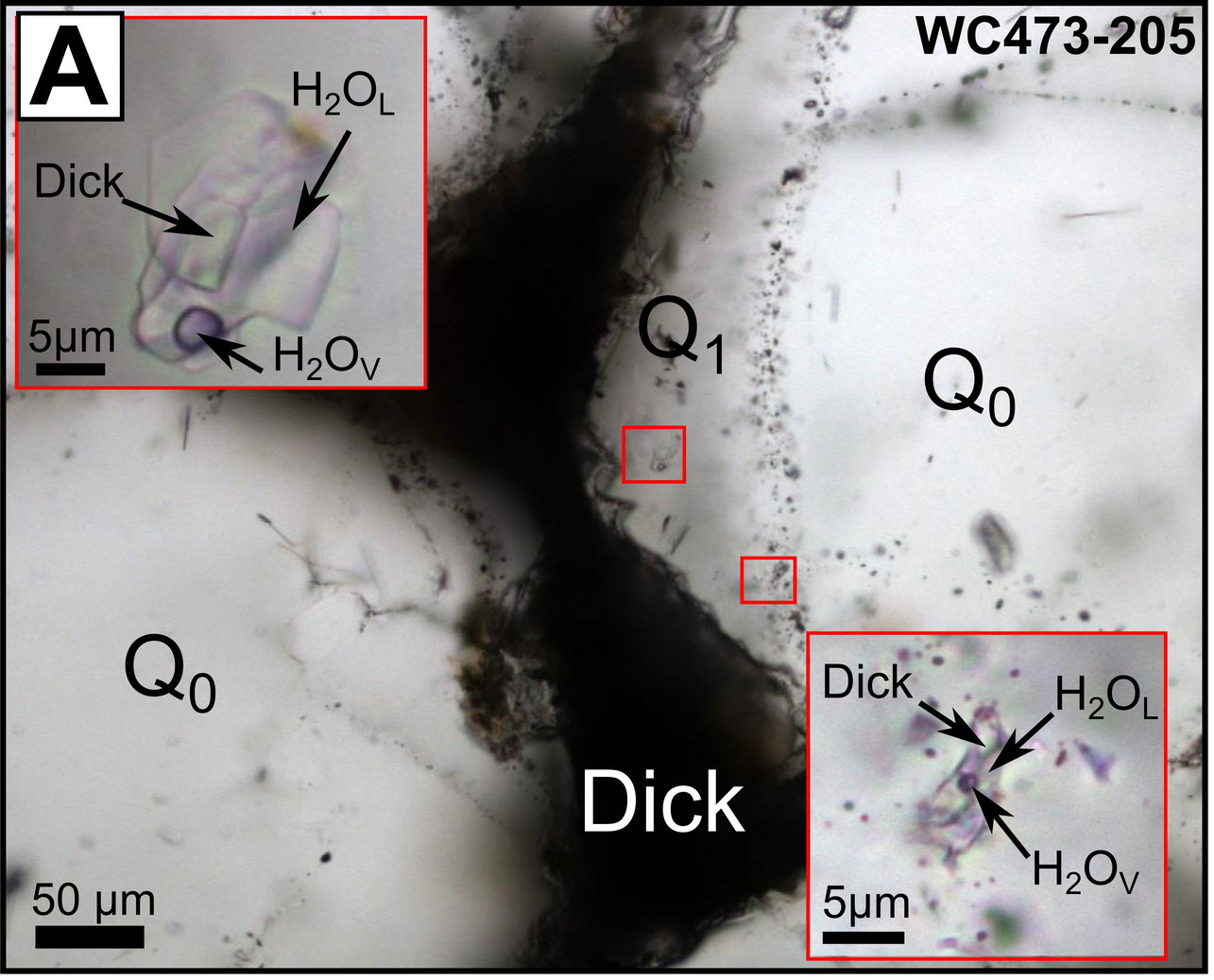
A
WC473-205
H_2O_L
Dick
5µm
H_2O_V
Q_1
Q_0
Q_0
Dick
50 µm
Dick
H_2O_L
H_2O_V
5µm

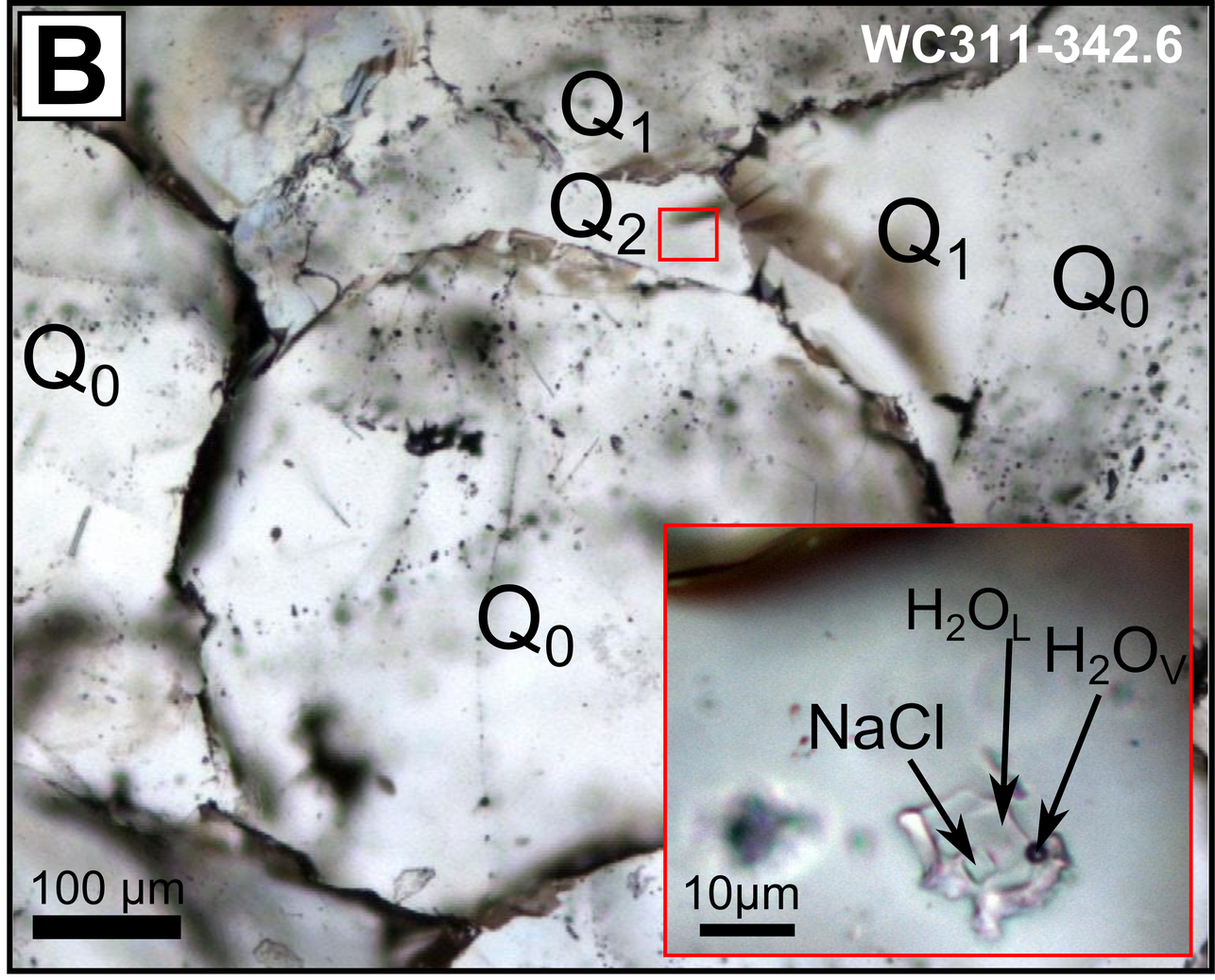
B
WC311-342.6
Q_1
Q_2
Q_1
Q_0
Q_0
Q_0
100 µm
H_2O_L
H_2O_V
NaCl
10µm

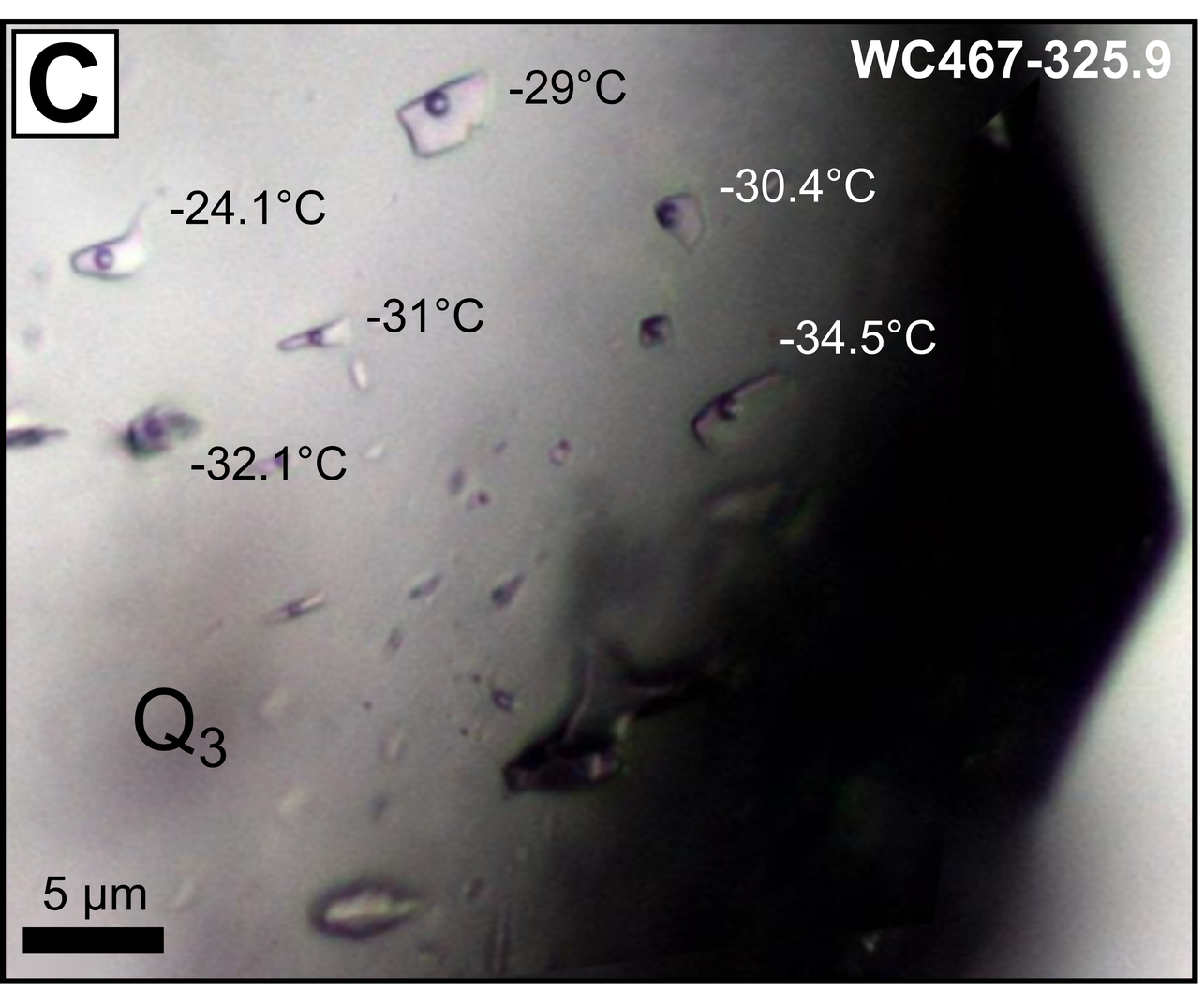
C
WC467-325.9
-29°C
-30.4°C
-24.1°C
-31°C
-34.5°C
-32.1°C
Q_3
5 µm

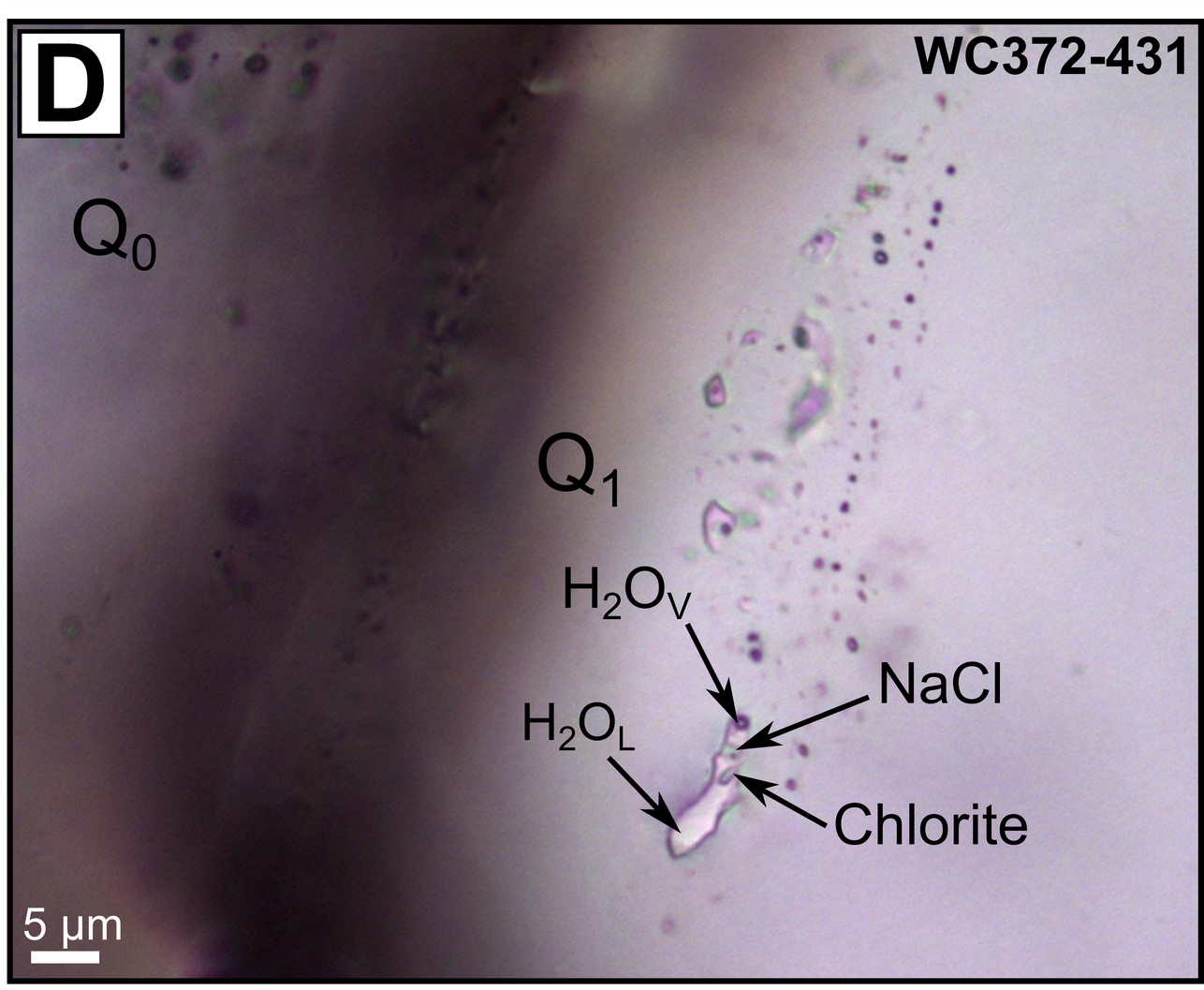
D
WC372-431
Q_0
Q_1
H_2O_V
NaCl
H_2O_L
Chlorite
5 µm

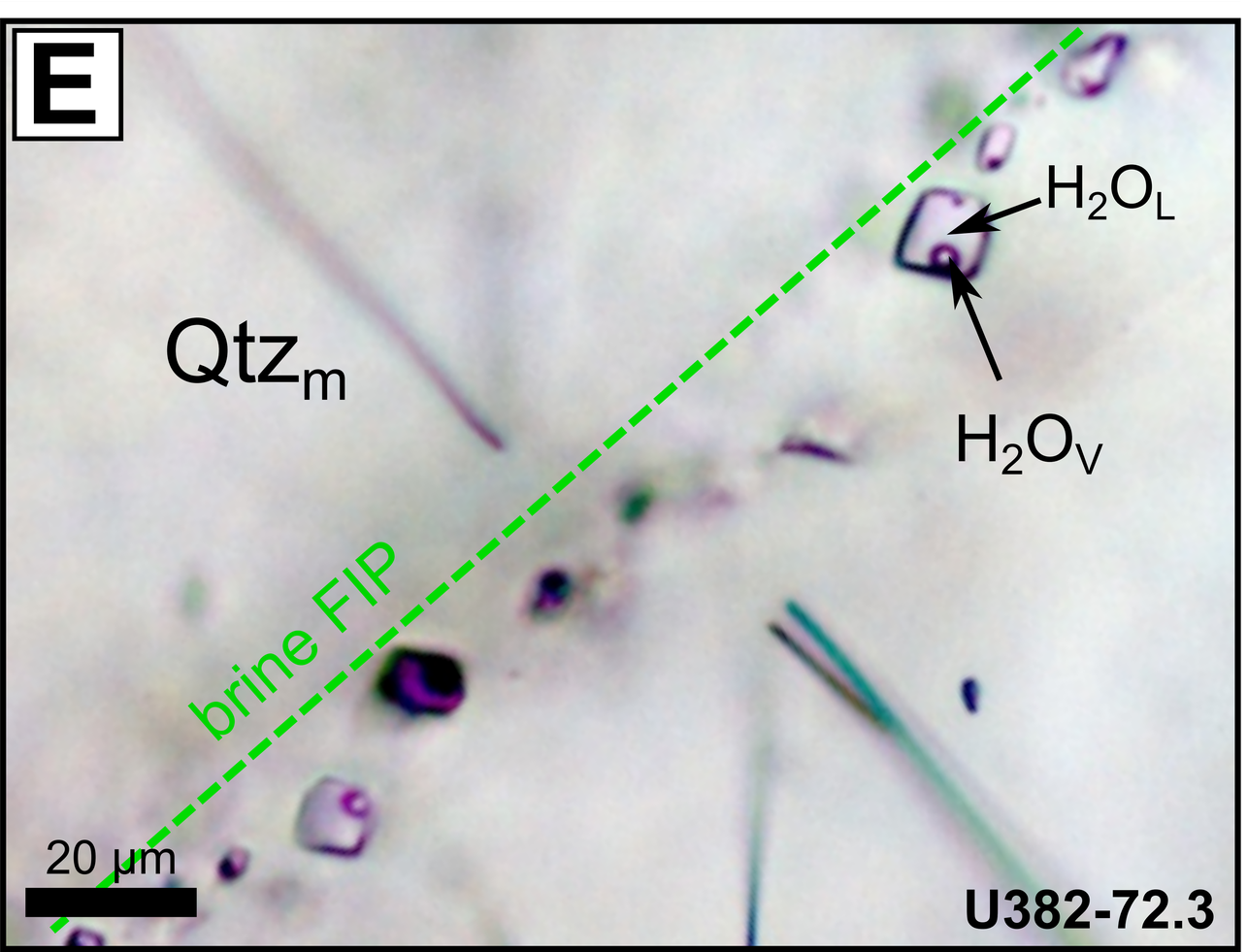
E
H_2O_L
Qtz_m
H_2O_V
brine FIP
20 µm
U382-72.3

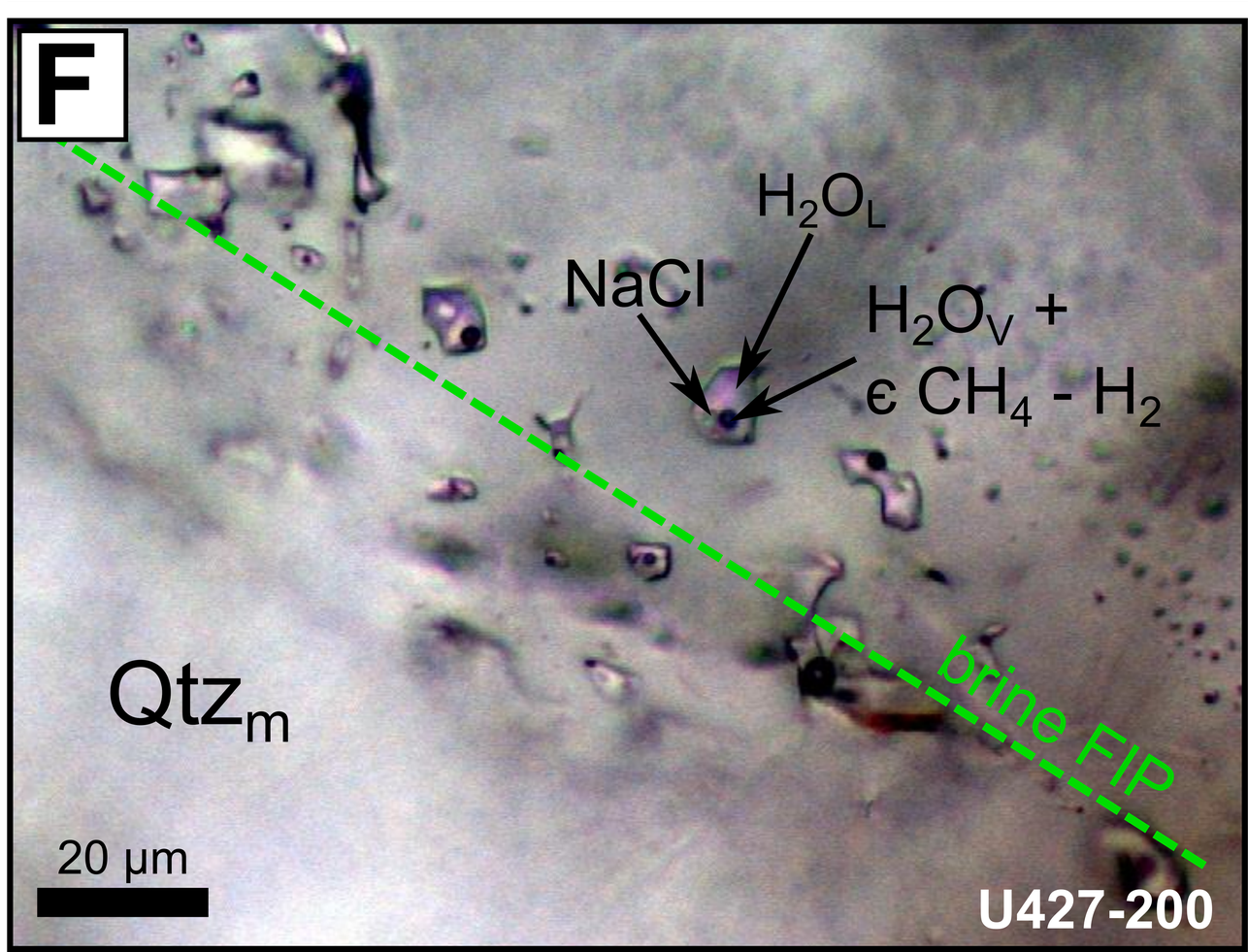
F
H_2O_L
NaCl
H_2O_V +
ϵ CH_4 - H_2
Qtz_m
brine FIP
20 µm
U427-200

FI in basin

- dickite dominated
- illite + dickite dominated
- illite + sudoite dominated
- illite dominated

FI in basement

A

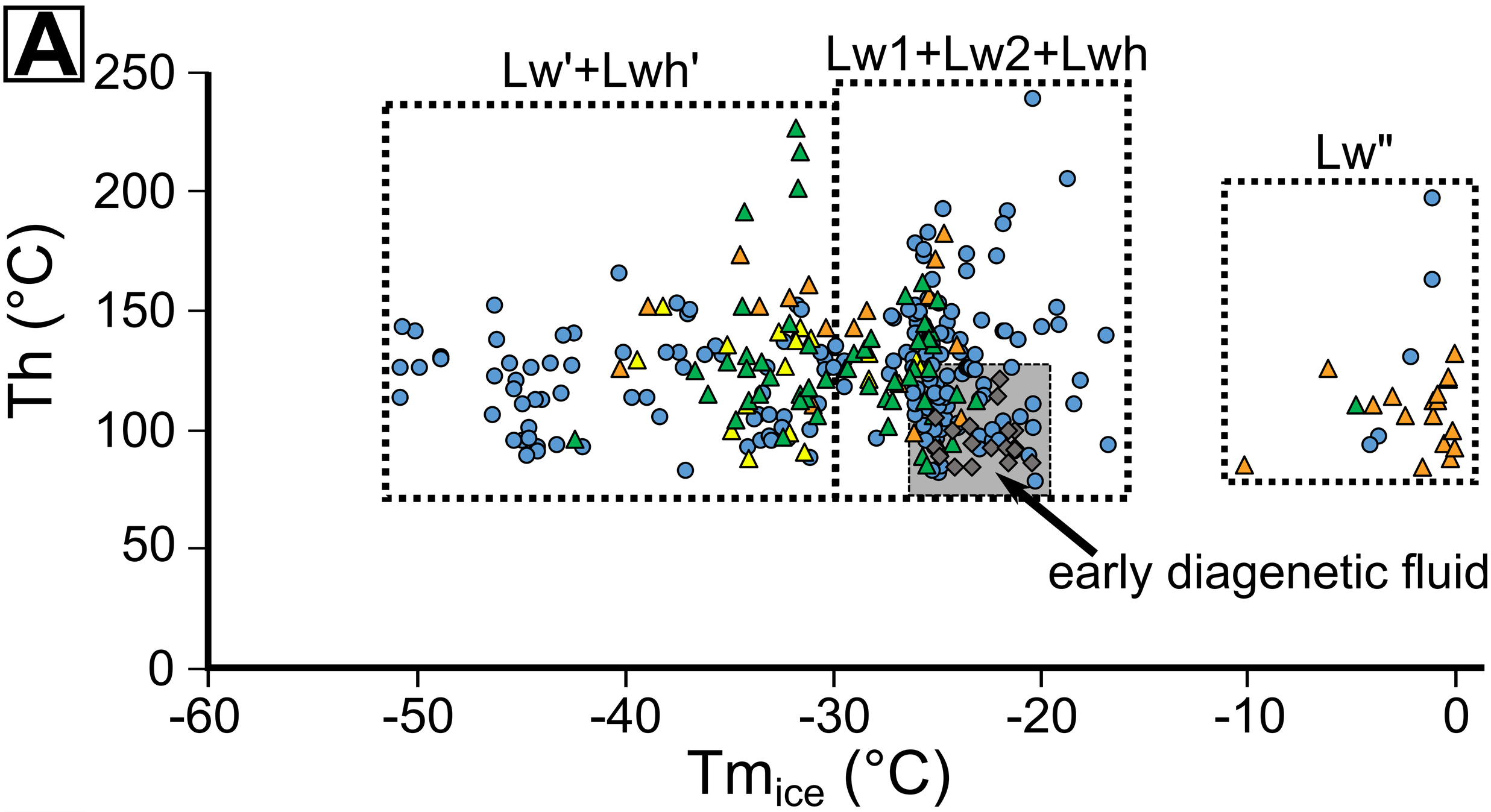

B

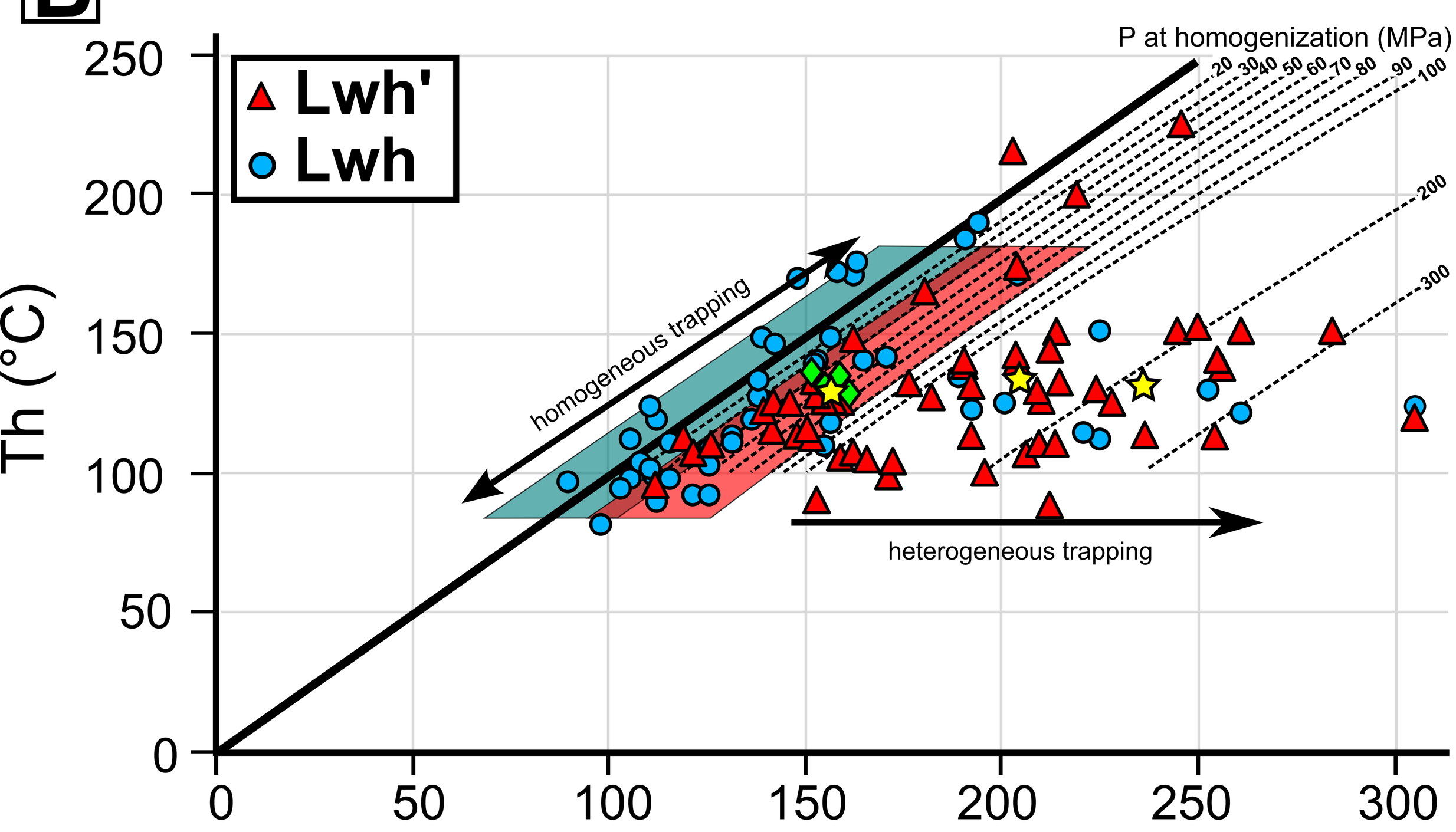

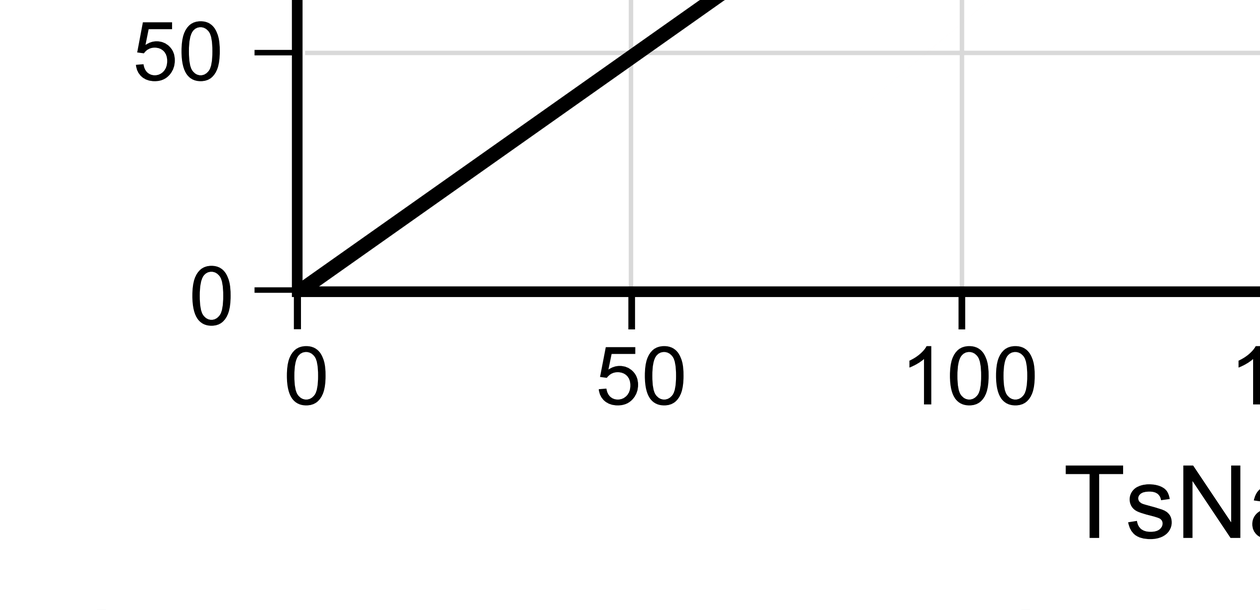

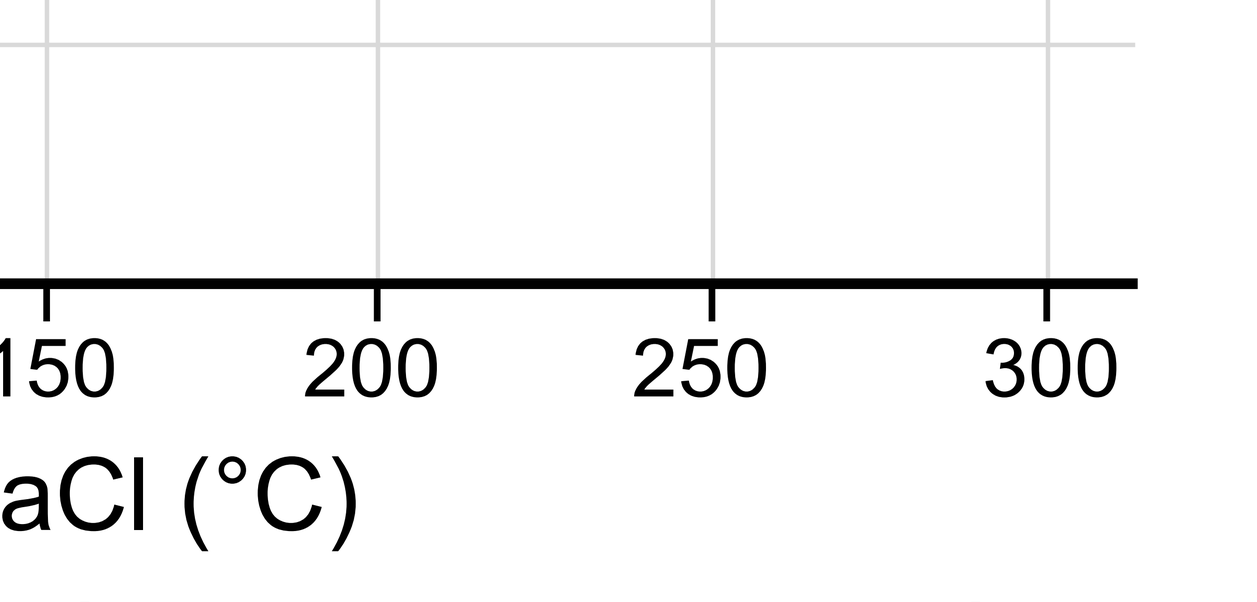

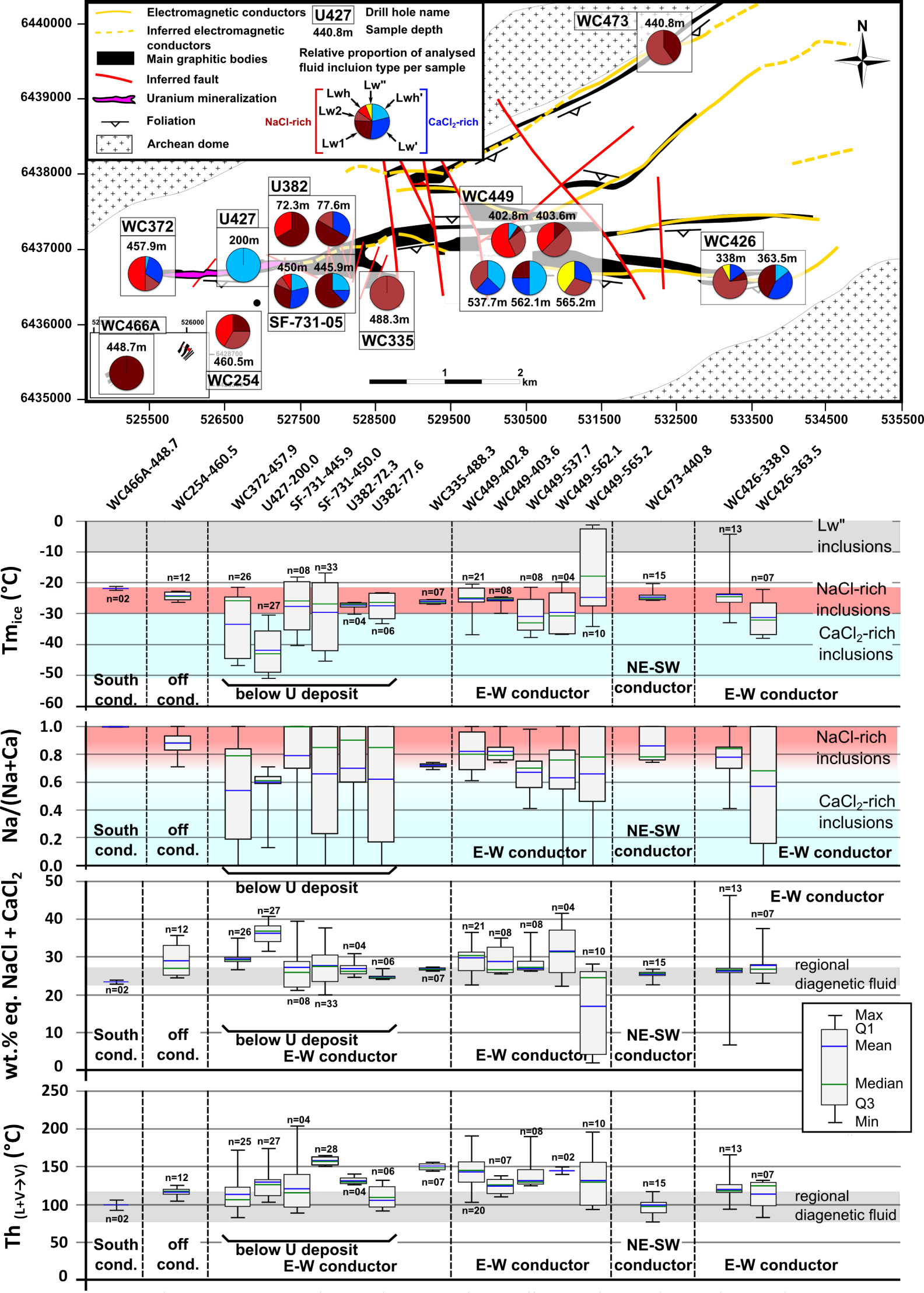
Electromagnetic conductors
Inferred electromagnetic conductors
Main graphitic bodies
Inferred fault
Uranium mineralization
Foliation
Archean dome
U427
440.8m
Drill hole name
Sample depth
Relative proportion of analysed fluid incluion type per sample
Lwh
Lw"
Lwh'
Lw2
Lw1
Lw'
NaCl-rich
CaCl2-rich
WC473
440.8m
N
U382
72.3m
77.6m
WC449
402.8m
403.6m
WC372
457.9m
U427
200m
WC426
338m
363.5m
450m
445.9m
537.7m
562.1m
565.2m
SF-731-05
488.3m
WC335
WC466A
448.7m
460.5m
WC254
1
2
km
6440000
6439000
6438000
6437000
6436000
6435000
525500
526500
527500
528500
529500
530500
531500
532500
533500
534500
535500
WC466A-448.7
WC254-460.5
WC372-457.9
U427-200.0
SF-731-445.9
SF-731-450.0
U382-72.3
U382-77.6
WC335-488.3
WC449-402.8
WC449-403.6
WC449-537.7
WC449-562.1
WC449-565.2
WC473-440.8
WC426-338.0
WC426-363.5
Tmice (°C)
Lw" inclusions
NaCl-rich inclusions
CaCl2-rich inclusions
South cond.
off cond.
below U deposit
E-W conductor
NE-SW conductor
Na/(Na+Ca)
wt.% eq. NaCl + CaCl2
regional diagenetic fluid
Max
Q1
Mean
Median
Q3
Min
Th (L+V→V) (°C)

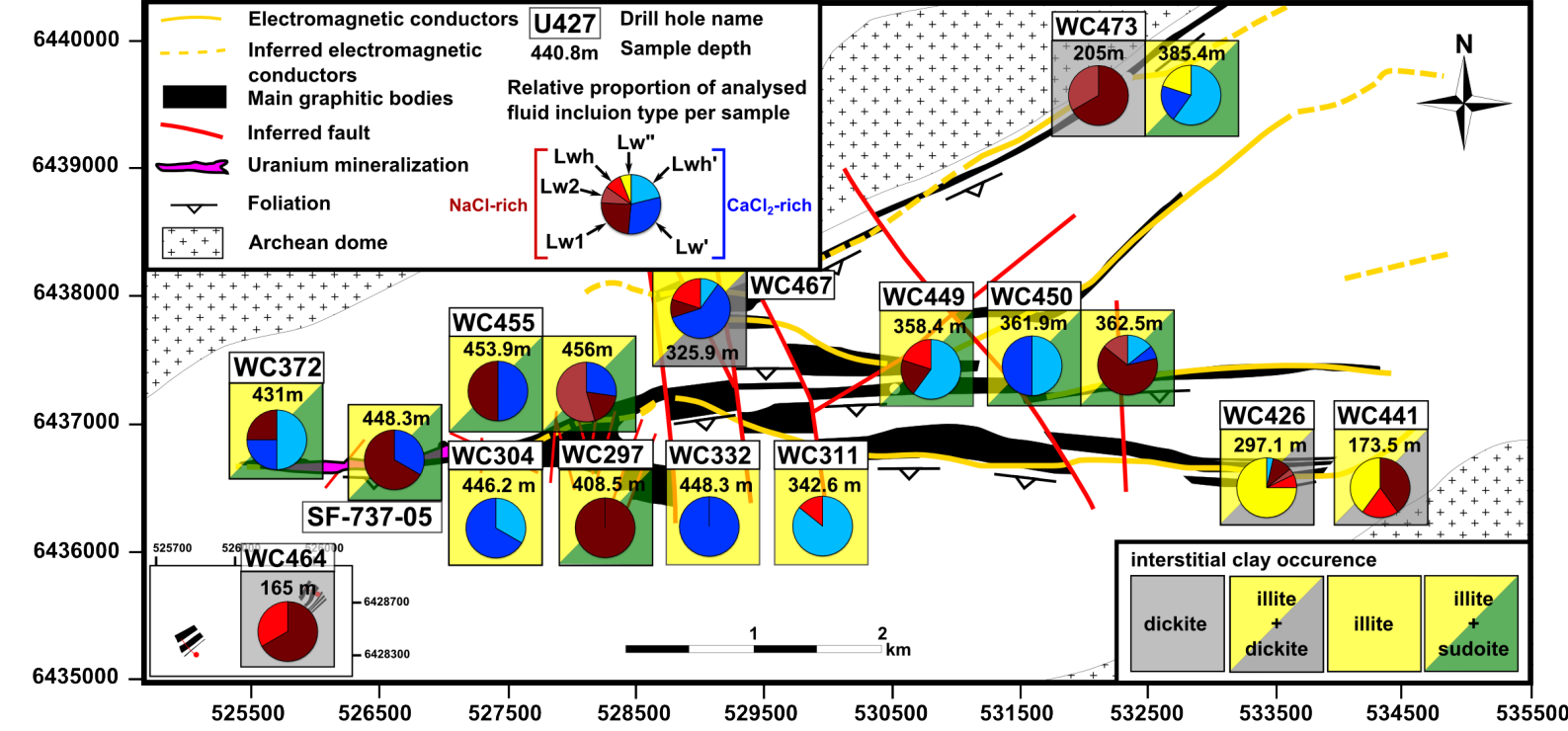
Electromagnetic conductors
Inferred electromagnetic conductors
Main graphitic bodies
Inferred fault
Uranium mineralization
Foliation
Archean dome
U427
440.8m
Drill hole name
Sample depth
Relative proportion of analysed fluid incluion type per sample
NaCl-rich
CaCl2-rich
Lwh
Lw"
Lwh'
Lw2
Lw1
Lw'
N
WC473
205m
385.4m
WC467
325.9 m
WC449
358.4 m
WC450
361.9m
362.5m
WC455
453.9m
456m
WC372
431m
448.3m
WC304
446.2 m
WC297
408.5 m
WC332
448.3 m
WC311
342.6 m
SF-737-05
WC426
297.1 m
WC441
173.5 m
WC464
165 m
interstitial clay occurence
dickite
illite + dickite
illite
illite + sudoite
1
2
km
6440000
6439000
6438000
6437000
6436000
6435000
525500
526500
527500
528500
529500
530500
531500
532500
533500
534500
535500

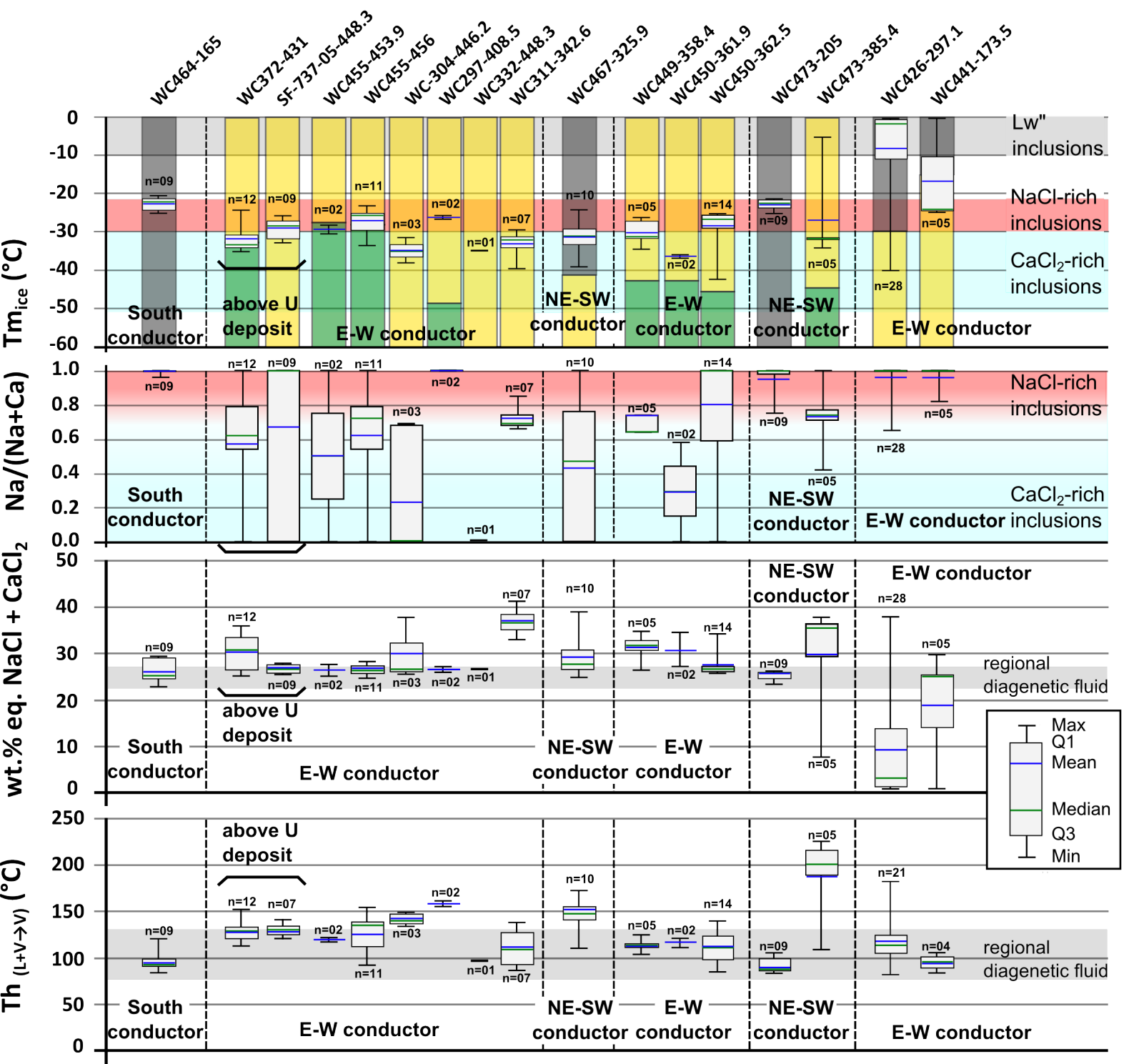
WC464-165
WC372-431
SF-737-05-448.3
WC455-453.9
WC455-456
WC-304-446.2
WC297-408.5
WC332-448.3
WC311-342.6
WC467-325.9
WC449-358.4
WC450-361.9
WC450-362.5
WC473-205
WC473-385.4
WC426-297.1
WC441-173.5
Tmice (°C)
Lw" inclusions
NaCl-rich inclusions
CaCl2-rich inclusions
Na/(Na+Ca)
wt.% eq. NaCl + CaCl2
regional diagenetic fluid
Th (L+V→V) (°C)
South conductor
above U deposit
E-W conductor
NE-SW conductor
Max
Q1
Mean
Median
Q3
Min

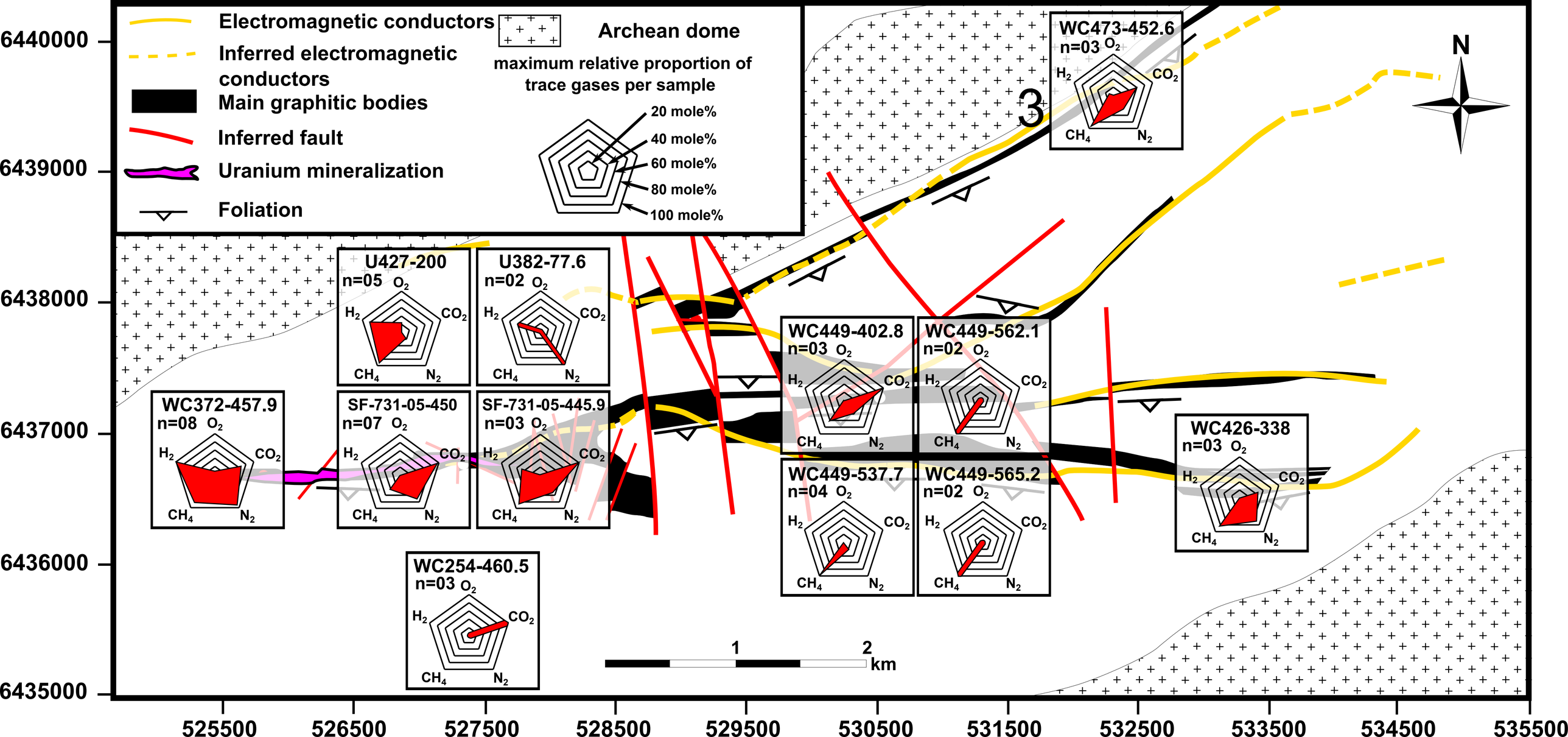
Electromagnetic conductors
Inferred electromagnetic conductors
Main graphitic bodies
Inferred fault
Uranium mineralization
Foliation
Archean dome
maximum relative proportion of trace gases per sample
20 mole%
40 mole%
60 mole%
80 mole%
100 mole%
WC473-452.6
n=03
U427-200
n=05
U382-77.6
n=02
WC449-402.8
n=03
WC449-562.1
n=02
WC372-457.9
n=08
SF-731-05-450
n=07
SF-731-05-445.9
n=03
WC449-537.7
n=04
WC449-565.2
n=02
WC426-338
n=03
WC254-460.5
n=03
O2
H2
CO2
CH4
N2
3
N
1
2
km
6440000
6439000
6438000
6437000
6436000
6435000
525500
526500
527500
528500
529500
530500
531500
532500
533500
534500
535500

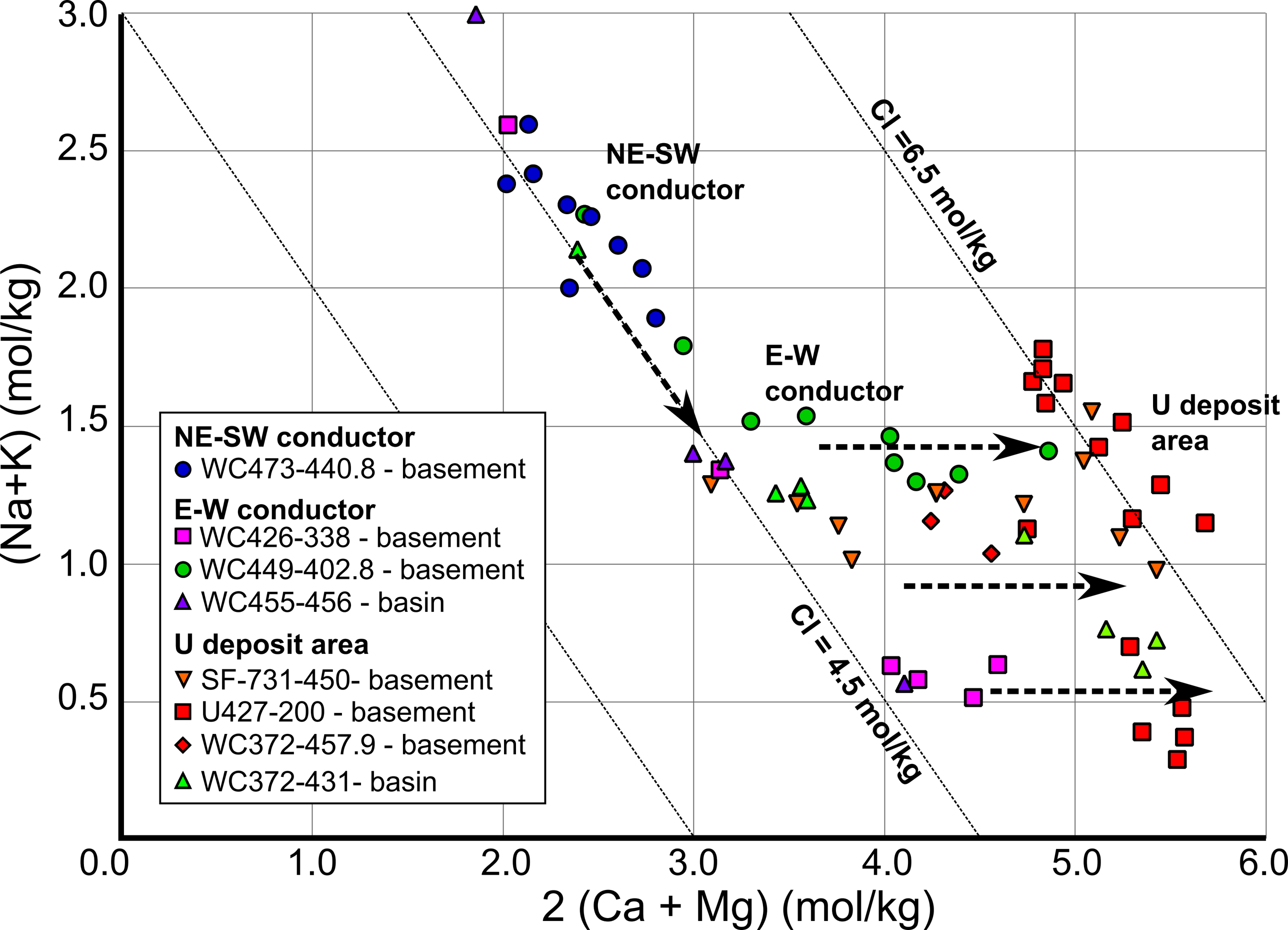
NE-SW conductor
E-W conductor
U deposit area
Cl =6.5 mol/kg
Cl = 4.5 mol/kg
NE-SW conductor
WC473-440.8 - basement
E-W conductor
WC426-338 - basement
WC449-402.8 - basement
WC455-456 - basin
U deposit area
SF-731-450- basement
U427-200 - basement
WC372-457.9 - basement
WC372-431- basin
(Na+K) (mol/kg)
2 (Ca + Mg) (mol/kg)
3.0
2.5
2.0
1.5
1.0
0.5
0.0
1.0
2.0
3.0
4.0
5.0
6.0

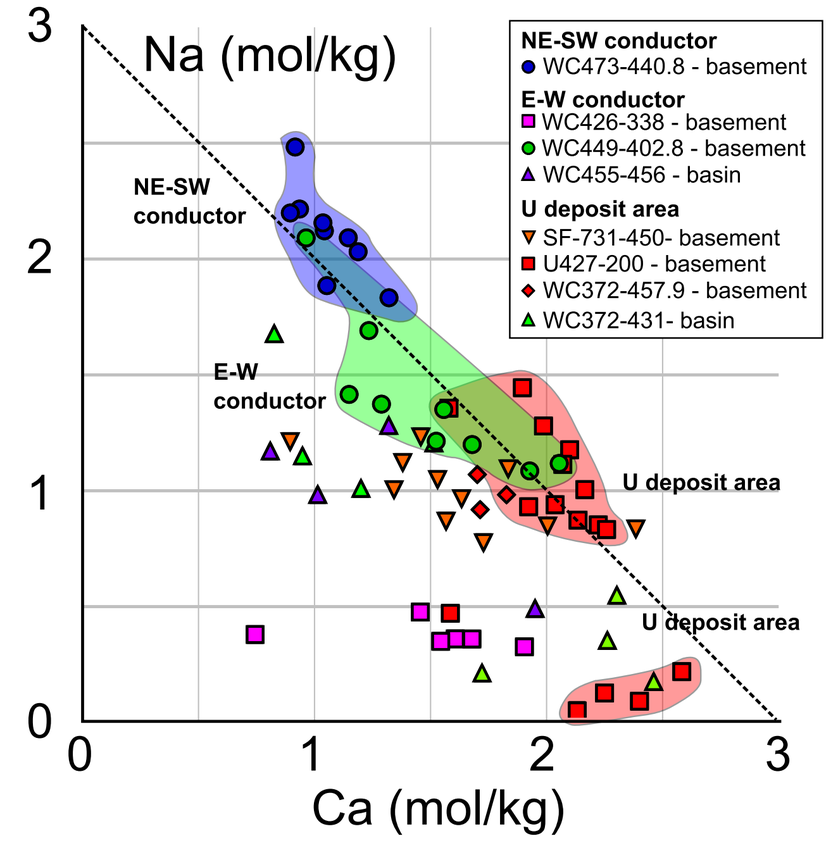
Na (mol/kg)
Ca (mol/kg)
NE-SW conductor
WC473-440.8 - basement
E-W conductor
WC426-338 - basement
WC449-402.8 - basement
WC455-456 - basin
U deposit area
SF-731-450- basement
U427-200 - basement
WC372-457.9 - basement
WC372-431- basin
NE-SW conductor
E-W conductor
U deposit area
U deposit area

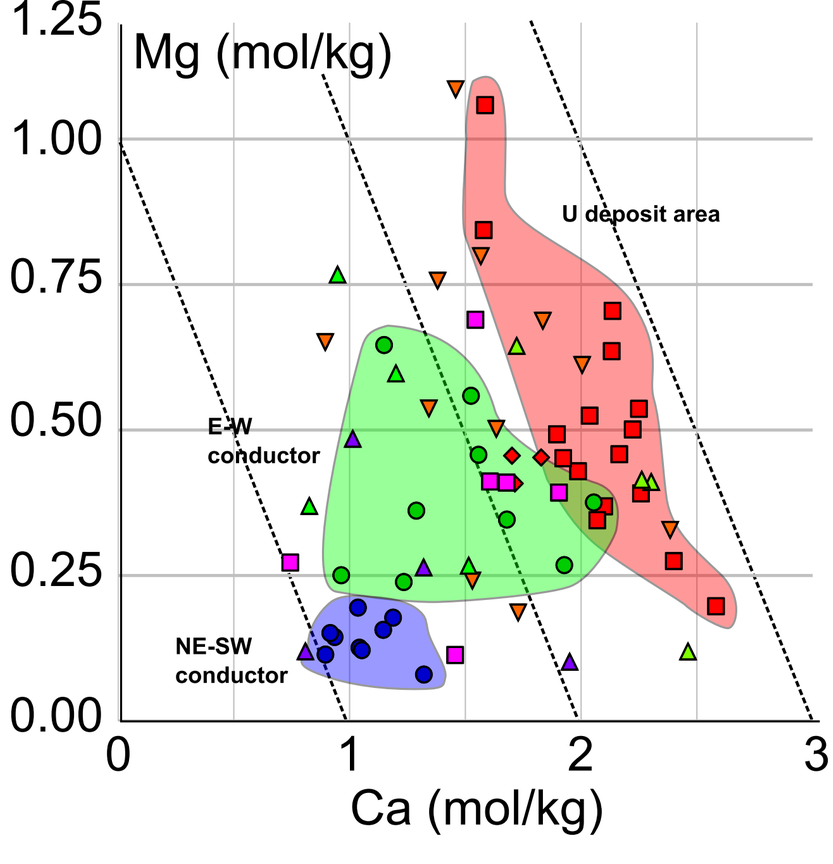
Mg (mol/kg)
Ca (mol/kg)
U deposit area
E-W conductor
NE-SW conductor

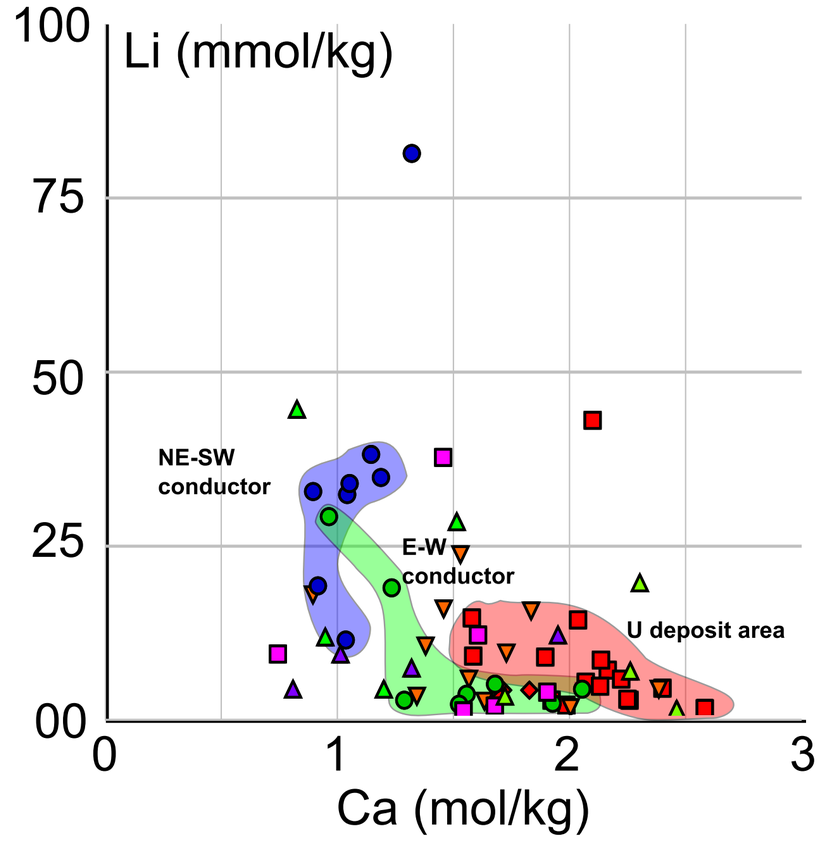
Li (mmol/kg)
Ca (mol/kg)
NE-SW conductor
E-W conductor
U deposit area

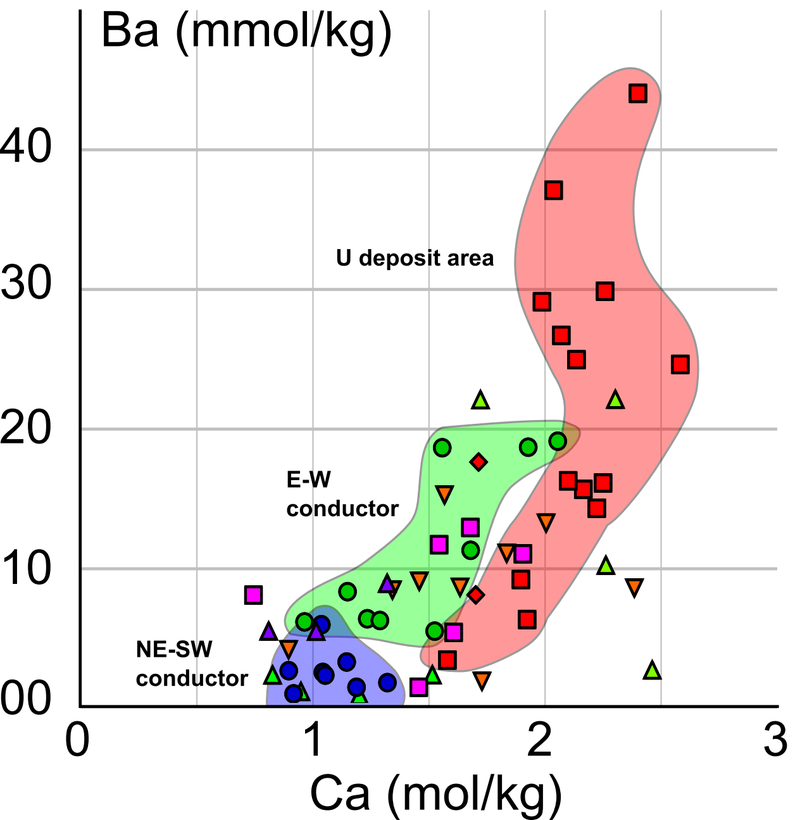
Ba (mmol/kg)
Ca (mol/kg)
U deposit area
E-W conductor
NE-SW conductor

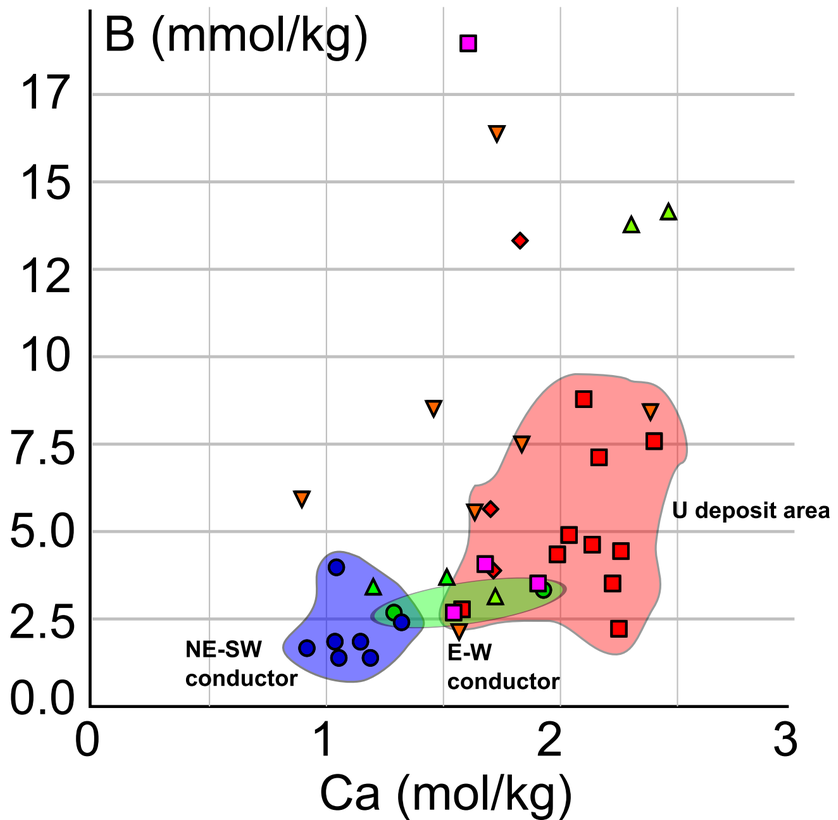
B (mmol/kg)
Ca (mol/kg)
U deposit area
NE-SW conductor
E-W conductor

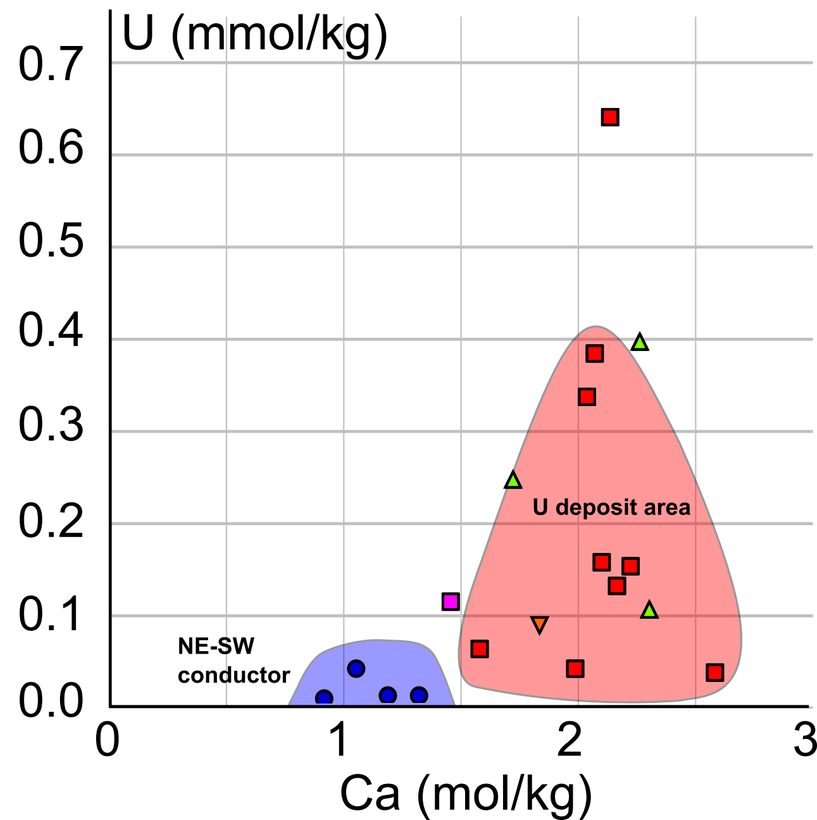
U (mmol/kg)
Ca (mol/kg)
U deposit area
NE-SW conductor

content in $CaCl_2$-rich FIs / NaCl-rich FIs
7
6
5
4
3
2
1
0
Na
Li
B
Mg
K
Ca
Mn
Fe
Cu
Zn
Sr
Pb
Ba
U
338
40
35
30
25
20
15
10
5
1
<L.O.D.

Carbonic FIPs orientations

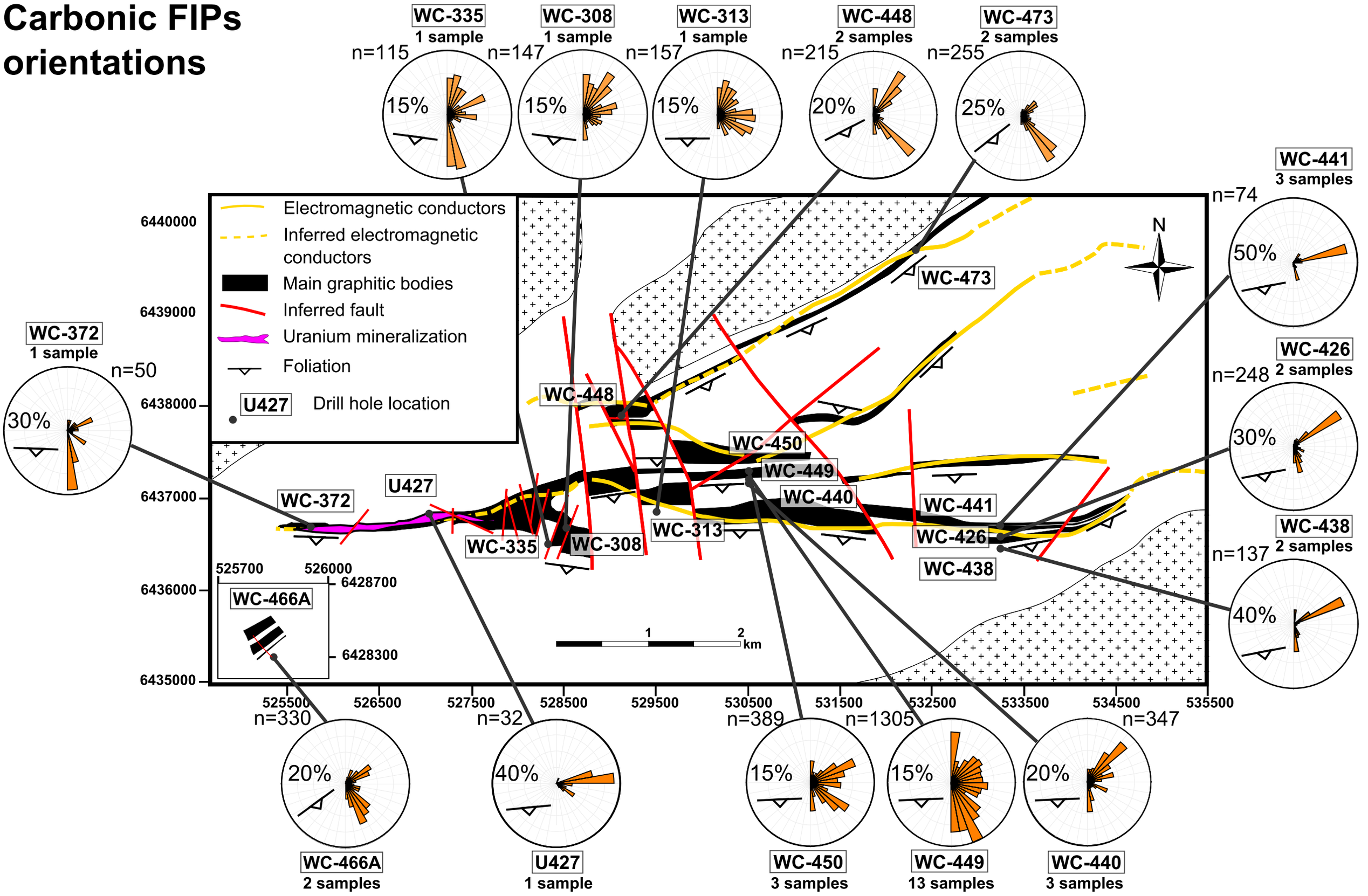

Brine FIPs orientations

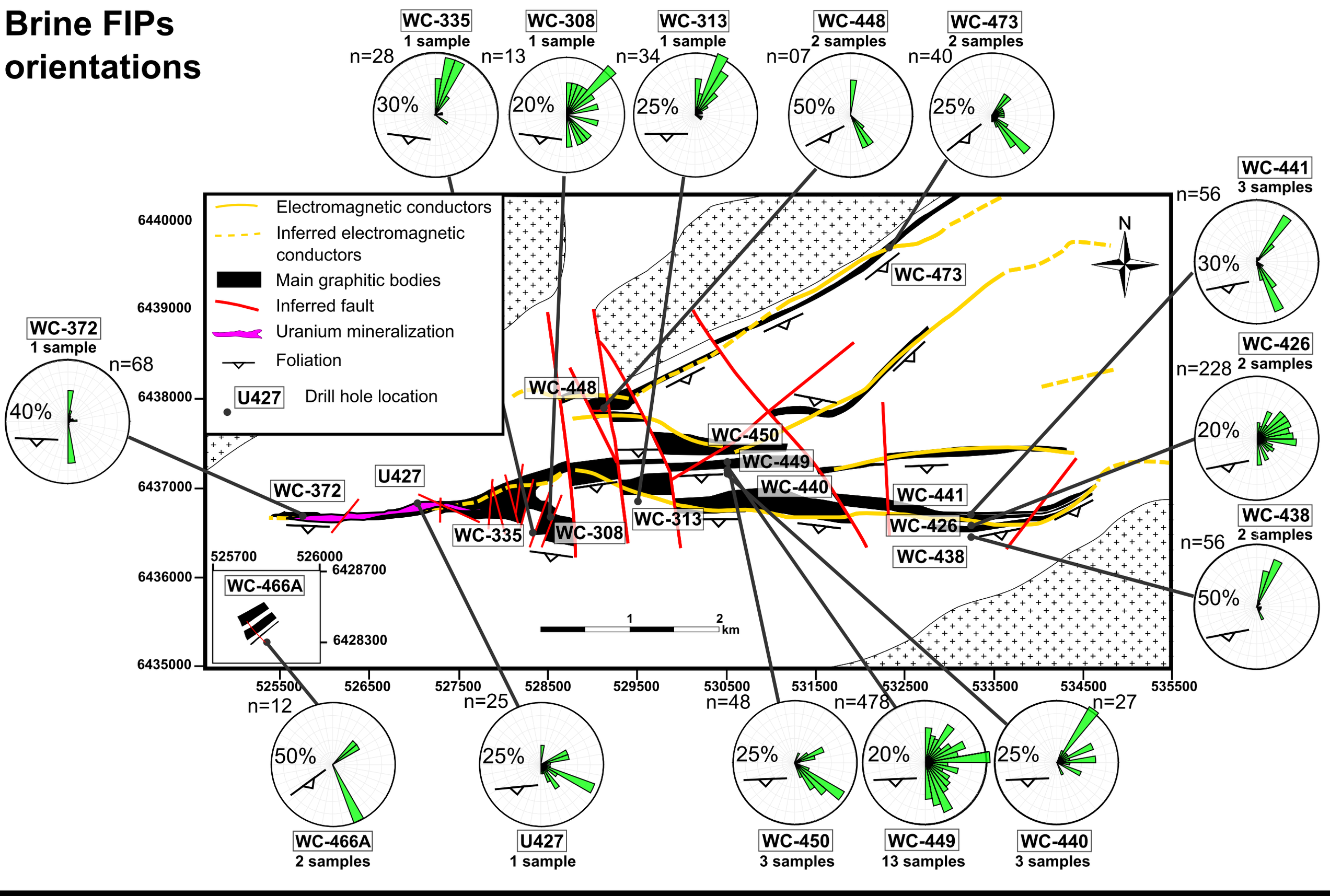

C

D

WC449

WC449

WC450

illite dominated

sudoite

UC

S

N

400m

400m

400m

500m

500m

50m

01 02 03 04 05 06 07 08 09 10 11 12 13 14 15 16 17 18 19

E

F

WC473

dickite dominated

illite dominated

sudoite

SE

NW

400m

500m

50m

20 21

26 Pegmatite sample

Metapelitic gneiss

Augen gneiss

Pegmatitic granite and anatectic sweat

Quartz breccia

Conglomerate

calcsilicate

2-5 % graphite

>5 % graphite

Graphitic cataclasite and breccia >20% graphite

carbonic FIP

Mix FIP

FIP Density (mm/mm²) carbonic fluid, δ_s

brine FIP

Mix FIP

FIP Density (mm/mm²) brine, δ_s

based on carbonic FIP

based on mix FIP

Estimated Quartz Fracture Porosity, Φ(%)

based on brine FIP

based on mix FIP

Estimated Quartz Fracture Porosity, Φ(%)

distance to fault core (m)

Isochores
$CaCl_2$-rich brine
NaCl-rich brine
litho 30°C/km
litho 40°C/km
hydro 30°C/km
hydro 40°C/km
hydro 60°C/km
Regional
diagenetic fluid
A
B
P(MPa)
T(°C)
depth litho. (km)
depth hydro. (km)
0
50
100
150
200
250
0
100
200
300
0
2
4
6
8
10
0
2
4
6
8
10

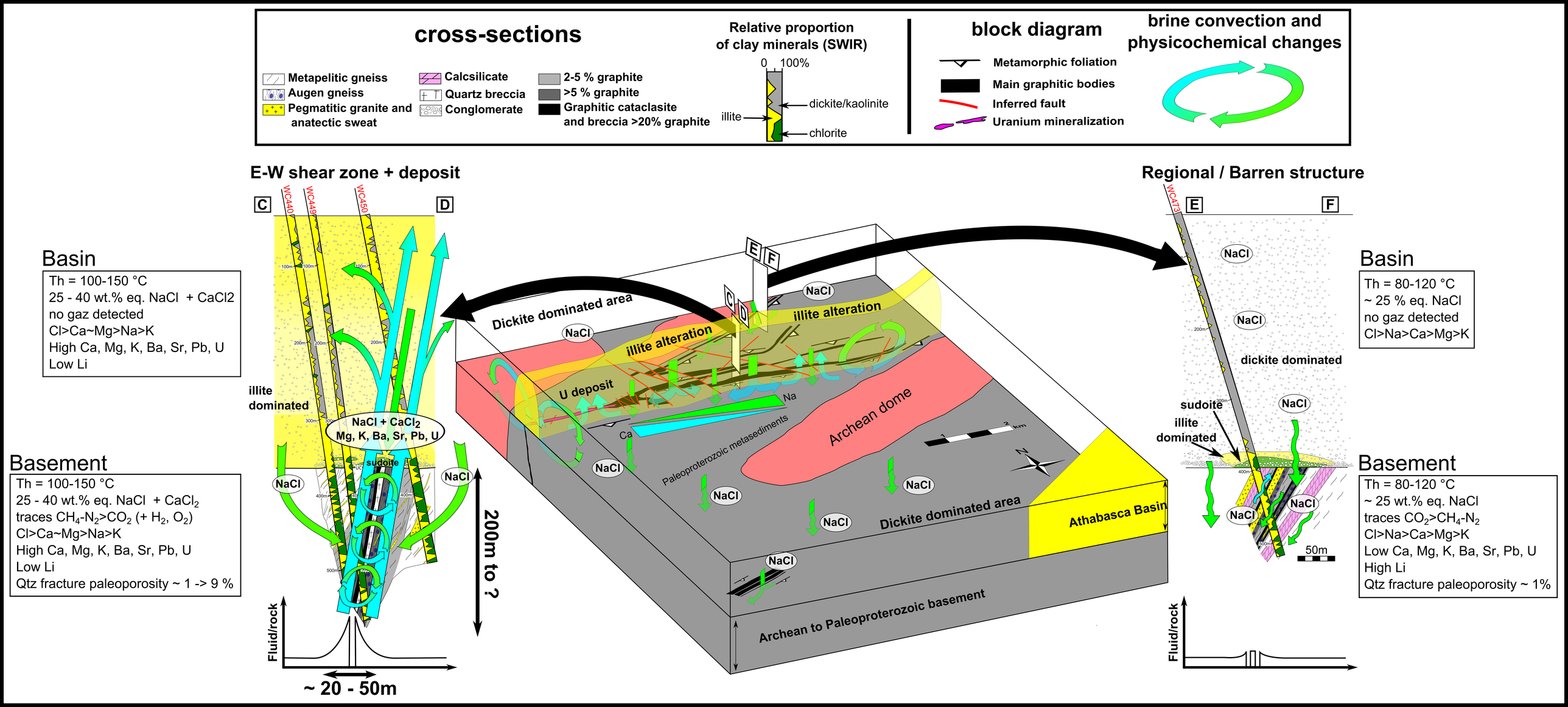
cross-sections
Metapelitic gneiss
Augen gneiss
Pegmatitic granite and anatectic sweat
Calcsilicate
Quartz breccia
Conglomerate
2-5 % graphite
>5 % graphite
Graphitic cataclasite and breccia >20% graphite
Relative proportion of clay minerals (SWIR)
0
100%
illite
dickite/kaolinite
chlorite
block diagram
Metamorphic foliation
Main graphitic bodies
Inferred fault
Uranium mineralization
brine convection and physicochemical changes
E-W shear zone + deposit
Regional / Barren structure
Basin
Th = 100-150 °C
25 - 40 wt.% eq. NaCl + CaCl2
no gaz detected
Cl>Ca~Mg>Na>K
High Ca, Mg, K, Ba, Sr, Pb, U
Low Li
Basement
Th = 100-150 °C
25 - 40 wt.% eq. NaCl + CaCl2
traces CH4-N2>CO2 (+ H2, O2)
Cl>Ca~Mg>Na>K
High Ca, Mg, K, Ba, Sr, Pb, U
Low Li
Qtz fracture paleoporosity ~ 1 -> 9 %
Basin
Th = 80-120 °C
~ 25 % eq. NaCl
no gaz detected
Cl>Na>Ca>Mg>K
Basement
Th = 80-120 °C
~ 25 wt.% eq. NaCl
traces CO2>CH4-N2
Cl>Na>Ca>Mg>K
Low Ca, Mg, K, Ba, Sr, Pb, U
High Li
Qtz fracture paleoporosity ~ 1%
WC4401
WC4491
WC4501
WC4731
C
D
E
F
illite dominated
NaCl + CaCl2
Mg, K, Ba, Sr, Pb, U
sudoite
NaCl
200m to ?
Fluid/rock
~ 20 - 50m
Dickite dominated area
illite alteration
U deposit
Na
Ca
Paleoproterozoic metasediments
Archean dome
Athabasca Basin
Archean to Paleoproterozoic basement
dickite dominated
50m

	Nomen-clature	Observed phase transitions between -180°C and 0°C	Tm_{ice} range	Used Methodology	Used system
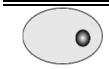	**Lw1**	Ice + HH → $H_2O_{(L)}$ + Ice + HH → $H_2O_{(L)}$ + Ice → $H_2O_{(L)}$	-30 °C to -15 °C	AqSo2e program (Package FLUIDS 1, Bakker, 2003)	NaCl - H_2O
	Lw2	Ice + HH → $H_2O_{(L)}$ + Ice + HH → $H_2O_{(L)}$ + HH → $H_2O_{(L)}$	-30 °C to -15 °C	Steele-MacInnis et al. (2011)	NaCl - $CaCl_2$ - H_2O
	Lwh	Ice + HH + $NaCl_{(S)}$ → $H_2O_{(L)}$ + Ice + HH + $NaCl_{(S)}$ → $H_2O_{(L)}$ + HH + $NaCl_{(S)}$ → $H_2O_{(L)}$ + $NaCl_{(S)}$	-30 °C to -15 °C	Steele-MacInnis et al. (2011)	NaCl - $CaCl_2$ - H_2O
	Lw'	Ice + HH → $H_2O_{(L)}$ + Ice + HH → $H_2O_{(L)}$ + Ice → $H_2O_{(L)}$	< -30 °C	AqSo2e program (Package FLUIDS 1, Bakker, 2003)	$CaCl_2$ - H_2O
	Lw'	Ice + HH → $H_2O_{(L)}$ + Ice + HH → $H_2O_{(L)}$ + HH → $H_2O_{(L)}$	< -30 °C	Steele-MacInnis et al. (2011)	NaCl - $CaCl_2$ - H_2O
	Lwh'	Ice + HH + $NaCl_{(S)}$ → $H_2O_{(L)}$ + Ice + HH + $NaCl_{(S)}$ → $H_2O_{(L)}$ + HH + $NaCl_{(S)}$ → $H_2O_{(L)}$ + $NaCl_{(S)}$	< -30 °C	Steele-MacInnis et al. (2011)	NaCl - $CaCl_2$ - H_2O
	Lw''	Ice + HH → $H_2O_{(L)}$ + Ice + HH → $H_2O_{(L)}$ + Ice → $H_2O_{(L)}$	> -15 °C	AqSo2e program (Package FLUIDS 1, Bakker, 2003)	NaCl - H_2O

	% of FIs > LOD	Ranges of Content (µg/g)
Na	100	1,091 to 57,092
Mg	100	972 to 26,383
K	100	1,621 to 86,924
Sr	100	27 to 8,405
Ca	100	29,855 to 103,502
Pb	97	26 to 2,745
Li	97	8 to 586
Mn	96	59 to 4,477
Ba	90	114 to 11,218
Zn	80	37 to 6,220
Fe	59	390 to 61,962
B	62	15 to 801
Cu	47	7 to 14,154
U	32	2 to 7,294
W	22	5 to 281
Sb	15	4 to 286

Location	Sample I.D.	Labels in Fig 9.	σ_S (carb.) (mm^{-2})	σ_S (brine) (mm^{-2})	σ_S (mix) (mm^{-2})	σ_S (brine + mix) (mm^{-2})	σ_S (carb. + mix) (mm^{-2})	Zf (carb.)	Z_f (brine)	Z_f (mix)	C_f (carb.)	C_f (brine)	C_f (mix)	Estimated qtz fract. poro. (φ) (carb. only) (%)	Estimated qtz fract. poro. (φ) (brine only) (%)	Estimated qtz fract. poro. (φ) (mix) (%)	Estimated qtz fract. poro. (φ) (brine + mix) (%)	Estimated qtz fract. poro. (φ) (carb. + mix) (%)
Pegmatite samples																		
Cross-section C - D on E-W structure	WC440-413.4	01	1.70	0.10	0.19	0.29	1.89	1.33E-03	1.11E-03	1.21E-03	590	708	650	2.2	0.2	0.3	0.4	2.5
	WC440-472.7	03	11.33	1.04	0.00	1.04	11.33	2.09E-03	1.77E-03	-	377	443	-	9.5	1	0	1	9.5
	WC440-515.6	10	5.71	0.43	1.04	1.47	6.76	9.50E-04	6.40E-04	5.30E-04	626	1231	880	6	1.2	1.2	2.4	7.2
	WC449-379	02	2.68	0.17	3.21	3.38	5.90	1.22E-03	1.59E-03	6.30E-04	644	493	619	3.8	0.2	2.1	2.3	5.9
	WC449-388.3	04	4.22	2.74	6.48	9.22	10.70	5.14E-03	2.96E-03	3.12E-03	153	265	251	1.4	1.6	3.6	5.2	5.1
	WC449-402.8	05	2.82	2.98	0.66	3.64	3.48	2.50E-03	2.46E-03	2.11E-03	314	319	372	5.3	5.7	1.5	7.2	6.8
	WC449-403.6	06	10.62	3.23	0.35	3.58	10.97	4.30E-03	2.69E-03	5.57E-03	183	292	141	4.3	2.1	0.1	2.2	4.4
	WC449-414.2	07	10.40	0.35	0.00	0.35	10.40	3.59E-03	6.50E-02	-	218	83	-	5	0.4	0	0.4	5
	WC449-434.4	08	14.31	0.41	0.92	1.33	15.23	2.97E-03	2.71E-03	1.30E-03	264	290	602	8.4	0.3	1.2	1.5	9.6
	WC449-443.7	09	4.62	0.71	2.64	3.36	7.27	3.52E-03	3.19E-03	3.50E-03	223	247	224	2.3	0.4	1.3	1.7	3.6
	WC449-481.6	11	10.39	0.04	0.58	0.62	10.98	4.70E-03	4.17E-03	3.56E-03	167	188	221	3.9	0	0.3	0.3	4.1
	WC449-501.9	12	8.45	8.26	2.28	10.55	10.74	4.08E-03	4.63E-03	3.33E-03	193	170	236	3.6	3.1	1.2	4.3	4.8
	WC449-537.7	13	9.97	4.98	1.64	6.63	11.61	1.44E-03	1.82E-03	1.92E-03	546	432	409	12.1	4.8	1.5	6.3	13.6
	WC449-560	14	13.37	6.30	4.54	10.85	17.92	8.15E-03	5.80E-03	4.74E-03	214	236	166	14.1	5.8	1.7	7.4	15.8
	WC449-562.1	15	12.8	6.87	1.07	7.94	13.87	3.23E-03	3.86E-03	2.03E-03	243	285	387	6.9	6.1	0.9	7	7.8
	WC449-565.2	16	7.23	6.85	0.55	7.40	7.78	3.72E-03	3.99E-03	4.62E-03	211	197	170	8.2	7.3	0.5	7.8	8.7
	WC450-429.7	17	4.27	1.48	0.46	1.94	4.73	1.42E-03	1.13E-03	1.24E-03	553	694	632	5.2	2.3	0.6	2.9	5.9
	WC450-469.6	18	11.77	0.48	0.13	0.61	11.90	2.79E-03	1.24E-03	2.37E-03	281	634	331	7.4	0.7	0.1	0.8	7.4
	WC450-484.5	19	6.14	0.23	0.00	0.23	6.14	1.47E-03	1.41E-03	-	535	556	-	7.3	0.3	0	0.3	7.3
E-W structure	426-338		2.39	4.41	0.00	4.41	2.39	2.10E-03	2.10E-03	-	378	611	-	2	9.8	0	9.8	2
	426-385.6		10.75	11.23	0.00	11.23	10.75	3.20E-03	3.30E-03	-	302	289	-	8.9	8.8	0	8.8	8.9
	426-363.5		4.31	7.58	0.00	7.58	4.31	1.80E-03	1.70E-03	-	442	458	-	4.2	7.7	0	7.7	4.2
	441-390.6		3.92	4.4	1.73	6.13	5.65	1.80E-03	2.00E-03	1.40E-03	434	386	575	3.8	3.8	2.2	6	6
	441-451.5		12.25	9.13	0.91	10.05	13.16	9.00E-04	8.00E-04	9.00E-04	584	652	452	10.5	8.5	0.5	8.9	10.9
	438-367.5		2.97	0.26	0.62	0.87	3.58	2.00E-03	1.60E-03	1.50E-03	389	486	518	2.6	0.3	0.7	1	3.3
	438-465.7		0.58	0.81	0.17	0.97	0.74	1.20E-03	1.10E-03	7.00E-04	432	747	1140	0.4	1.3	0.4	1.8	0.8
	308-531.8		10.32	0.79	0.00	0.79	10.32	5.90E-03	2.20E-03	-	132	351	-	3	0.6	0	0.6	3
	313-511.3		3.46	0.91	0.29	1.20	3.75	2.10E-03	1.60E-03	1.80E-03	372	478	444	2.9	1	0.3	1.2	3.1
	335-488.3		4.31	1.26	0.36	1.61	4.66	1.70E-03	1.30E-03	1.30E-03	465	587	586	4.4	1.6	0.5	2.1	4.9
Below deposit	SF-731-05-450 (N.O.)		7.45	1.91	1.05	2.96	8.51	2.10E-03	1.70E-03	1.50E-03	372	459	509	6.2	1.9	1.2	3.1	7.4
	SF-731-05-445.9 (N.O.)		3.36	0.49	0.11	0.60	3.47	3.40E-03	2.20E-03	2.00E-03	228	355	394	1.7	0.4	0.1	0.5	1.8
	U382-77.6A - (N.O.)		7.03	1.78	5.72	7.51	12.76	2.10E-03	1.20E-03	2.00E-03	373	656	391	5.8	2.6	5	7.6	10.8
	372-457.9		25.68	12.92	2.11	15.03	27.79	4.70E-03	2.40E-03	4.80E-03	168	334	165	9.6	9.6	0.8	10.4	10.4
	u427-200		4.01	3.42	0.00	3.42	4.01	1.30E-03	1.30E-03	-	595	621	-	5.3	4.7		4.7	5.3
South conductor	466A-448.7		4.48	0.54	0.00	0.54	4.48	1.70E-03	2.10E-03	-	460	383	-	4.6	0.5	0	0.5	4.6
	466A-484.3		3.5	0.00	0.00	0.00	3.5	8.00E-04	-	-	981	-	-	7.6	0	0	0	7.6
North-East Trend	448-440.2		10.58	0.14	1.49	1.63	12.08	4.50E-03	6.40E-03	1.00E-03	174	123	817	4.1	0	2.7	2.7	6.8
	448-467.3		17.16	1.28	0.95	2.23	18.11	6.30E-03	4.20E-03	3.40E-03	124	188	228	4.7	0.5	0.5	1	5.2
	473-476.2	21	3.74	1.08	0.00	1.08	3.74	1.00E-03	1.00E-03	-	752	789	-	6.3	1.9	0	1.9	6.3
	473-440.8	20	8.97	1.35	0.00	1.35	8.97	3.30E-03	2.50E-03	-	241	311	-	4.8	0.9	0	0.9	4.8
Off structure	254-466.7 (N.O.)		3.35	0.00	0.01	0.00	3.35	1.10E-03	-	-	719	-	-	5.4	0	0	0	5.4
	254-460.5 (N.O.)		4.21	0.31	0.00	0.31	4.21	1.10E-03	2.40E-03	-	687	654	-	6.4	0.9	0	0.9	6.4
Gneiss samples																		
E-W structure	426-449.5 - gneiss		7.44	0.44	0.22	0.67	7.67	1.80E-03	1.50E-03	1.50E-03	449	509	515	7.4	0.5	0.3	0.8	7.7
	441-362 - gneiss		11.32	0.30	0.27	0.57	11.59	3.20E-03	1.90E-03	2.10E-03	243	406	379	6.1	0.3	0.2	0.5	6.3
	244-460.5 - gneiss		8.50	0.06	0.00	0.06	8.50	3.90E-03	2.70E-03	-	201	288	-	3.8	0	0	0	3.8
Below deposit	U382-72.3 - gneiss		13.86	0.91	0.00	0.91	13.86	2.50E-03	1.90E-03	-	315	404	-	9.7	0.8	0	0.8	9.7
	U427-29.8 - gneiss		4.29	0.00	0.05	0.05	4.34	1.00E-03	-	1.10E-03	791	-	712	7.5	0	0.1	0.1	7.6

cross-sections

- Metapelitic gneiss
- Augen gneiss
- Pegmatitic granite and anatectic sweat
- Calcsilicate rocks
- Quartz breccia
- Conglomerate
- 2-5 % graphite
- >5 % graphite
- Graphitic cataclasite and breccia >20% graphite

block diagram

- Metamorphic foliation
- Main graphitic bodies
- Inferred fault
- Uranium mineralization

brine convection and physicochemical changes

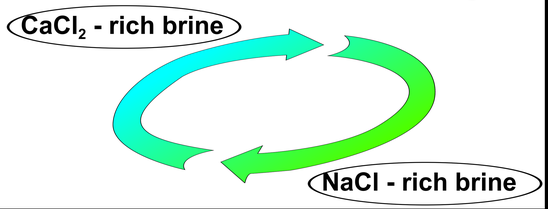

E-W shear zone + deposit

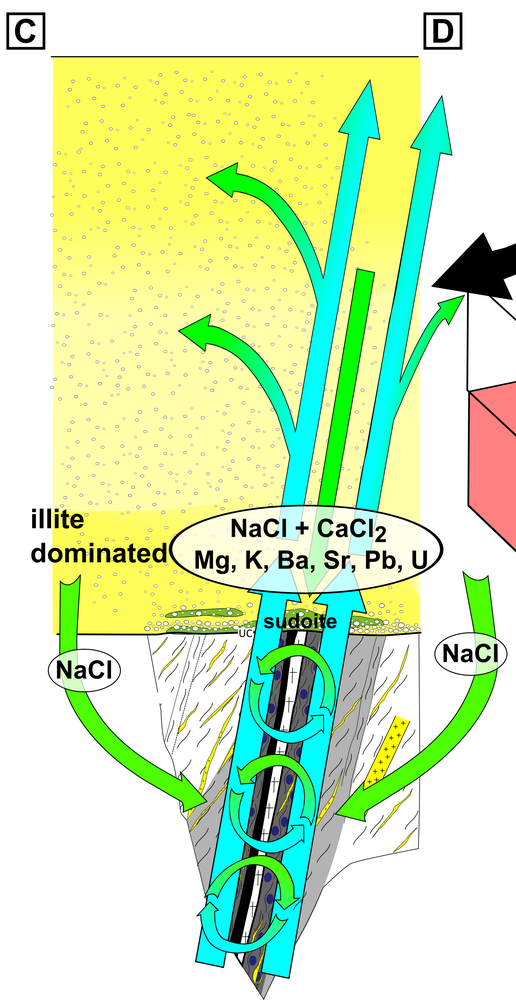

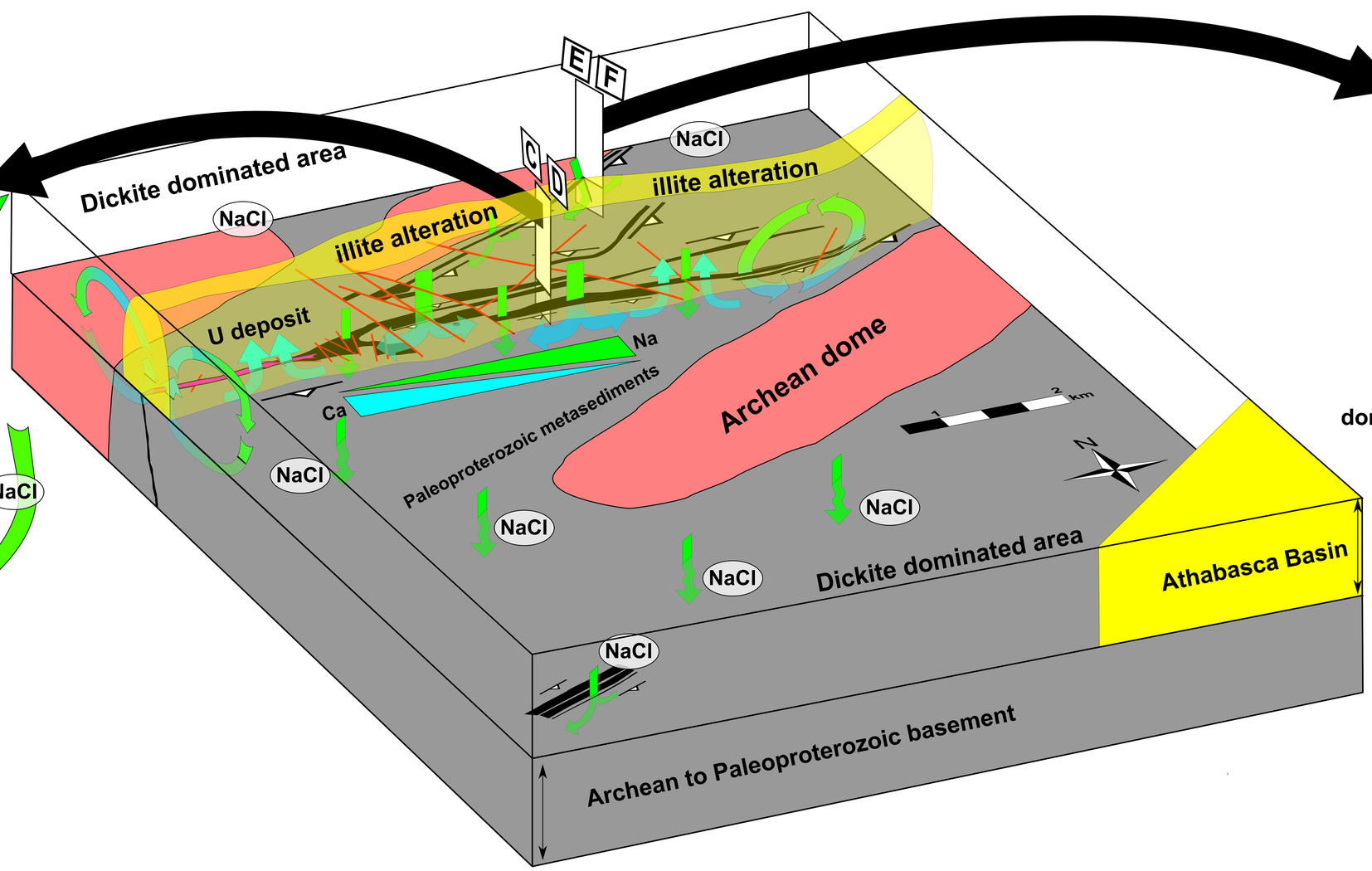
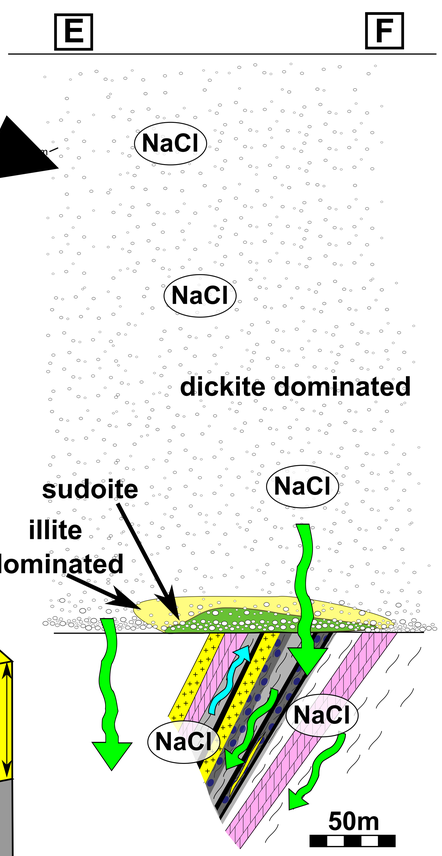
Regional / Barren structure